공학박사 학위논문

Morphological Control of Mesoporous Iron Oxide and N-doped Carbon Nanomaterials for their Applications to Lithium Ion Battery and Fuel Cell

메조기공 산화철과 질소−도핑 카본 나노물질의

리튬 이온 전지와 연료전지 응용을 위한

형태학적 제어

2018년 2월

서울대학교 대학원
화학생물공학부
이 수 홍

Abstract

Morphological Controls of Mesoporous Iron Oxide and N-doped Carbon Nanomaterials for their Applications to Lithium Ion Battery and Fuel Cell

Soo Hong Lee

School of Chemical and Biological Engineering

The Graduate School

Seoul National University

Recently, various mesoporous nanomaterials are extensively investigated for their promising applications in electrochemical devices such as Li-ion batteries (LIB) and fuel cells. Mesoporous nanomaterials have extremely large surface area with high density of active sites as

well as short diffusion distance. These properties facilitate mass transfer of reactants and products and make mesoporous nanomaterials ideal candidates especially for electrode materials in electrochemical devices. However, there are a number of issues that need to be resolved to realize the commercially feasible, high-performance electrode materials. High surface-to-volume ratio of mesoporous materials often causes extensive side reactions in uncontrolled ways. Kinetics of mass transfer in the complex pore structures is not well understood. To gain control of the optimization parameters, we need to establish standard design principle based on structure-function relationship. This dissertation presents noble approaches to optimizing electrochemical performance of mesoporous materials which is guided by newly developed analytic methods. By controlling morphology, pore structure, and composition of mesoporous materials on the basis of rational design principles, I accomplished the development of high performance electrodes for electrochemical devices.

To apply mesoporous materials to LIB electrodes, a robust and well-designed morphology is essential: the formation of solid electrolyte interphase (SEI) needs to be minimized and volume expansion during charge/discharge cycles should be tolerated. In this study, I focus on

utilizing metal oxide nanoparticles. While having large storage capacity, nanoparticles suffer from the excessive generation of solid-electrolyte interphase (SEI) on the surface, low electrical conductivity, and pulverization. To compensate for these shortcomings, I designed and prepared mesoporous iron oxide nanoparticle clusters (MIONCs) using a bottom-up self-assembly approach. These materials exhibit excellent cyclic stability and rate capability owing to their three-dimensional mesoporous nanostructure. By controlling the geometric configuration, I was able to achieve stable interfaces between the electrolyte and active materials, confining the SEI formation on the outer surface of the MIONCs.

Using porous carbon materials for fuel cell electrodes is another important issue in energy material research. Fe-N-C catalysts have been extensively studied to replace expensive Pt/C electrodes, which facilitate the oxygen reduction reaction (ORR) at the cathode. The ORR performance not only depends on the atomic configuration of the active sites but also heavily relies on structural factors, such as active site utilization and mass transfer properties. Thus, a systematic optimization of the Fe-N-C catalysts was conducted to maximize the ORR activity in alkaline media. Through comparison with the control groups by

complex capacitance analysis, I conclude that the mesoporous structure is essential for increasing the utilization of active sites, whereas a nano-sized particulate morphology is required to achieve superior rate capability. During accelerated durability tests, the optimized catalysts show negligible activity loss over 10,000 potential cycles, demonstrating their excellent long-term stability.

In the first chapter of the Thesis, various synthetic strategies for applications of mesoporous materials to LIBs and fuel cells are reviewed with representative examples from the previous studies. In the second and the third chapters, my works on the development of metal oxide nanoparticles-based mesoporous LIB electrode materials and carbon-based non-Pt electrode materials are discussed. Through my study, I have shown that controlling morphology and pore structure can be a solution to improving electrochemical activity and stability of the mesoporous material electrodes simultaneously.

Keywords: mesoporous material, Li-ion battery, solid-electrolyte interphase, oxygen reduction reaction, complex capacitance analysis

Student Number: 2011-21061

Contents

Chapter 2. Magnetite Nanoparticle Clusters as Highly Stable Anodes for Lithium-Ion Batteries via Controlled SEI Formation

Chapter 3. Optimization of Hierarchical Porous Fe-N-C Electrocatalysts for Oxygen Reduction Reaction

List of Tables

List of Figures

x

xv

xvii

Chapter 1. An Overview: Application of Mesoporous Nanomaterials for Li-ion battery and Fuel Cell Electrodes

1.1 Introduction

1.1.1 Optimization of electrode materials for renewable energy applications

Sustainable energy issues originate from the current annual global power consumption, which is approximately 14 terawatts (TW, 14×10^{12} J s^{-1}). About 80% of the energy is obtained from carbon dioxide (CO_2)-emitting fossil fuels (oil, coal, and natural gas) and less than 1% comes from carbon-free renewable power sources, such as biofuels and geothermal, wind, and solar power.[1] Because of the rapid industrialization of emerging economies, such as China and India, global power demand is expected to grow to approximately 25–30 TW by 2050, when a "business as usual" growth is assumed.[2] If these increasing power demands are satisfied by fossil fuels, the concomitant CO_2 generation and related global warming effects will pose a severe

environmental threat to human civilization. Therefore, the development of efficient energy conversion and storage devices is of vital importance. The representative technologies for energy conversion and storage are fuel cells and Li-ion batteries, respectively. Fuel cells are direct electrochemical fuel-to-electricity energy conversion technologies, and they have higher theoretical efficiencies (50–60%) compared to internal combustion engines (ca. 35% efficiency).[3] Among the various types of fuel cells, proton-exchange membrane fuel cells are under active research and have massive potential for a variety of uses, ranging from automotive to stationary power applications. Batteries provide electrons originating from the difference in chemical potential of the cathode (excess of electrons) and anode (deficient electrons) materials. Among the variety of battery technologies, Li-ion batteries (LIBs) have received much attention as rechargeable power sources because of their high energy densities and wide electrochemical stability window.

Despite extensive efforts to meet current energy demands, it is still necessary to improve the energy and power densities of batteries, capacitors, and fuel cells.[4] As shown in Figure 1.1, the increasing demand for higher energy and power densities has resulted in a shift to

a new performance growth curve.[5] To achieve the new performance growth curve, electrodes in galvanic and electrolytic cells must be optimized with respect to diverse characteristics, such as mass transport and electronic and ionic conductivity, during operation. However, the architecture of electrochemical cell has many interfaces that are composed of electrochemically active materials, conductive agents, and ion-conducting electrolytes. Electrochemical reactions occur at the interfaces of various phases, and electrons, ions, and reactants interact at these interfaces. For example, fuel-cell electrodes generate electricity through reactions at a three-phase boundary comprising gas (reactant), ions (electrolyte), and electrons.[6] Although the reaction can be regarded as occurring at the active sites where the active materials are located, the overall reactivity is governed by the transport phenomena and the degree of formation of the three-phase boundary at the electrode. However, the characterization of the transport phenomena and three-phase boundary is particularly challenging. The discrepancy between the electrochemical surface area (ECSA) and geometrical surface area poses difficulties in predicting the intrinsic activity of an active material. It has been previously shown that approximately 50% of the Pt nanoparticles

3

(NPs) participate in the oxygen reduction reaction (ORR) because of incomplete connections between Pt sites and the electrolytes.[7] Therefore, the optimization of the electrode architecture requires efficient transport pathways, through which all the charges and molecules move. In this respect, mesoporous materials with diverse morphologies and sizes have drawn great attention because of their facile mass transport and large surface area. In this chapter, I introduce advantages and disadvantages of the mesoporous structure when this structure is applied in electrochemical application. Three different kinds of synthetic methods to achieve diverse mesoporous nanomaterials are followed. Subsequently, the basics of two representative electrochemical applications, such as Li-ion battery and fuel cell, are explained to develop optimized mesoporous nanomaterials for facile mass transfer.
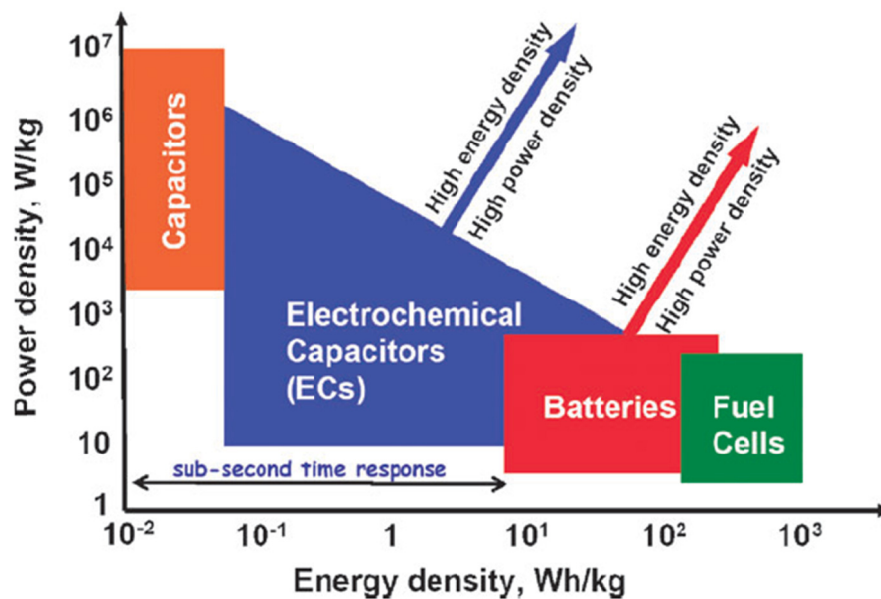
Figure 1.1 Comparison of the operational dimensions of energy storage and conversion devices (from Ref. [5] Rolison, D. R.; Long, J. W.; Lytle, J. C.; Fischer, A. E.; Rhodes, C. P.; McEvoy, T. M.; Bourg, M. E.; Lubers, A. M. *Chem. Soc. Rev.* **2009,** *38*, 226–252.)

1.1.2 Advantages of Mesoporous Materials

Mesoporous materials with pore diameters of 2 to 50 nm are attracting significant interest because of their large surface area and open porous structure with excellent interconnectivity, electrical conductivity, and structural stability.[8] Generally, pores are categorized based on their sizes: micropores (less than 2 nm), mesopores (2–50 nm), and macropores (more than 50 nm). One advantage of mesoporous materials over other morphologies is their large surface area. Mesoporous materials with large surface areas are good candidates for catalyst supports that can immobilize a large number of active species on the surfaces. If the interface between the electrode and electrolyte is properly controlled, mesoporous materials will have much larger ECSAs than geometric surface area and generate electrical currents several orders of magnitude greater than those of non-mesoporous materials.[9] However, the advantages of a large ECSA are restricted to surface-confined redox reactions or reactions in which the redox current is directly correlated with increasing ECSA.[10] For example, in the fast charge-transfer kinetics of solution-phase redox reactions, there is no possibility of diffusion to the inner surface of the electrode at the characteristic timescale of

the experiments.[11]

The other advantage of mesoporous materials is their facile charge and mass transfer. In commercial electrocatalysts, small NPs are dispersed in conducting supports, such as porous carbon or conductive metal oxides, to increase the surface-to-volume ratio and provide electrical contact. Even though the ECSAs of mesoporous materials are comparable to those of the NP-supporting heterostructures, the mesoporous structures exhibit much higher charge transfer rates. Their continuous wall structure facilitates electron transfer in comparison to the NP-supporting heterostructures, which may suffer from interparticle resistance to charge transport. Moreover, ordered and regular channels comprising various pore structures allow rapid mass transport compared to diffusion in nonporous or disordered pore structures.[12] The mechanism of ion transport and diffusion has been extensively studied concerning supercapacitors, although the exact mechanism of transport and diffusion in porous materials is unclear and complicated by many factors, such as the shape of pores, connectivity, and pore-size distribution.[13] In supercapacitors, micropores account for most of the geometrical surface area and are expected to be the most efficient pores in double-layer formation.

According to previous reports, the maximum capacitance is obtained when the pore size of the electrode material is close to the size of an ion in the electrolyte.[14] However, the narrow walls channels of the micropores may interfere with ion transportation, resulting in kinetic polarization in the charge and discharge process. A micro/mesopore region with a diameter of 1.3–3.4 nm can provide diffusion paths for electrolyte ions. In this region, the diffusion distance will also be very short if the micropores are located within the mesopore walls. The macropores play a critical role, acting as an ion buffering reservoir, and decrease the ion transport distance. However, the pore sizes are continuously distributed from micropores to macropores, leading to complexity in the analysis. Moreover, the porous structures, confirmed by gas adsorption–desorption techniques, exhibit quite different characteristics compared to those of electrochemical electrodes because of the larger size of the solvated ions compared to an inert gas. From this fundamental viewpoint, a separate analysis of only one kind of porous structure during cell operation is essential to determination of the roles of each pore system.

1.1.3 Disadvantages of Mesoporous Materials

Mesoporous materials for electrochemical applications also have disadvantages derived from their unique pore structure and morphology. First, the large geometrical surface area can cause many side reactions, which are directly related to performance degradation and safety issues of electrochemical devices. Although the large surface area can generate a large number of active sites as desired, unwanted side reactions can also occur. Uncontrolled side reactions can deactivate the entire catalyst by the deposition of by-products on the active sites and degrade electrochemical performance. As a representative example, the formation of excessive SEI on the anode surfaces of LIB is related to the loss of specific capacity during cycling.[15] This subject will be discussed in Chapter 2.

Secondly, another disadvantage originates from the porous structure, which can decrease the volumetric density (tap density) of the electrodes. The activity or capacity of an electrode is measured and calculated on the basis of the loading weight or volume (e.g., specific activity and volumetric capacity), depending on the application of the electrode. A low tap density leads to a low volumetric capacity and requires a high mass loading electrode to match the loading weight.

High mass loading results in thick electrodes and makes it difficult to maintain the electrical and ionic pathways during the electrochemical reaction.[16] A deficiency in the porous structure will result in the internal blockage of the mass transfer pathways, whereas excessive porosity can lead to low volumetric activity. Therefore, the pore structure and pore volume quantity must be optimized depending on the desired applications.

Lastly, the complex nature of the transport problem have plagued the theoretical and experimental characterization of mass and charge transfer in mesoporous materials .[17,18] Although previous reports have attempted to correlate the porous structure with the electrochemical performance, it is still hard to predict the intrinsic activity and stability of the electrodes precisely.[19,20] Fundamental studies based on *in situ* NMR[21,22] and electrochemical quartz crystal microbalance measurements[23] have quantitatively characterized the ion-charging process in supercapacitors. However, a quantitative characterization of the porous electrodes used in fuel cells and LIBs is still lacking. The transport of the reactants and products to and from the active sites controls the electrochemical reaction efficiency. Recently, it has been reported that the dominant mode of mass

transport at the electrode is nanodiffusion rather than bulk diffusion.[24] Nanodiffusion occurs within a diffusion layer with dimensions on the nanometer scale. Figure 1.2 is a representation of an electrocatalytic film in which nanodiffusion and bulk diffusion take place. The identification and quantitative characterization of mesoporous materials are necessary to demonstrate the mechanism of the electrochemical reaction in terms of activity and selectivity. This subject will be discussed in Chapter 3.
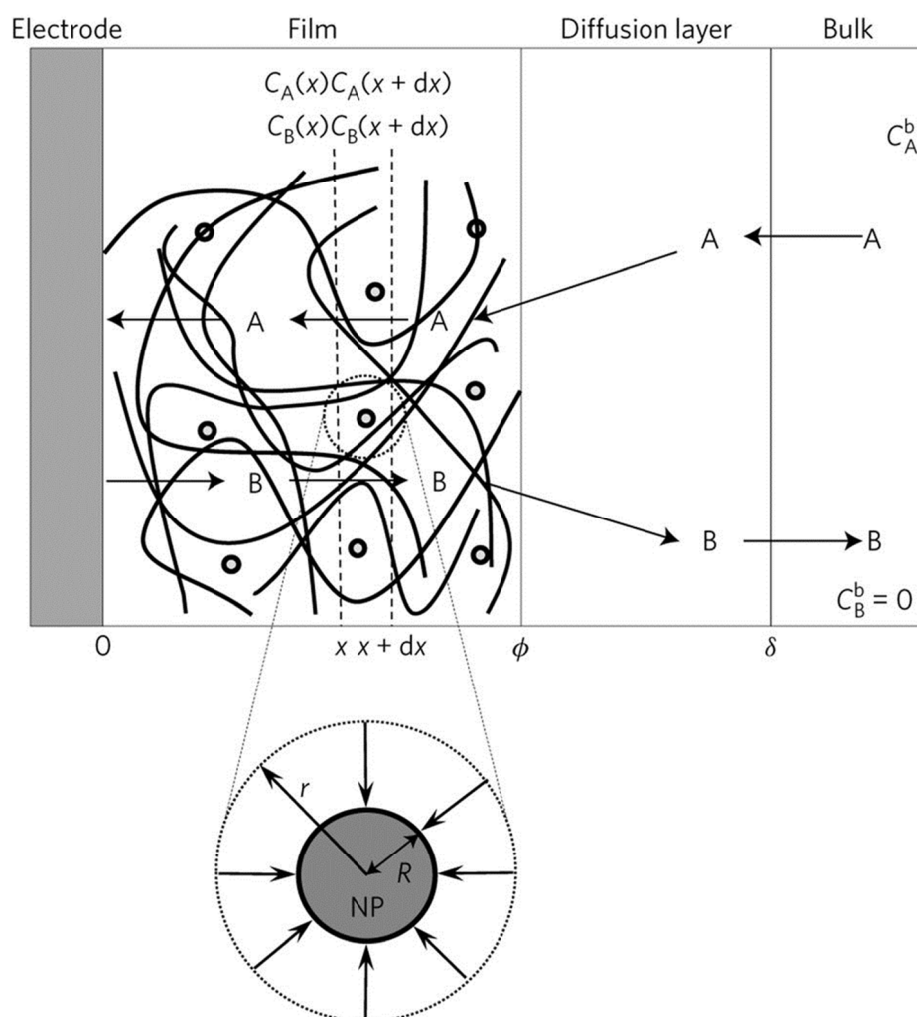
Figure 1.2. Schematic illustration of the electrocatalytic film. The catalyst nanoparticles are the grey circles, and the electronic conductor is represented by the thick black tortuous lines. (from Ref. [24] Costentin, C.; Di Giovanni, C.; Giraud, M.; Saveant, J.-M.; Tard, C. *Nat. Mater.* **2017,** *16*, 1016–1021.)

1.2 Synthetic Methods

There are diverse synthetic routes for preparing mesoporous materials, such as siliceous materials, metal oxides, and even metal chalcogenides. Three typical pathways leading to mesoporous materials will be discussed in the following section. The hard-template (nanocasting) method, which uses a mesoporous silica or carbon as a template, will be discussed first. Soft-template methods utilizing surfactants or block copolymers as templates and recently developed mesoporous superstructures assembled from colloidal NPs are discussed in the subsequent sections.

1.2.1 Hard-template Method

The hard-template method, the most common synthetic route to mesoporous materials with an ordered pore structure, is based on the "cast and mold" process, which is analogous to metal casting. Rigid and porous materials (on the nanometer or micrometer scale) can be used as templates or "molds." A precursor, which is generally in the form of liquid or solution, adheres to the surfaces of the templates or fills the void spaces in the template. Subsequently, heat treatment

transforms the precursor into a solid material. Finally, diverse etching processes are conducted to remove the template, liberating the cast with an inverse morphology of the template. Figure 1.3 shows representative examples of the hard template method, including infiltration and coating.[25]

An elaborate consideration of various factors is required for preparing mesoporous materials through the hard-template method. For example, the choice of the precursors can affect the morphology or porosity of the final product. For an exact replication of the template, the precursor must uniformly fill or coat the template.[26] To achieve this goal, the precursor solution should easily wet the template surface. It is crucial for the precursor solution and template to have a similar polarity to allow homogeneous mixing. Functionalization of the template surface is useful in changing its net charge or polarity for ensuring a favorable coating.[27] If this is not achieved, the precursor may coat other surfaces in the reactor or aggregate without coating the template. Moreover, the precursor solution must have a sufficiently low viscosity to facilitate the filling or coating process. The existence of additional solvents can help in this process, preventing imperfect infiltration and aggregation of the precursor itself.[28]. Considering

these requirements, metal salts dissolved in a polar solvent are commonly used as precursors for preparing mesoporous inorganic materials. If the target composition of the porous materials is silica (SiO_2), tetraethyl orthosilicate (TEOS) is a common precursor. Ordered mesoporous carbon materials can be prepared by using low-molecular-weight phenol-formaldehyde oligomers (PF sol) as a precursor.

After the filling or coating process, the precursor must be consolidated into a rigid, solid-phase material. For the condensation, chemical reactions at elevated temperatures are usually used, including sol-gel reactions or polymerization. An acidic or basic catalyst is needed in this process to ensure the cross-linking of the precursor molecules. As the condensation proceeds, a three-dimensional gel is formed, replicating the template morphology. Having control over the reaction rate is quite important because rapid gelation or uncontrolled precipitation should be avoided. Rapid gelation can repel the precursor sols from the templates, resulting in the aggregation of the product gels.[29] The same consideration is applied to the further consolidation of the gels by high-temperature thermal treatment (>300 °C). The crystallization of a metal oxide or

the carbonization of a polymer takes place during the heat treatment, accompanied by substantial shrinkage of the porous materials. The shrinkage originates from the evaporation or combustion of some parts of the residual precursors, which can be easily decomposed at high temperature. Excessive shrinkage can cause blockages of the porous structure, sintering, and total delamination from the template and subsequent separation of the template and product.[30] Therefore, careful control of the temperature, heating rate, and holding times is a key to successful synthesis of intact hierarchical or mesoporous structures.

The removal of the template or etching is the final and sometimes optional step, depending on the template used in the synthesis. Chemical etching using a strong acid or base is generally applied for the selective removal of many different templates. Several etching cycles are needed to remove the template completely. In addition, the strong acid can change the surface functional groups in the product material by imparting surface hydroxyl group or carboxylic acid groups through oxidation.

Many types of rigid structure with features at different scales can be used as templates if the precursor has a chemical affinity for the

surface of the template. Figure 1.4 is a compilation of images that show representative templates utilized in the hard-template method.[31] Various kinds of preassembled hard templates, including films[32], fibers,[33] powders,[34] and monolithic materials,[35] are frequently utilized for the synthesis of porous materials. Diverse silica-based structures with ordered pore systems are representative examples of hard templates, owing to easy fabrication, wide range of pore structures, and facile modification of surface.[36] Discrete colloidal nano- or microparticles can also be used as a hard template for the synthesis of hollow spherical particles.[37] The sedimentation of a suspension of spheres under gravity can generate monolithic colloidal crystals, which can also be used as unique hard templates. In specific synthetic conditions, the hard templates do not always have to be prepared prior to synthesis. Some materials including salts,[32] carbon,[38] and even ice crystals[39] in the precursor solution can be transformed into templates *in situ* during synthesis. The method needs precise control over the amount and location of template, which determines the pore morphology. Figure 1.5 represents the morphology and elemental analysis of mesoporous metal oxide nanostructures, which were synthesized using the hard template.[26]

1 7
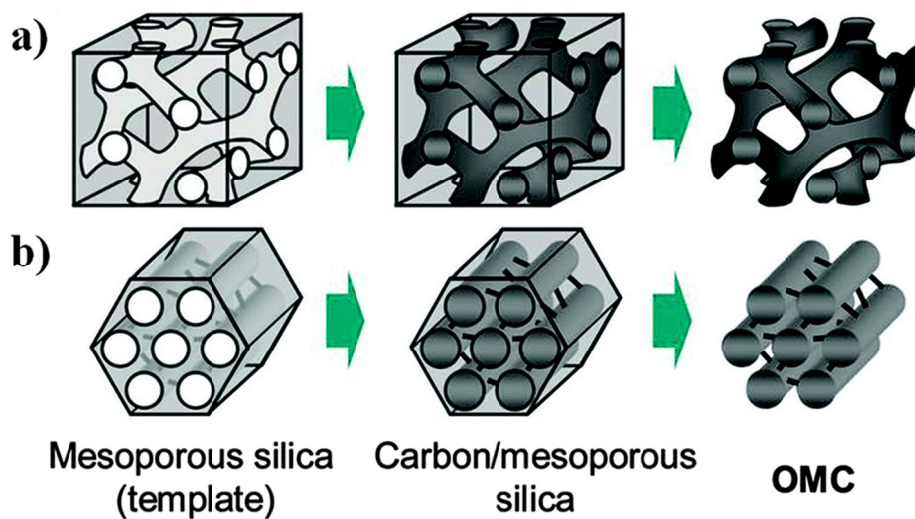
Figure 1.3. Schematic representation of the hard template process to prepare ordered mesoporous carbons (OMC). The structures used as templates represent pre-formed mesoporous silica of (a) MCM-48 and (b) SBA-15. (from Ref. [25] Roberts, A. D.; Li, X.; Zhang, H. *Chem. Soc. Rev.* **2014,** *43*, 4341–4356.)
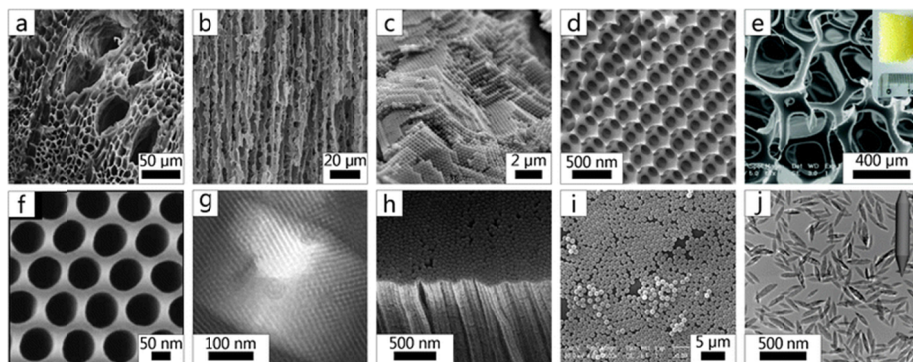
Figure 1.4. A compilation of images showing representative examples of templates using the hard-template method. (a) A plant stem, (b) freeze-dried starch, (c) a polymeric colloidal crystal, (d) a three-dimensional ordered macroporous structure, (e) polyurethane, (f) an anodic aluminum oxide (AAO) template, (g) an *in situ* NaCl crystal template, (h) a polymer produced from an AAO membrane, (i) colloidal silica spheres, and (j) rod-shaped nanoparticles. (from Ref. [31] Petkovich, N. D.; Stein, A. *Chem. Soc. Rev.* **2013,** *42*, 3721–3739.)
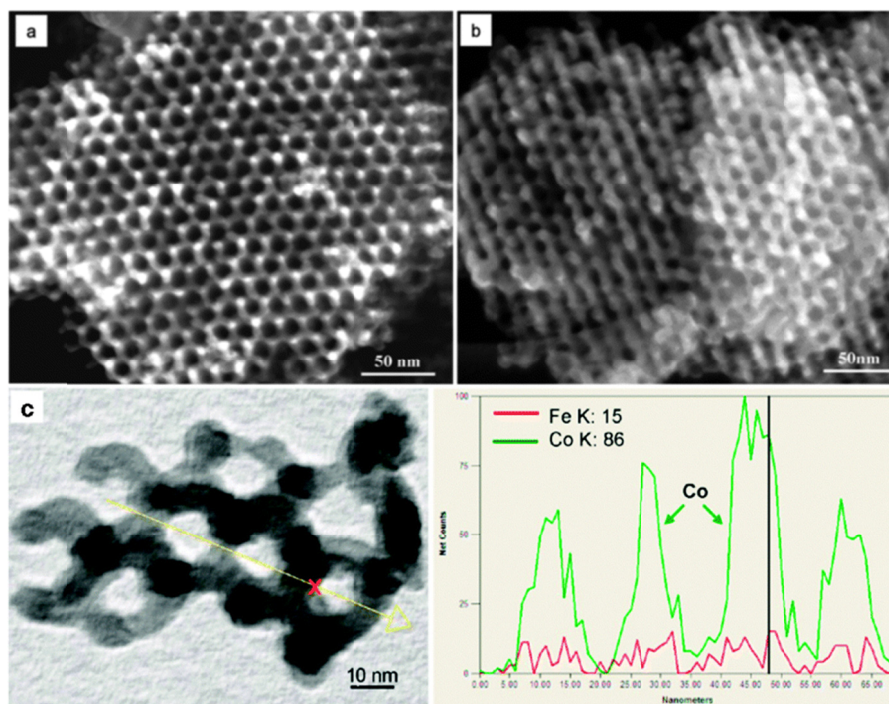
Figure 1.5. SEM images of (a) CO_3O_4 from the KIT-6 template. (b) CO_3O_4-$CoFe_2O_4$ nanocomposite and (c) line scan scanning transmission electron microscopy (STEM) energy-dispersive X-ray spectroscopy (EDX) elemental analysis of sample (b). (from Ref. [26] Gu, D.; Schuth, F. *Chem. Soc. Rev.* **2014**, *43*, 313–344.)

1.2.2 Soft-template Method

A large number of mesoporous materials have been synthesized through self-assembly of surfactants. The surfactants have two or more chemically distinct functional groups covalently bonded together. These groups are thermodynamically incompatible with each other because the entropy of mixing per unit volume is small.[40] Surfactants are classified as cationic, anionic, or nonionic surfactants based on the charge of the head group. Quaternary cationic surfactants are particularly efficient for the synthesis of mesoporous silica structures.[41] They consist of at least one quaternary amine (hydrophilic) head group and at least one (hydrophobic) tail group. This type of surfactant also includes quaternary ammonium-, gemini-, bolaform-, and multiple headgroup-type surfactants, which have been used as templates to prepare various mesoporous structures.[41] Cationic surfactants have outstanding solubility and are generally compatible with acidic and basic media, but they are expensive and toxic. In contrast, anionic salt surfactants consist of carboxylates, sulfates, and phosphates, which act as hydrophilic groups.[42] These surfactants are usually assisted by positively charged precursors to form electrostatic interactions. However, they are used infrequently in

comparison with cationic and nonionic surfactants. Nonionic surfactants are widely used in industry owing to their wide variety of chemical structures, low price, nontoxicity, and biodegradability. The chemical structure or functional groups of nonionic surfactants can be easily modified to control self-assembly or micelle size. Commonly used nonionic surfactants include Brij surfactants, which contain a linear alkyl chain connected to a hydrophilic polyethylene oxide (-CH_2-CH_2O-O-, PEO) chain, and the Pluronic family, tri-block PEO_x-PPO_y (polypropylene oxide)-PEO_x surfactants. The hydrophobicity of PPO group is sufficient for micelle formation compared to the PEO group. The micelle formation in nonionic surfactants largely depends on the van der Waals interactions and hydrogen bonding.

Two conditions must be satisfied for the formation of micelles in solution: the Krafft temperature and critical micelle concentration (CMC). The micelles can be formed above a given temperature range (Krafft temperature) because, at this temperature, their solubility increases dramatically. The micelles in the solution can be formed spontaneously after reaching a narrow concentration range (the CMC). After reaching the CMC, any added surfactant is incorporated into the micelles. Ordered mesoporous materials are always obtained when the

CMC values are between 0 and 20 mg L^{-1}. After forming micelles in solution, the final mesoporous structure is dependent on the liquid-crystal phases in the case of ionic surfactants. The packing parameter (*g*) of ionic surfactants is widely used to explain why certain liquid crystals form in solution;

$$g = V / (a_0 l),$$

where *V* is the total volume of hydrophobic surfactant chains, a_0 is the effective hydrophilic head group area at the surface of an aqueous micelle, and *l* is the kinetic surfactant tail length.[43] Figure 1.6 illustrates how the packing parameter is related to the typical liquid crystalline phases and shows models of various types of liquid crystals observed in a surfactant-containing solution.[43] The liquid crystal phases of the surfactants are important for controlling the porous structure because liquid crystals are transformed into pore networks during heat treatment. In the case of nonionic surfactants, the block copolymers can result in microphase separation on the molecular scale (5–100 nm), producing complex nanostructures with various morphologies. The Flory–Huggins interaction parameter, χ_{AB}, explains the driving force for this microphase separation.

$$\chi_{AB} = \left(\frac{z}{\kappa_B T}\right) [\varepsilon_{AB} - \frac{1}{2}(\varepsilon_{AA} + \varepsilon_{BB})]$$

Here, z is the number of nearest neighbors per monomer in the polymer, $\kappa_B T$ is the thermal energy, and ε_{AB}, ε_{AA} and ε_{BB} are the interaction energies per monomer between A and B, A and A, and B and B, respectively. χ_{AB} multiplied by N (the degree of polymerization or number of monomers per chain) indicates the interactions per chain, and, if $\chi_{AB}N$ is greater than 10.5, microphase separation can occur.[46]

Although the packing parameter and Flory–Huggins interaction parameter can predict various kinds of morphologies of liquid crystals (pore structure), the micelles and liquid crystals are dynamic structures that are readily changed when precursor molecules are added. These changes stem from the new interactions between the precursor, surfactant, and solvent. A mesostructured hybrid phase composed of building blocks (precursors) and an organized supramolecular template (liquid crystal of surfactants) is generated in the first stage. To give rise to well-organized hybrid mesostructures, a strong interaction between the template and precursor molecules is necessary to form a complex co-assembly and to avoid macroscale phase segregation. In general, the precursors are generated by a sol-gel

process (silane, metal-oxo, or metal-hydroxypolymers) or polymerization (PF sol). The controllable hydrolysis and condensation behavior of the precursors is the key factor in achieving the formation of organized mesostructures. It has been proposed that the organization at the hybrid interface between the precursor and template must be faster than the precursor condensation rate, which leads to a highly organized mesostructure.[27]

From a molecular point of view, electrostatic interactions or hydrogen bonds govern the degree of interactions between the precursors and templates in many cases. To explain this interaction, researchers have proposed four different models, S^+I^-, S^-I^+, $S^+X^-I^+$, and $S^-X^+I^-$, where "S" represents the surfactant, "I" represents the inorganic precursors, and "X" represents a mediator.[44] Considering the interactions between the precursor and template, we can control the morphologies of the resulting mesostructures and draw various morphological diagrams by changing the amount of the precursors in the solution.[45] Figure 1.7 shows that the structural control of mesoporous materials is possible by controlling the amount of sol (precursor) added.[46]

There are three global pathways for obtaining mesostructures based

on the soft-template methods: (1) cooperative assembly or precipitation,[47] (2) "true" liquid crystal templating (LCT),[48] (3) evaporation-induced self-assembly (EISA),[49] which are shown in Figure 1.8. For the cooperative assembly, the mesostructures are generated via the simultaneous assembly of the precursor and surfactant. During the assembly process, a variety of complex concurrent processes, including micelle aggregation and the formation of partially condensed precursor species, emerge before the formation of the mesostructured materials.[50] The coexistence of highly ordered mesostructure and locally ordered domains is possible, and rearrangements between these two phases are responsible for the formation of highly ordered mesostructures upon aging or heating. The final liquid crystalline phase that is surrounded by the precursor is formed and precipitated out of the solution. To obtain a highly ordered porous structure, it is essential to control the condensation of the precursors, which competes with the formation rate of liquid crystals. If condensation takes place before appreciable formation of the liquid crystalline phase, untemplated precursors may form and precipitate separately. In the case of the LCT pathway, the formation of a liquid crystalline phase precedes the condensation of the precursor network.

Similar to a hard-template, the infiltration of the hydrolyzed precursors to the preformed liquid crystalline phase occurs, followed by the formation of the organic or inorganic walls in the hydrophilic region. Although this flexible method is useful for the production of mesoporous nanostructures, the LCT pathway requires special conditions, such as a high concentration of a nonionic surfactant.[51] Moreover, it is quite vulnerable to disruption of the initial lyotropic liquid crystal by the addition of a precursor solution or by the release of alcohols upon hydrolysis. Lastly, the EISA method is closely related to the LCT method, but there are additional interactions at the solid-liquid interface.[32] By beginning with inorganic or organic precursors with low polymerization degrees in volatile polar solvents, self-assembly into moldable precursor-template frameworks is possible. The involved precursors are further hydrolyzed and concentrated to reach CMC conditions during solvent evaporation. In this step, the relative humidity of the surrounding environment can modify the mesostructure.[52] Subsequent condensation of the precursors around the liquid crystal phase finally permits one to obtain a rigid framework.

Table 2. Relationship between the Packing Parameter of Cationic Surfactant and Mesostructure

$g = V/a_0 l \rightarrow$				
$< 1/3$	$1/3 < 1/2$	$1/2 < 2/3$	1	> 1
spherical micelles	cylindrical micelles	3D cylindrical micelles	lamellar micelles	reversed micelles
single-chain surfactants with large headgroups, e.g., $C_nH_{2n+1}N(C_2H_5)_3X$ ($n = 12-18$), $18B_{4-3-1}$, C_{n-s-1} ($n = 12-18$)	single-chain surfactants with small headgroups, e.g., $C_nH_{2n+1}N(CH_3)_3X$ ($n = 8-18$)	single-chain surfactants with small headgroups, e.g., CTAB special surfactants with large hydrophobic polar head and double-chain surfactants with large headgroups and flexible chains, e.g., $C_{16}H_{33}(CH_3)_2N(CH_2)(C_6H_5)$, Gemini C_{m-12-m}	double-chain surfactants with small headgroups or rigid, immobile chains, e.g., $C_nH_{2n+1}N(CH_3)_3X$ ($n = 20, 22$), $C_{16-2-16}$	double-chain surfactants with small groups
		Basic Synthesis		
SBA-6 (cubic $Pm\bar{3}n$)	SBA-7 (3D hexagonal $P6_3/mmc$)	MCM-41 (2D hexagonal $p6mm$)	MCM-48 (cubic $Ia\bar{3}d$)	MCM-50 (lamellar structure)
		Acidic Synthesis		
SBA-1 (cubic $Pm\bar{3}n$)	SBA-2 (3D hexagonal $P6_3/mmc$)	SBA-3 (2D hexagonal $p6mmc$		SBA-4 (lamellar structure)
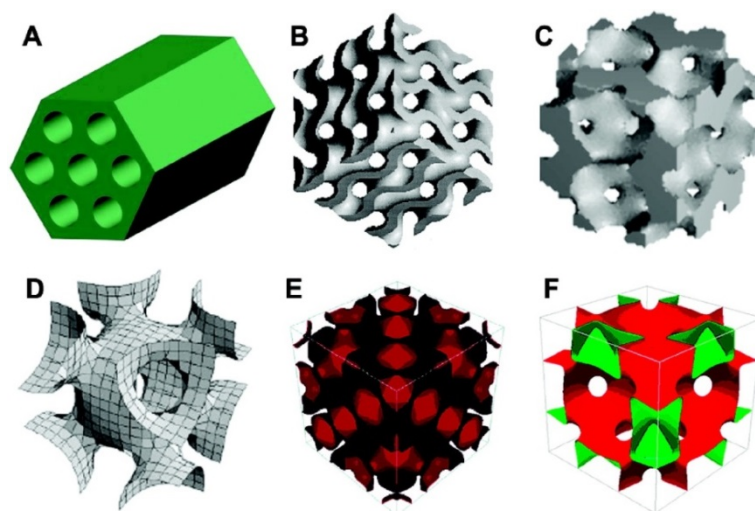
Figure 1.6. The relationship between the packing parameter of cationic surfactant and mesostructure. Pore models of mesostructures with (a) *p6mm*, (b) *Ia$\bar{3}$d*, (c) *Pm$\bar{3}$n*, (d) *Im$\bar{3}$m*, (e) *Fd$\bar{3}$m*, and (f) *Fm$\bar{3}$m* symmetry (from Ref. [43] Wan, Y.; Zhao. *Chem. Rev.* **2007,** *107*, 2821–2860.)
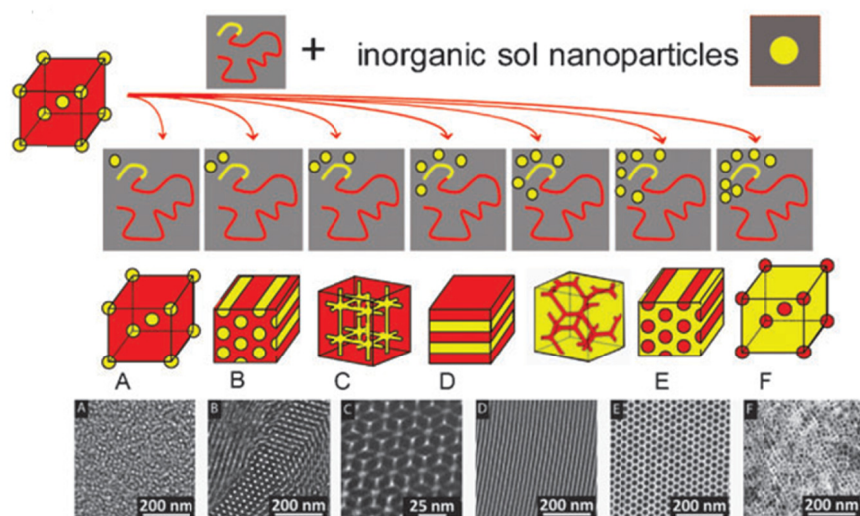
Figure 1.7. Organically modified aluminosilicate nanostructures using block copolymer polyimide (PI)-*b*-PEO as a template (from Ref. [46] Orilall, M. C.; Wiesner, U. *Chem. Soc. Rev.* **2011,** *40*, 520–535.)
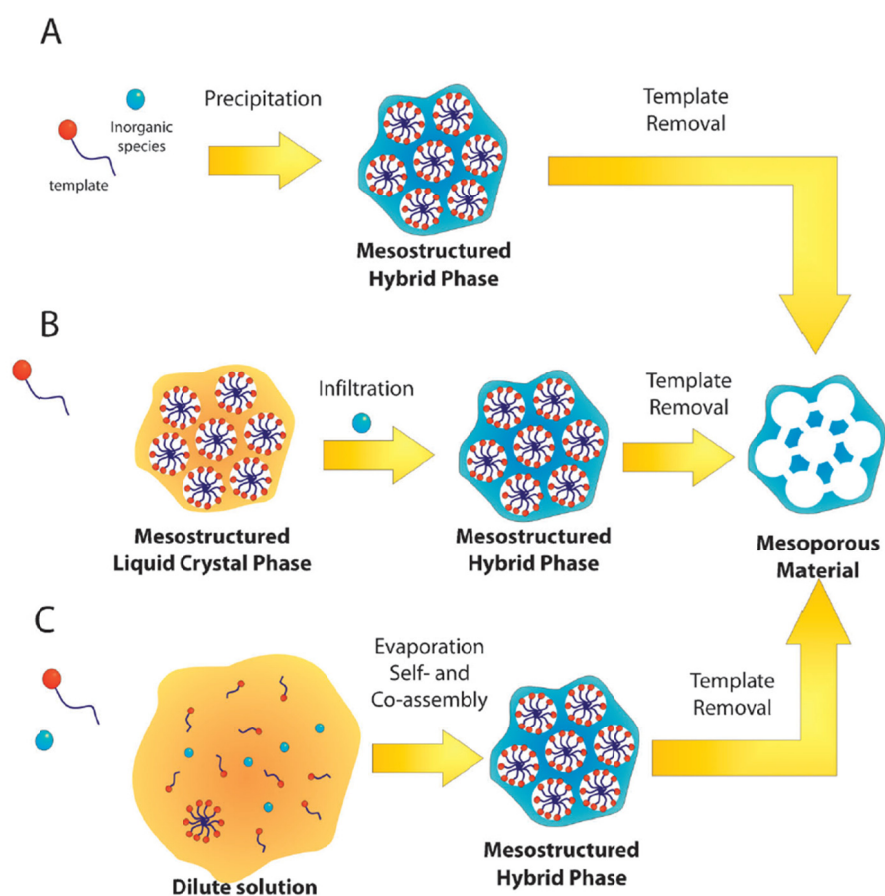
Figure 1.8. Scheme of the synthetic route to mesoporous nanostructures. (a) Cooperative assembly, (b) "true" liquid crystal template (LCT), and (c) evaporation-induced self-assembly (EISA) (from Ref. [27] Soler-Illia, G. J. A. A.; Azzaroni, O. *Chem. Soc. Rev.* **2011,** *40*, 1107–1150.)

1.2.3 Colloidal Nanoparticle Superstructures

While soft-template methods have been developed for the synthesis of many mesoporous materials, they suffer from mesostructure collapse during the annealing step. As a result, the synthesis of fully crystallized metal oxides by the soft-template method is very challenging. To prevent the structural deformation during calcination, the use of preformed and fully crystallized NPs as building blocks instead of molecular precursors has attracted much attention. Such self-assembled NP superstructures can show not only the size- and shape-dependent properties of individual NPs, but also exhibit new collective properties arising from the interactions between neighboring NPs.[53] For example, the assembly of noble metal NPs can induce near-field coupling of surface plasmon between adjacent NPs, which results in the generation of "hot spots."[54] The formation of the NP superstructures can be categorized into two pathways, as shown in Figure 1.9: (i) the *in situ* process, which integrates the formation of individual NPs and self-assembled superstructures in a single step, and (ii) the preformation of individual NPs in separate reactors followed by assembly into a superstructure with the help of a structure-directing agent, such as surfactants and block copolymers.

3 1

Typically, the colloidal NPs with high crystallinity are synthesized and stabilized by a layer of organic capping ligands. Such NPs, which have an inorganic core with hydrophobic surfaces, can be treated as artificial molecules dispersed in an organic solvent. In the *in situ* process, the degree of stabilization derived from the ligands is intentionally reduced to produce the secondary superstructures through the oriented attachment of the primary NPs.[55] This process is also known as "limited ligand protection." The key to form the superstructures is to maintain the appropriate concentration of capping ligands in the solution, which is not sufficient to protect the primary NPs but is sufficient to stabilize the resulting superstructures. As a representative example, Peng *et al.* synthesized three-dimensional nanoflower-like structures of In_2O_3, CoO, MnO, and ZnO.[56,57] The *in situ* method is a convenient and time-saving process compared to other methods requiring multiple steps. However, the successful formation of NPs superstructures through the *in situ* method has been limited to certain examples because it is more challenging than that of the primary NPs. This complex nature can be ascribed to the very narrow concentration window of the capping ligands that results in the formation of colloidal NP superstructures. The precise control of the

porous structure is also difficult because of the rapid growth of the NP superstructures.

The other method for producing NP superstructures is a two-step process, in which the primary NPs are synthesized first and, then, self-assembled using surfactants or block copolymers as structure-directing agents. The mechanism of this process is quite similar to that of the soft-template method. The self-assembly of pre-synthesized NPs through the EISA process can result in the preparation of mesoporous metal oxides with fully crystalline frameworks.[58] Typically, EISA utilizes the oil-in-water emulsion method where pre-synthesized NPs dispersed in an oil phase are emulsified into an aqueous solution with the help of surfactants. This process produces oil droplets of a few micrometers. The NPs in the oil droplets are concentrated and condensed into the superstructures by evaporating the oil phase in the emulsion. The self-assembly is based on the hydrophobic interactions of the capping ligands on the surfaces of the primary NPs. The growth of the colloidal NPs superstructures is driven by the balance between the hydrophobic van der Waals interactions and the steric repulsion force between neighboring superstructures.[59] The surfactant is adsorbed on the surfaces of the

superstructures through hydrophobic interactions and also helps to disperse the superstructures in aqueous solution because of the amphiphilic nature. This facile bottom-up method has demonstrated that the formation of NP superstructures is possible by using various sizes and shapes of NPs as building blocks, including $BaCrO_4$, Ag_2Se, CdS, PbS, Fe_3O_4, $NaYF_4$ nanodots, Bi_2S_3 and LaF_3 nanoplates, and $PbSeO_3$ nanorods.[60] The emulsion-based self-assembly method also has a unique advantage: the incorporation of multiple components into one superstructure, which can result in synergistic interactions. For example, many combinations of metal oxide (support) and metal (catalyst) NP superstructures, such as CeO_2/Pd and TiO_2/Pd, can be fabricated by simply mixing two different types of NPs.[61] Figure 1.10 demonstrates the morphology of the superstructures made from different kinds of preformed NPs. The mesoporous multicomponent colloidal superstructures have also been designed as high-temperature model catalysts. In supported metal catalysts, small NPs tend to aggregate during reaction at high temperature, leading to a reduction in the catalytic activity. However, the unique self-assembled structures exhibit high catalytic activity and thermal stability for both CO oxidation and cyclohexene hydro-conversion.

The other method for producing NPs superstructures is conducted by two-step process, in which the primary NPs are synthesized firstly, and then self-assembled using surfactants or block copolymers as structure-directing agents. The mechanism of this process is quite similar to that of the soft-template method. Self-assembly of pre-synthesized NPs through EISA process can result in the preparation of mesoporous metal oxide with fully crystalline frameworks.[58] Typically, EISA utilize the oil-in-water emulsion method; pre-synthesized NPs dispersed in oil phase are emulsified into an aqueous solution with the help of surfactants. This process produces oil droplet of a few micrometers. The NPs in oil droplet are concentrated and condensed into the superstructures by evaporating the oil phase in the emulsion. The self-assembly is based on the hydrophobic interactions of capping ligands on the surfaces of the primary NPs. The growth of the colloidal NP superstructures is driven by a balance between hydrophobic van der Waals interactions and repulsion steric force between neighboring superstructures.[59] The surfactant is adsorbed on the surfaces of the superstructures through hydrophobic interactions and also helps to disperse the superstructures in aqueous solution due to amphiphilic nature. This facile bottom-up method was

demonstrated that the formation of the NPs superstructures can be possible by using various sizes and shapes of NPs as a building block, including $BaCrO_4$, Ag_2Se, CdS, PbS, Fe_3O_4, $NAYF_4$ nanodots, Bi_2S_3 and LaF_3 nanoplates, and $PbSeO_3$ nanorods.[60] The emulsion-based self-assembly method also has unique advantages of incorporation of multiple components into one superstructure, which can show synergistic interactions. For example, many combinations of metal oxide (support) and metal (catalyst) NPs superstructures, such as CeO2/Pd and TiO2/Pd, were fabricated by simply mixing two different types of NPs at first.[61] Figure 1.10 demonstrates the morphology of resulting superstructures made from different kinds of the preformed NPs. The mesoporous multicomponent colloidal superstructures also designed as a high-temperature model catalyst. In supported metal catalysts, small sized NPs tend to be aggregated during reaction in high temperature, leading to degradation of the catalytic activity. The unique self-assembled structure exhibited high catalytic activity and thermal stability for both CO oxidation and cyclohexene hydro-conversion.
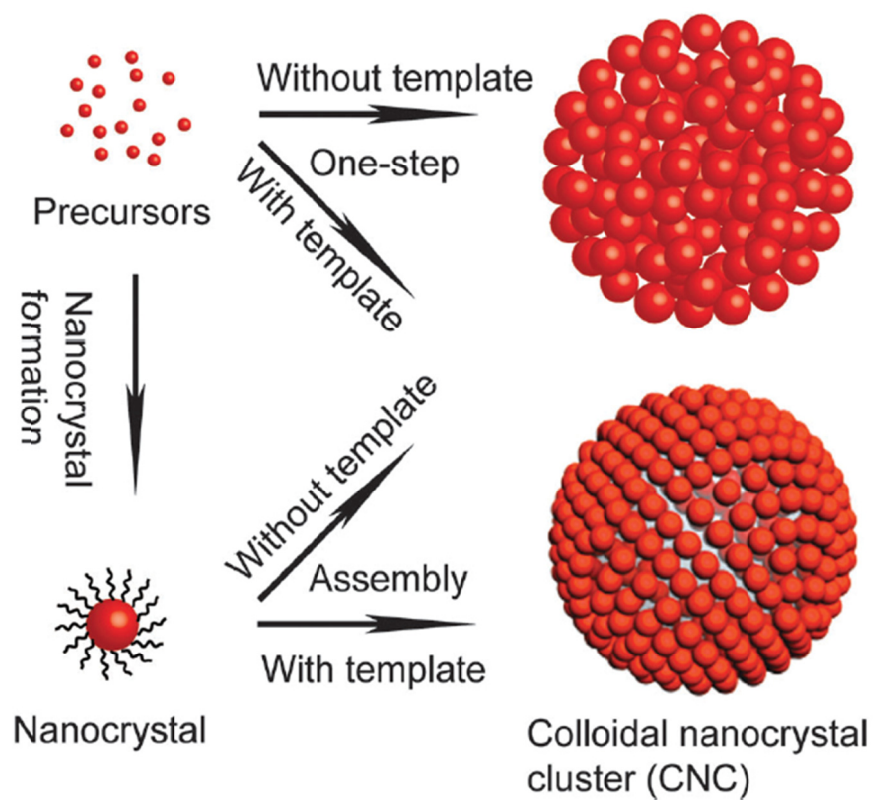
Figure 1.9 Schematic illustration of the preparation method for colloidal NPs superstructures (from Ref. [53] Lu, Z.; Yin, Y. *Chem. Soc. Rev.* **2012,** *41*, 6874–6887.)
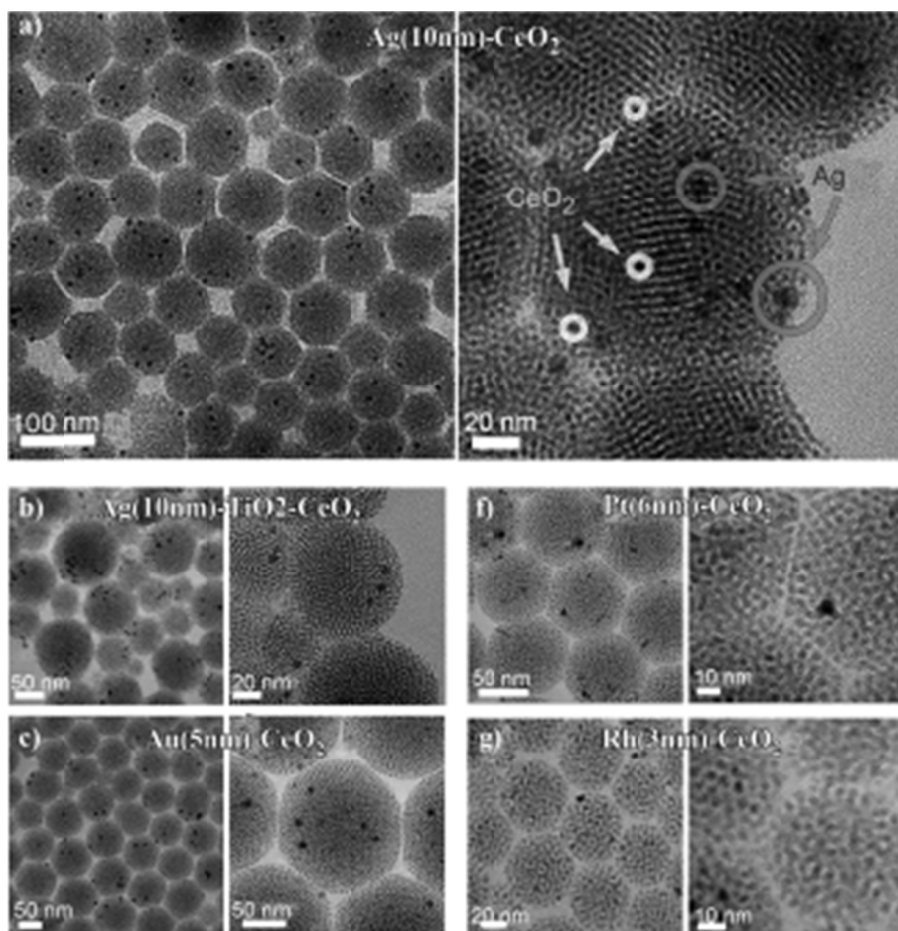
Figure 1.10 A series of TEM images of mesoporous multicomponent nanocomposite colloidal spheres (MMNCS) (from Ref. [61] Chen, C.; Nan, C.; Wang, D.; Su, Q.; Duan, H.; Liu, X.; Zhang, L.; Chu, D.; Song, W.; Peng, Q.et al. *Angew. Chem., Int. Ed.* **2011,** *50*, 3725–3729.)

1.3 Mesoporous Materials for Li-ion batteries

1.3.1 Basics of Li-ion Batteries

Since the Li/TiS$_2$ secondary battery was first introduced in the 1970s, [62] safety problems related to using metallic lithium as an anode electrode have been noted. To replace the dangerous metallic lithium anode and solve the safety issues, many different types of anodes have been developed. In 1991, Sony commercialized the first LIB using graphite as the anode and LiCoO$_2$ as a cathode. In this configuration, lithium is present as ions in the electrolyte, which resolves the excessive formation of dendrites in lithium metal anodes. Over the past two decades, LIBs have become one of the most efficient power storage devices, owing to their long lifespans, high reaction voltages, and low self-discharge.[63] Recently, they have been integrated as the power source for hybrid electric vehicles and electric vehicles.[64] Figure 1.11 demonstrates the operating mechanism of LIBs, which contain a cathode, anode, electrolyte, and separator.[65] During the charging process, Li ions are extracted from the cathode and moved into the anode by passing through the electrolytes. At the same time, electrons are transferred from the cathode to the anode through the

external wires, completing the overall circuit. The discharge process is the reverse of the charging process. For example, the overall reactions using graphite and lithium cobalt oxide can be expressed as:

$$LiCoO_2 \leftrightarrow 0.5\ Li^+ + 0.5\ e^- + Li_{0.5}CoO_2 \quad (Cathode)$$

$$C_6 + Li^+ + e^- \leftrightarrow LiC_6 \quad (Anode)$$
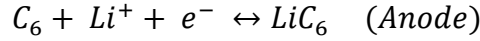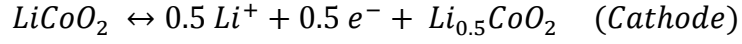
However, LIBs using graphite and lithium cobalt oxide still suffer problems, such as low energy and power densities. Since the early 2000s, nanostructured transition metal oxides have attracted significant attention because of their high theoretical capacity.[66] The reaction between lithium and nanoscale transition metal oxides, the so-called "conversion reaction," is as follows:

$$M_xO_y + 2yLi^+ + 2ye^- \leftrightarrow xM^0 + yLi_2O\ (M = transition\ metal)$$
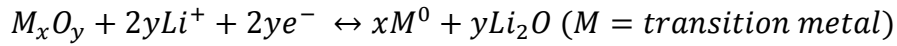
Figure 1.12 demonstrates the conversion reaction of a transition metal oxide in a LIB anode. In the above equation, $2y$ lithium ions can be stored per formula unit of metal oxide through the conversion reaction, causing an amorphization of the transition metal oxides, as well as a large volume expansion. At the end of lithiation, nano-sized transition metal clusters are embedded in the lithium oxide (Li_2O) matrix. During de-lithiation, these transition metal clusters are oxidized to form amorphous transition metal oxides.[67]

In the LIBs, a composite electrode is fabricated by mixing active materials for reaction with Li^+ ions, conductive carbons for electrical contact, and binders for the physical joining of the active materials and conductive carbons. In the case of the conversion reaction, the simultaneous diffusion and transport of Li^+ and e^- into the active metal oxide is a key factor in improving the power density of LIBs. Although many factors influence the rate of transport of the Li^+ and e^-, the rate-determining step is the solid-state diffusion through the active materials.[68] The transport of both electrons and lithium ions is influenced by the morphology and porosity of the nanomaterials.[69] Specifically, lithium-ion diffusion is directly affected by the particle size or pore wall dimension. For ion transport via solid-state diffusion in electrode materials, the following relationship can be established:

$$\tau = L^2 / D$$

where τ is the characteristic time constant for diffusion, L is the diffusion length, and D is the ion diffusion coefficient.[70] Therefore, mesoporous electrode materials can exhibit high rate capabilities by decreasing the lithium-ion diffusion length, in which the nano-sized pore wall structure ensures short diffusion distances.
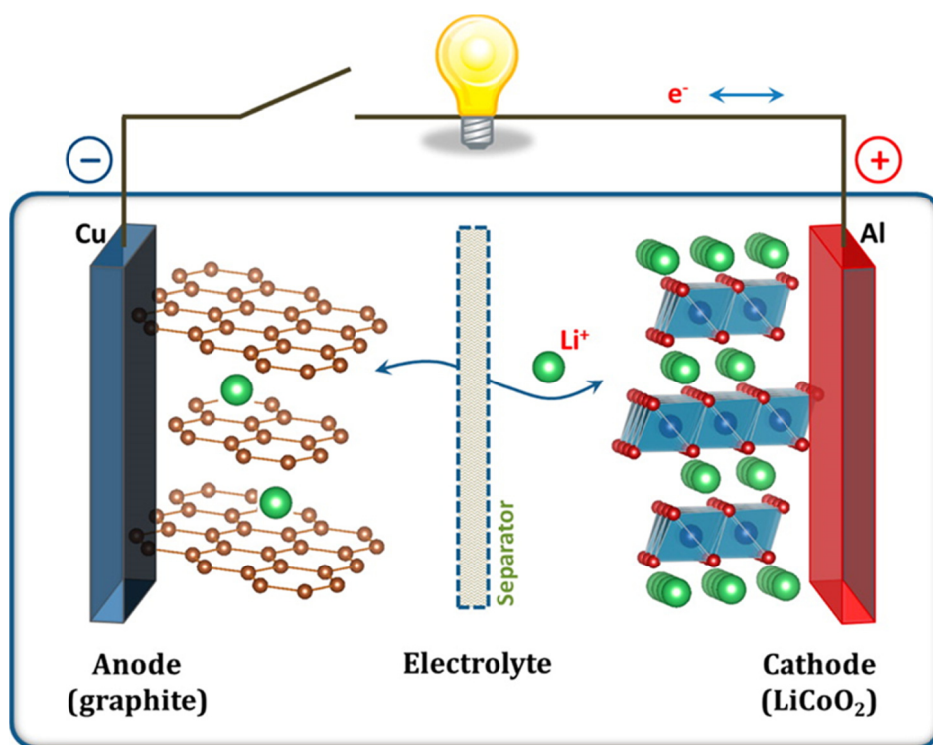
Figure 1.11 Schematic illustration of a lithium-ion battery (LIB) (from Ref. [65] Goodenough, J. B.; Park, K.-S. *J. Am. Chem. Soc.* **2013,** *135*, 1167–1176.)
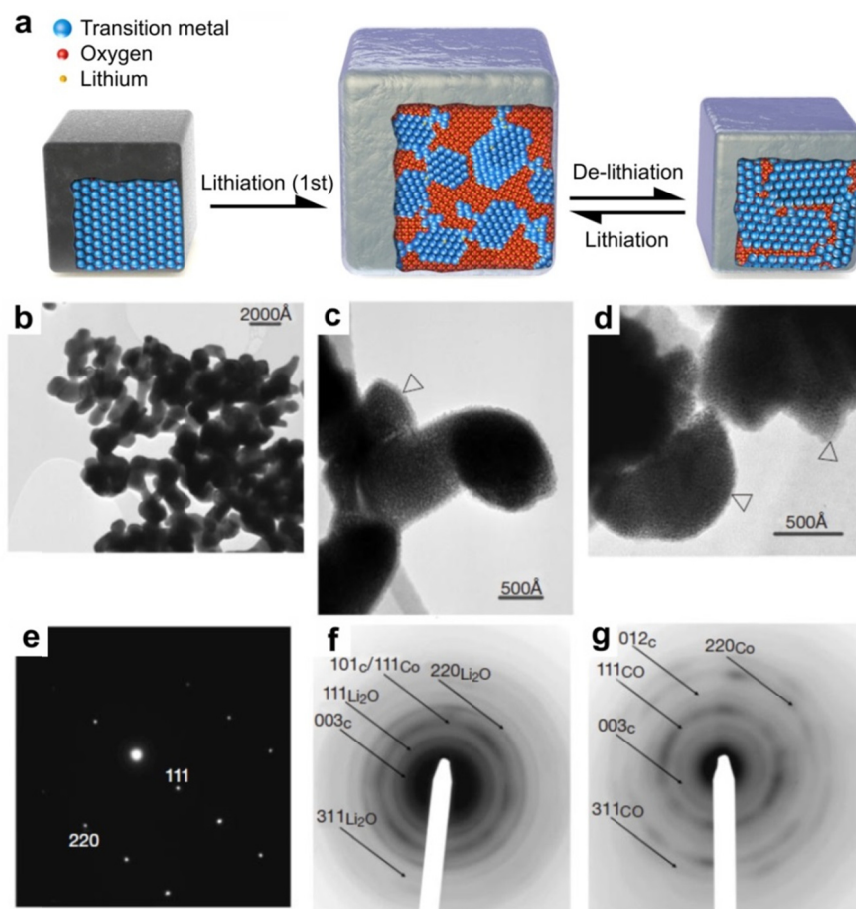
Figure 1.12 Schematic illustration of the conversion reaction of a cobalt oxide in a LIB. Transmission electron microscopy (TEM) images of (b) the starting CoO electrode, (c) the fully lithiated CoO electrode, and (d) a de-lithiated CoO electrode, and (e–g) their corresponding selected area electron diffraction (SAED) patterns. (from Ref. [67] Yu, S.-H.; Lee, S. H.; Lee, D. J.; Sung, Y.-E.; Hyeon, T. *Small* **2016,** *12*, 2146–2172.)

1.3.2 Mesoporous Metal Oxide as Anodes

During the charging/discharging process, the conversion reaction-based active materials suffer from extensive volume expansion because the size of the Li^+ ions being added/extracted is comparable with the overall size of the metal oxide lattice.[71] The mesoporous structure can provide empty spaces, which can alleviate this volume expansion and prevent the pulverization of the active materials during long cycles. Recently, Park *et al.* proposed a model explaining how to alleviate the volume expansion in the course of lithiation by conducting *in operando* small angle X-ray scattering.[72] Figure 1.13 demonstrates three different models for the structural deformation upon the volume expansion of three electrodes during the charging/discharging process. In the case of the mesoporous Co_3O_4, there is direct evidence that the mesoporous void volume acts as a buffer, successfully accommodating the volume expansion of the active material upon based on the conversion reaction. However, the partial loss of the mesostructure was also detected because of the phase transition during the charge/discharge process.
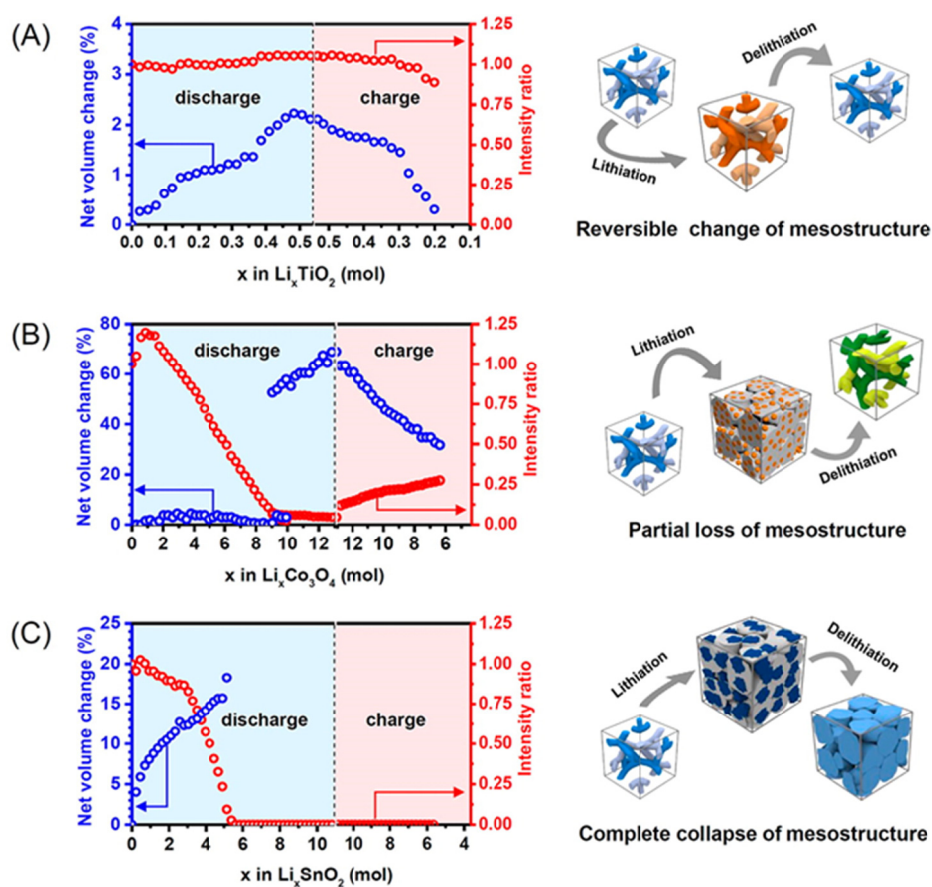
Figure 1.13 Schematic illustration of pore dynamics in the ordered mesoporous metal oxide electrodes. **(**a) meso-TiO$_2$ (b) meso-Co$_3$O$_4$, and (c) meso-SnO$_2$ (from Ref. [72] **P**ark, G. O.; Yoon, J.; Park, E.; Park, S. B.; Kim, H.; Kim, K. H.; Jin, X.; Shin, T. J.; Kim, H.; Yoon, W.-S.et al. *ACS Nano* **2015,** *9*, 5470–5477.)

1.3.3 Solid-Electrolyte Interphase (SEI) Formation and Control

Although the mesoporous nanostructure can provide a short Li^+-ions diffusion distance, thus enhancing power density, accommodating volume expansion, and maintaining electrochemical stability, a high surface area and exposure of edge sites can result in excessive reactions in the LIB electrode. As mentioned above, the SEI layer forms on the active material surfaces during LIB operation owing to side reactions with the electrolyte, solvent, and salt. In LIBs, an aprotic salt solution with low molecular weight organic solvents is the most utilized combination for making electrolytes. Figure 1.14 shows the relative electron energies of the anode, electrolyte, and cathode in a LIB.[73] The stability window of the electrolyte is the difference between the lowest unoccupied molecular orbital (LUMO) of the anode and the highest occupied molecular orbital (HOMO) of the cathode. The organic electrolytes used in LIBs have oxidation potentials of around 4.7 V (vs. Li^+/Li) and a reduction potential close to 1.0 V (vs. Li^+/Li). The energy gaps between the anode and cathode must be as high as possible to maintain a high output voltage and increase the energy density. Therefore, the reaction potential of the metal oxide is as low as 0.2 V (in the case of manganese oxide), which

is below the reduction potential. SEI formation occurs mainly during the first charge process, owing to the exposure of the bare surfaces of the anode and the high electron transfer ability of the anode. Figure 1.15 illustrates the formation of an SEI layer on the graphite anode with different solvents in the electrolyte.[74] During the first charge/discharge process, about 15% of original capacity is generally consumed in the irreversible SEI formation.[75] The key factors for SEI formation depend on the composition and morphological structure of the active materials, including particle size, basal-to-edge plane ratio, pore size, and degree of crystallinity.[76] Because the particle size is small, the irreversible capacity loss increases because of the larger surface area-to-volume ratio for lithium inventory loss during SEI formation. In addition, the SEI formation begins at the edge sites more rapidly than at the basal planes because of the chemical reactivity of the edge sites. The edge sites have more uncoordinated atoms on the surfaces, which can result in the active decomposition of the solvents and electrolytes. This process is also applicable to the mesoporous materials, which have a large surface area and nano-sized pore wall structure with plenty of edge sites. When the mesoporous materials are used as the anode material, the SEI layer gradually grow thicker

during repeated charge/discharge cycles. The gradual thickening of the layer further consumes Li^+ ions, electrolyte, and Li salts, leading to increases in the overall resistance of the electrode. The increase in the anode potential is also attributed to a lower number of Li^+ ions in the electrode after SEI formation. Therefore, the formation of a compact and conformal SEI coating on the anode is vital to prevent further undesired decomposition of the electrolyte during the first charge process. Ideal SEI layer properties include high electrical resistance to prevent successive SEI formation and high Li^+-ion conductivity to permit Li^+-ion access to the anode material.[77] In addition, the SEI layer must endure the expansion and contraction stress during charge/discharge process. The chemical composition of the SEI layer has been demonstrated to have a bilayer type structure. Zhang *et al*. fabricated MnO films on Ti substrates using pulsed laser deposition to quantify the mechanical properties of the SEI layer.[78] Atomic force microscopy (AFM) and force spectroscopy were performed in a vacuum to prevent exposing the SEI layer to air. The as-deposited MnO films exhibit a granular morphology with a surface roughness of ca. 12 nm (Figure 1.16.a). When two MnO electrodes were discharged at 0.8 and 0.3 V, the SEI layer was precipitated with a surface

roughness varying over the range of 14–17 nm (Figure 1.16.b,c). In these two samples, the SEI layer responded to external mechanical forces with an initial elastic deformation followed by plastic yield. In addition, the SEI layer in these samples exhibits a single-layer structure of 43-nm thickness with a Young's modulus of 1.1 GPa. This value is much higher than those of usual organic materials, so the inorganic SEI layer can be characterized as compact and hard. When the electrode was discharged at 0.1 and 0.01 V, the surface grain size and roughness started to increase drastically to the range of 65–280 nm (Figure 1.16.d,e). The SEI layer in these samples also shows initial elastic deformation followed by plastic yield, but another set of elastic and yield regions was also clearly observed, indicating a double-layer structure. A Young's modulus of 16 MPa and a thickness of 40 nm for the outer layer and a Young's modulus of 540 MPa and a thickness of 70 nm for the inner layer were determined. The inner layer corresponds to hard inorganic materials, and the soft outer layer is likely to be composed of organic materials in a double-layer structure, demonstrating that one-electron and two-electron reductions occurred simultaneously. Finally, when the electrode was charged again to 3.0 V (Figure 1.16.f), the SEI layer changed back to a thickness of

approximately 9 nm with a Young's modulus >1 GPa. As a result, the unstable soft organic SEI layer decomposed during the charge process, whereas the inorganic SEI layer remained partially intact. It is quite noticeable that the distribution of the SEI layer on the electrode surface is highly inhomogeneous. In mesoporous materials with a nano-sized pore wall structure, the control of SEI layer formation is much more difficult owing to the extremely high surface-to-volume ratio and edge-to-basal plane ratio. Therefore, proper strategies to achieve controllable SEI layers on the mesoporous materials must be developed to improve the initial irreversible capacity loss, rate capability, and safety.[79]
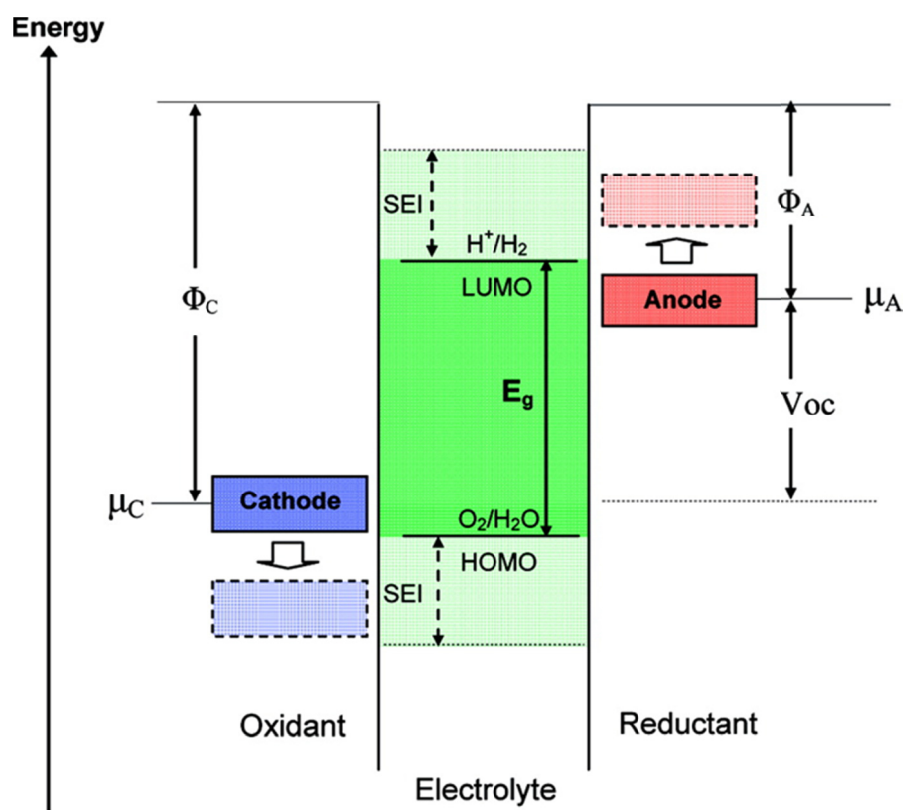
Figure 1.14 Energetics of the formation of an SEI layer on the anode and cathode under reductive and oxidative conditions (from Ref. [73] Goodenough, J. B.; Kim, Y. *Chem. Mater.* **2010,** *22*, 587–603.)
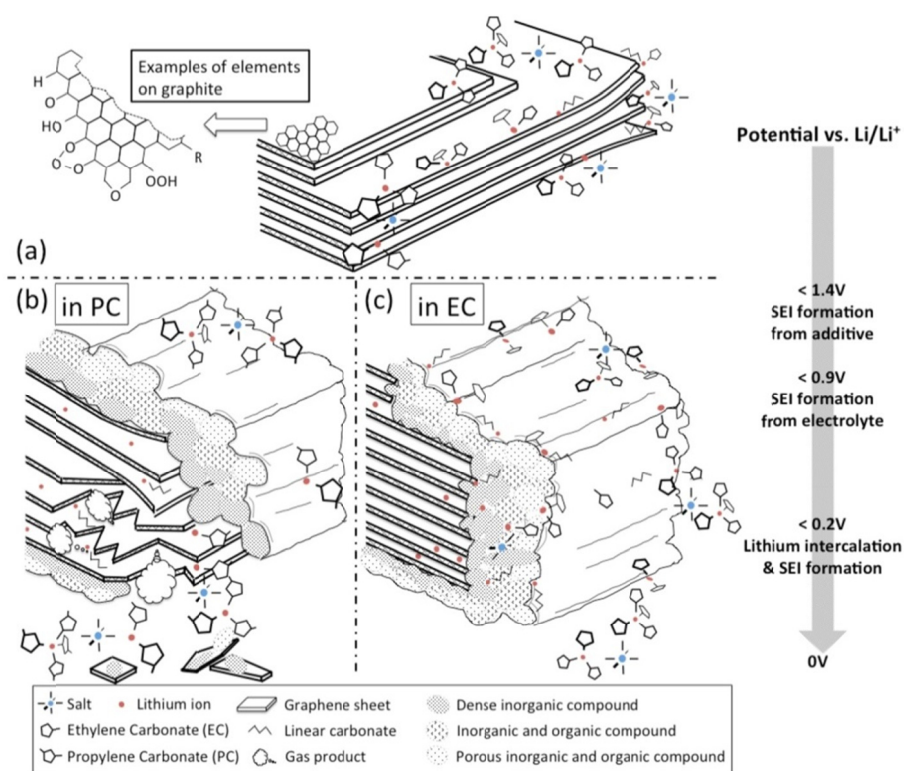
Figure 1.15 Schematic illustration of the formation of an SEI on the anode: (a) graphene layer above 1.4 V vs. Li/Li$^+$ and (b) SEI formation in propylene carbonate (PC) solvent. Below 0.9 V vs. Li/Li$^+$, intercalation of Li$^+$ ions with PC molecules leads to graphene exfoliation: (c) stable SEI formation in ethylene carbonate (EC)-based solvent. (from Ref. [74] An, S. J.; Li, J.; Daniel, C.; Mohanty, D.; Nagpure, S.; Wood, D. L. *Carbon* **2016,** *105*, 52–76.)
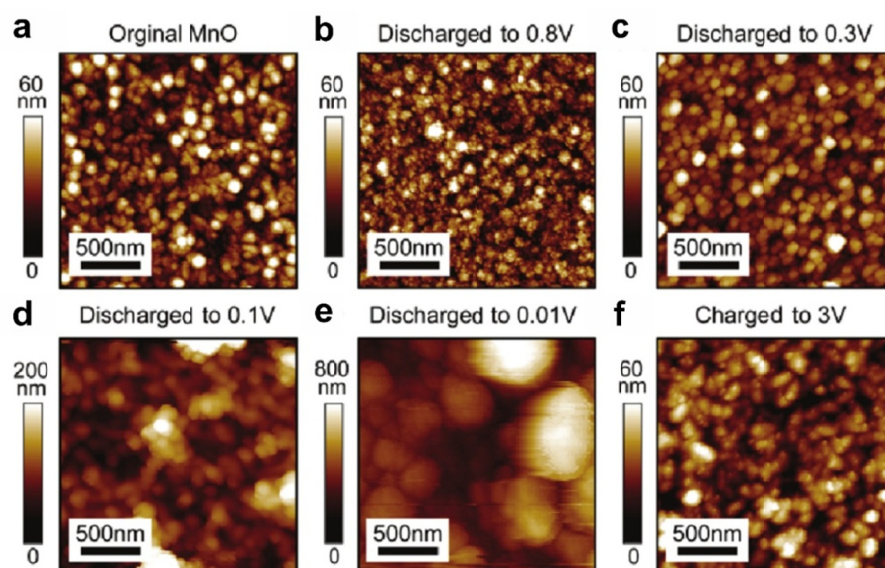
Figure 1.16 AFM images of an MnO electrode surface during the first cycle (a) before electrochemical tests, (b) at 0.8 V, (c) at 0.3 V, (d) at 0.1 V, (e) at 0.01 V during discharge, and (f) at 3 V after charge. (from Ref. [78] Zhang, J.; Wang, R.; Yang, X.; Lu, W.; Wu, X.; Wang, X.; Li, H.; Chen, L. *Nano Lett.* **2012,** *12*, 2153–2157.)

1.4 Mesoporous Materials for Fuel Cells

1.4.1 Fuel Cell Fundamentals

A fuel cell is an energy conversion device that generates electricity from the electrochemical reaction of oxygen and hydrogen.[80] In the anode, the hydrogen oxidation reaction (HOR) occurs with a low overpotential in comparison to the cathode reaction, the oxygen reduction reaction (ORR). The ORR is an extremely sluggish reaction with a 10-times larger overpotential than that of the HOR. The ORR in aqueous solution is highly irreversible and includes multiple adsorption/desorption reaction steps involving O, OH, O^{2-}, HO^{2-}, and H_2O_2, which make hard to understand exact mechanism.[81] The mechanism of the ORR involves the net transfer of four electrons and four protons to O_2 and the cleavage of the double bond of O_2. As the ORR process is regarded as the kinetically limiting factor of several devices depending on the oxygen electrochemistry, the overpotentials of the ORR must be zero relative to the thermodynamic reduction potential of O_2, which can be described as follows:

$$O_2 + 2H_2O + 4e^- \leftrightarrow 4OH^-; \; E^0 = 0.401 \; V \; vs \; SHE \; \text{(in basic condtion)}$$

$$O_2 + 4H^- + 4e^- \leftrightarrow 2H_2O; \; E^0 = 1.229 \; V \; vs \; SHE \; \text{(in acidic solution)}$$
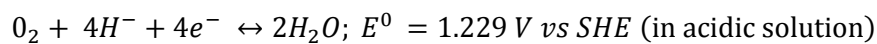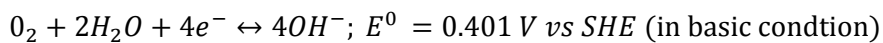
The standard reduction potential is described with reference to the standard hydrogen electrode (SHE) for the direct four-electron pathway in acidic and basic solutions.

The potential and current are commonly utilized as fundamental descriptors of the electrochemical reaction. In nonstandard conditions, the equilibrium potential of the oxygen electrode reactions is defined according to the Nernst equation.

$$E_{eq} = E^0 + \frac{nF}{RT} \left(\sum_i \ln a_i^0 - \sum_j \ln a_j^R \right)$$

Here, E_{eq} is the equilibrium potential, E^0 is standard potential, n is the number of electrons, F is the Faraday constant, R is the ideal gas constant, a_i^0 is the activity of the oxidants, and a_j^R is the activity of the reductants.

The current is expressed by the sum of the reaction rates, coming from the anode and cathode. Considering the low solubility of O_2 in aqueous solution (1.26×10^{-3} mol L^{-1}), the evaluation of ORR activity can utilize the convective or forced transport of reactants in the solution. The rotating-disk electrode (RDE) technique is frequently used to measure the activity of the ORR process. Figure 1.17 illustrates a typical RDE set-up in a three-electrode system, and ORR

polarization curves have been collected using the RDE technique.[82] Generally, performance indicators, such as the onset potential (E_{onset}), half-wave potential ($E_{1/2}$), overpotential under a specific current density (η_j), and diffusion-limiting current density (j_L), are reported in the literature The electrochemical properties of RDE can be described using the Koutecky–Levich (K-L) equation:

$$\frac{1}{j} = \frac{1}{j_L} + \frac{1}{j_K} = \frac{1}{0.62nFC_0D_0^{2/3}v^{1/6}w^{1/2}} + \frac{1}{nFkC_0}$$

where j_K is the kinetic-limiting current density, w is the angular velocity, v is the scan rate, C_0 and D_0 are the bulk concentration and diffusion coefficient of the electrolyte, respectively, and k is the electron-transfer rate constant. By using the K-L equation, we can calculate n and k from the slope and intercept, respectively.

To find the exact reaction pathway of the multiple step ORR process, the use of the rotating ring-disk electrode (RRDE) technique is dominant.[83] The RRDE can detect the products generated from the disk electrode through a nearby coaxial ring electrode. Figure 1.18 shows a typical RRDE curve of a Pt/C electrode in a basic solution. The current related to HO_2^- re-oxidation ($X_{HO_2^-}$) is also recorded in the ring current, and the corresponding electron transfer numbers (n_{e^-})

during the ORR process are calculated as follows:

$$X_{HO_2^-} = \frac{2I_R/N}{I_D + I_R/N}$$

$$n_{e^-} = \frac{4I_D}{I_D + I_R/N}$$

where I_R is the ring current, I_D is the disk current, and N is the collection efficiency.

If we assume the ORR process at equilibrium, the η-j characteristic is correlated with Butler–Volmer equation:

$$j = j_0\left[\exp\left(\frac{\alpha_a nF\eta}{RT}\right) - \exp\left(-\frac{\alpha_c nF\eta}{RT}\right)\right]$$

where j_0 is the exchange current density at equilibrium potential, and α_a and α_c are the charge transfer coefficients in the anode and cathode, respectively. Considering that the ORR process is almost irreversible, the observed ORR currents (j) at a high overpotential ($|\eta|$ > 50 mV) can be regarded as follows:

$$j_c = -j_0\exp(-\frac{\alpha_c nF\eta_c}{RT})$$

$$\eta_c = \frac{RT}{nF\eta_c}\ln j_0 - \frac{RT}{nF\eta_c}\ln j = a - b\ln j$$

where b is the Tafel slope, which is a direct indicator of the reaction mechanism (based on its value). For example, a b value of -60 mV dec^{-1} in basic solution can be interpreted as a pseudo two-electron reaction as the rate-determining step (RDS). In addition, a b value of -120 mV dec^{-1} corresponds to the first-electron reduction of O_2 as the RDS.[84]
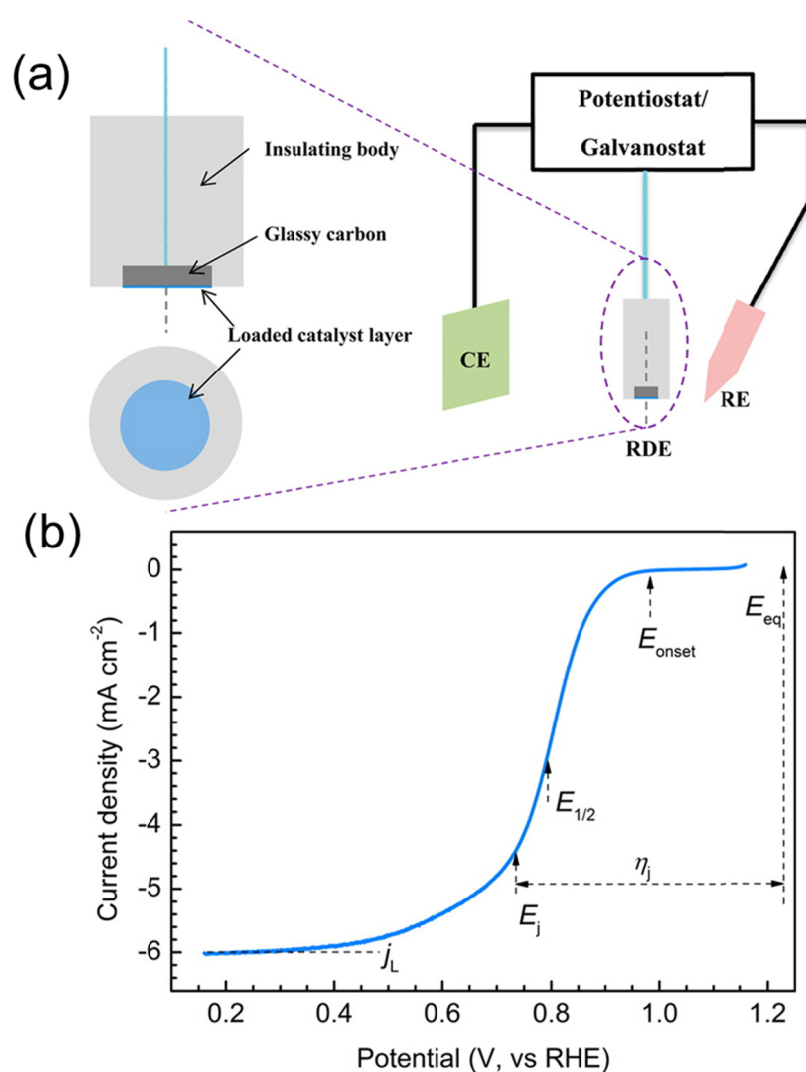
Figure 1.17. (a) Schematic illustration of a typical RDE setup in three-electrode configuration (b) A representative example of an ORR polarization curve from the RDE system (from Ref. [82] Ge, X.; Sumboja, A.; Wuu, D.; An, T.; Li, B.; Goh, F. W. T.; Hor, T. S. A.; Zong, Y.; Liu, Z. *ACS Catal.* **2015,** *5*, 4643–4667.)
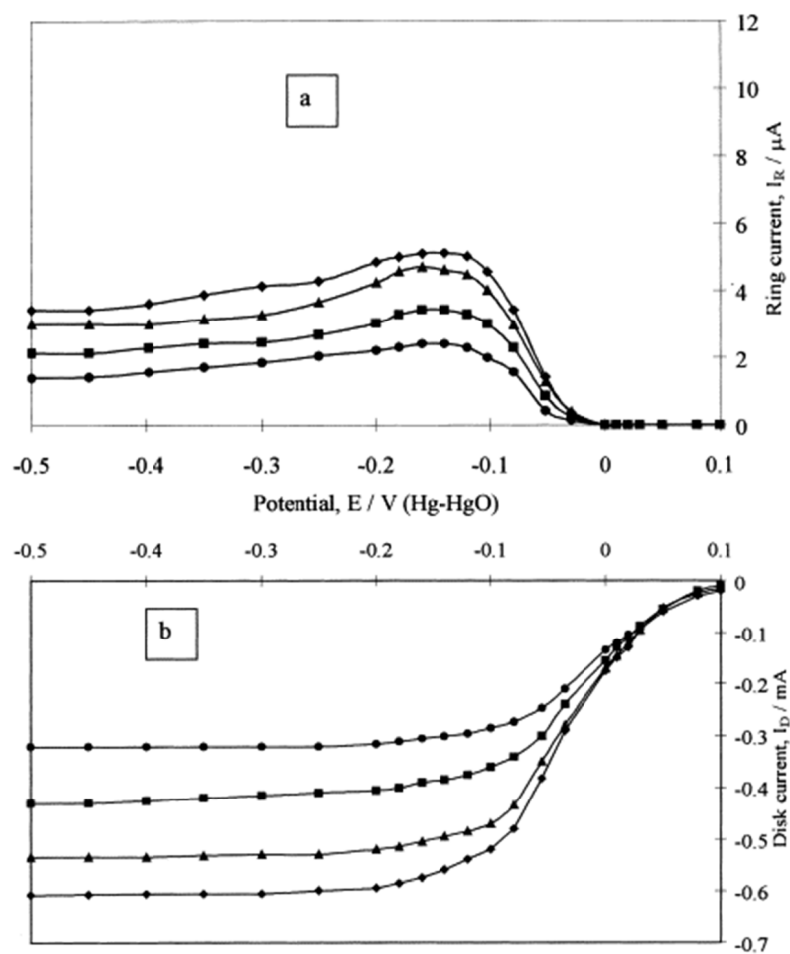
Figure 1.18. (a) Current–potential curves for O$_2$ reduction on 20 wt% Pt/C in 1 M NaOH solution and for (**b**) HO$_2^-$ reoxidation on a Pt ring electrode (from Ref. [83] Geniès, L.; Faure, R.; Durand, R. *Electrochim. Acta* **1998,** *44*, 1317–1327.)

1.4.2 Fe-N-C catalysts for Oxygen Reduction Reaction

Pt is the most efficient ORR electrocatalyst because of its moderate intrinsic interactions with reaction intermediates. Because there are many complex interrelationships between the oxygen species intermediates during the ORR process, the moderate chemisorption energy is important.[85] However, the high cost and scarcity of Pt-based ORR catalysts are the main drawbacks for the large-scale commercialization of fuel cells as renewable energy sources. In 1964, Jasinski *et al.* reported that cobalt phthalocyanine showed high ORR catalytic performance in alkaline electrolytes and this seminal work provoked extensive research into the development of Pt-free ORR catalysts.[86] Among them, Fe-N-C catalysts have gained much attention because of their superior ORR activity in acid and alkaline electrolytes, low-cost precursor materials, and facile synthesis.[87] The structure of the Fe-N-C catalyst can be described as heterogeneous ensembles of in-plane coordinated Fe atoms bonded to nearby N atoms embedded in a graphene-type matrix, such as $Fe-N_4/C$[88] or $Fe-N_{2+2}/C$.[89] Previous theoretical calculations predicted that the rehybridization of the Fe 3d orbitals with the ligand N orbitals coordinated from the axial direction results in a significant change in

the electronic and geometric structure, which can increase the ORR catalytic activity greatly.[92] In addition, the π-conjugated carbon basal plane can tune the downshift in the e_g-orbitals (d_z^2) of the metal ion through the electron-withdrawing nature of the carbon support. This delocalized π-electron can shift the redox potential of metal ion anodically by about 600−900 mV, leading to superior ORR activity.

The identification of the exact active site in the Fe-N-C structure still remains elusive because of the heterogeneous ensembles of active sites in the catalysts. Currently, two ORR active sites have been proposed: the edge plane FeN_4/C species and $N-Fe-N_{2+2}/C$ species, which display catalytic activity for the ORR in acidic medium.[90] Figure 1.19 illustrates the proposed structures of the active sites identified by ^{57}Fe Mössbauer spectroscopy. The authors insisted that the D3 state is the most active species because the protonated neighboring basic nitrogen can relay protons to the active site. This proton relay near the redox center in the second coordination sphere of the iron-porphyrin structures has a high selectivity for the $4e^-$ reduction pathway to H_2O.[91] The catalytic active sites are embedded in the edge sites, which can form from the gaps between two crystalline graphite sheets. Because the size of the gaps between two

graphite edge sites is in the micropore regime, the ORR activities of the Fe-N-C catalysts are linearly correlated with the surface area of the micropores. To investigate the reaction pathway of the ORR on Fe-N-C catalysts, first-principles density functional theory (DFT) calculation have been performed, which indicate that the ORR proceeds as follows: (1) $O_2 \rightarrow *O_2$ (adsorption); (2) $*O_2 + (H^+ + e^-) \rightarrow *OOH$; (3) $*OOH + (H^+ + e^-) \rightarrow 2*OH$; (4) $2*OH + 2(H^+ + e^-) \rightarrow 2H_2O$.[92] Apart from the theoretical calculations, an experimental demonstration of the ORR mechanism of the Fe-N-C catalysts was conducted, and the inner- *vs.* outer-sphere electron transfers were elucidated.[93] Figure 1.20.a illustrates the inner-sphere electron transfer (ISET) and outer-sphere electron transfer (OSET) mechanisms during the ORR in alkaline media. The well-known ISET mechanism includes direct chemisorption of desolvated O_2 on the active site, resulting in a 4e⁻ ORR pathway without the desorption of reaction intermediates. In contrast, the OSET mechanism coexists with the ISET mechanisms in the alkaline electrolyte, where the non-covalent hydrogen bonding between adsorbed hydroxyl species (*OH) and solvated O_2 in the outer-Helmholtz plane can proceed via a 2e⁻ ORR pathway forming HO₂⁻

6 3

anions. As depicted in Figure 1.20.b, the Fe-N$_4$/C active site can promote the 4e$^-$ ORR pathway through the ISET mechanisms, where O$_2$ displaces the OH$^-$ species and adsorbs directly on the Fe^{2+} active sites by forming ferric-hydroperoxyl adducts. The stability of this Lewis acid-base adduct determines the selectivity of the ORR process in various pH electrolytes. At pH > 12, the Lewis basic nature of the HO$_2^-$ anions (pK_a ≈ 11.6) can result in its apparent stabilization on the Lewis acid Fe^{2+} active sites, leading to complete 4e$^-$ pathway. However, in acidic media, the analogous ferric-hydroperoxyl adduct will be Fe^{2+}−(OHOH), where the protonated nature of the hydrogen peroxide intermediate (H$_2$O$_2$) mitigates its Lewis basic characteristics. This destabilization of the Lewis acid-base adducts on the Fe^{2+} active site leads to the higher overpotential for the ORR and requires secondary sites for the further reduction or disproportionation of H$_2$O$_2$. Therefore, the ORR active sites of the Fe-N-C catalysts are more active in alkaline media than in acid media.

Figure 1.19. Side and top view of the proposed structure of the Fe-N-C catalyst: (a) FeN$_4$/C site assigned to a doublet D1 state. (b) the FeN$_{2+2}$/C site assigned to a doublet D2 state, and (c) N-FeN$_{2+2}$/C site assigned to a doublet D3 state. (from Ref. [90] Kramm, U. I.; Herranz, J.; Larouche, N.; Arruda, T. M.; Lefevre, M.; Jaouen, F.; Bogdanoff, P.; Fiechter, S.; Abs-Wurmbach, I.; Mukerjee, S.; Dodelet J.-P. *Phys. Chem. Chem. Phys.,* **2012,** *14*, 11673–11688.)

Figure 1.20. (a) Schematic illustration of the inner-sphere (inset i) and outer-sphere (inset ii) electron transfer mechanisms during the ORR in alkaline electrolyte (IHP, inner Helmholtz plane, OHP, outer Helmholtz plane) (b) Proposed ORR mechanism on Fe-N-C catalyst active sites in alkaline media. (from Ref. [93] Ramaswamy, N.; Tylus, U.; Jia, Q.; Mukerjee, S. J. Am. Chem. Soc. 2013, 135, 15443–15449.)

1.4.3 Mass transfer in Fe-N-C catalysts

Through the above mechanisms, the ORR performance of the Fe-N-C catalysts greatly depends on the preparation conditions.[94] The different degrees of ORR performance may result from the coupling between the mechanistic steps and the transport of the intermediate species toward the catalytic surface.[95] The transport phenomena in porous ORR catalysts have attracted great attention because of the potential to increase the catalyst activity by catalyst modification. The increase in activity on porous ORR catalysts has been assumed to originate from the huge increase in the surface area.[96] For example, Wang *et al.* reported that N-doped mesoporous carbon spheres with tunable pore sizes showed superior ORR activity in alkaline media.[97] Such an enhancement in activity may originate from the optimum pore size, but there is a missing link explaining the effect of pore size on the ORR activity. Many other researchers have suspected that the enhancement of the activity may be attributed to improved mass transport properties in the electrodes.[13] However, the detailed mechanisms and quantitative data concerning the mass transport properties in the porous electrode have remained elusive because of difficulties in measuring the mass properties at the nanoscale.

Therefore, the transport of the substrate and products to and from the catalytic active centers is an emerging issue because they participate in the control of the catalytic efficiency of porous electrodes.[24] In this respect, the interesting properties of porous catalysts stem from the numerous, nanoscale confined spaces in the porous structure. The confined nanopores provide unique conditions for reactants, including delayed mass transport, electric double layer (EDL) overlap, and enhanced reaction probability.[98] Figure 1.21 illustrates that molecular species in the nanopores reside longer within an effective distance of the catalyst surface than that of a flat catalyst surface. In the kinetically controlled region of the ORR process, electron transfer to O_2 can determine the overall current densities and be controlled by how long an O_2 molecule resides on the catalyst surface. Specifically, longer residence times within an effective distance of the catalyst surface results in more probable electron transfers. Therefore, a porous structure can enhance the electrokinetics in the ORR, which has a sluggish reaction rate because of the multi-electron transfer. Such molecular motion in the pore can be explained by Knudsen diffusion (Figure 1.21.b) and Brownian motion (Figure 1.21.c). The Knudsen diffusion can be applied to explain molecular dynamics in the

nanopore when the mean free path of a molecule is sufficiently long compared to the pore size.[99] The molecules in the Knudsen regime are more likely to collide with the inner walls of the pores, and this behavior is predominant for mesopores (2–50 nm in pore size). Brownian motion can also explain the molecular dynamics when the mean free path is relatively short in comparison to the pore size, and the pathway is random.[100]

If a sufficient overpotential is applied to the electrode, ORR reactions take place as soon as the O_2 molecule reaches the catalyst surface. In this case, the collision frequency is negligible for the overall current density because of the very fast electron transfer to the reactant molecules. Instead, in the mass-transport limited regime, a concentration gradient in the diffusion layer determines the overall activity. Narrow nanopores and a complex porous structure restrict the molecular diffusion in the bulk solution, leading to an increase in the solution resistance. In such conditions, there is optimal pore size for the most effective mass transport.[101] This impeded mass transfer can enhance the $4e^-$ pathway selectively by increasing the collision frequency in the Fe-N-C catalyst during the ORR process.[102] The small amount of catalyst in the electrode thin film producing a fraction

of H_2O_2 (product of 2e⁻ pathway) increases. In contrast, high loads of the catalyst result in a higher chance of going through the 4e⁻ pathway before H_2O_2 intermediates diffuse out of the bulk electrolyte. Although the nanoporous materials suffer from delayed mass transport in the bulk solution, the porous structure can provide more facile diffusion kinetics for the reactant molecules in the diffusion layer. The mesopores are separated by the pore wall structure, which has dimensions of a few nanometers. In this scenario, the reactant molecules in the nanopores can experience a very short diffusion layer thickness, where the diffusion rate can increase significantly. If the distance between two active sites is sufficiently large, the diffusion layer thickness will be on the order of the nanometers, which can match the pore size.[103] As a demonstration, the acceleration of reactant diffusion is of the order of 1000 in the case of nanoparticles with a 10-nm radius because of the shortened diffusion layer.[95] Considering that the diffusion thickness to the planar electrode under moderate stirring or natural convection is of the order of 10^{-3} cm,[104] the diffusion rate in the diffusion layer could be much larger than that achievable through forced convection at the macroscale.[105] As a result, the mesoporous nanomaterial can provide not only large

collision frequency derived from confined porous structure but also the acceleration of the rate in the diffusion layer.
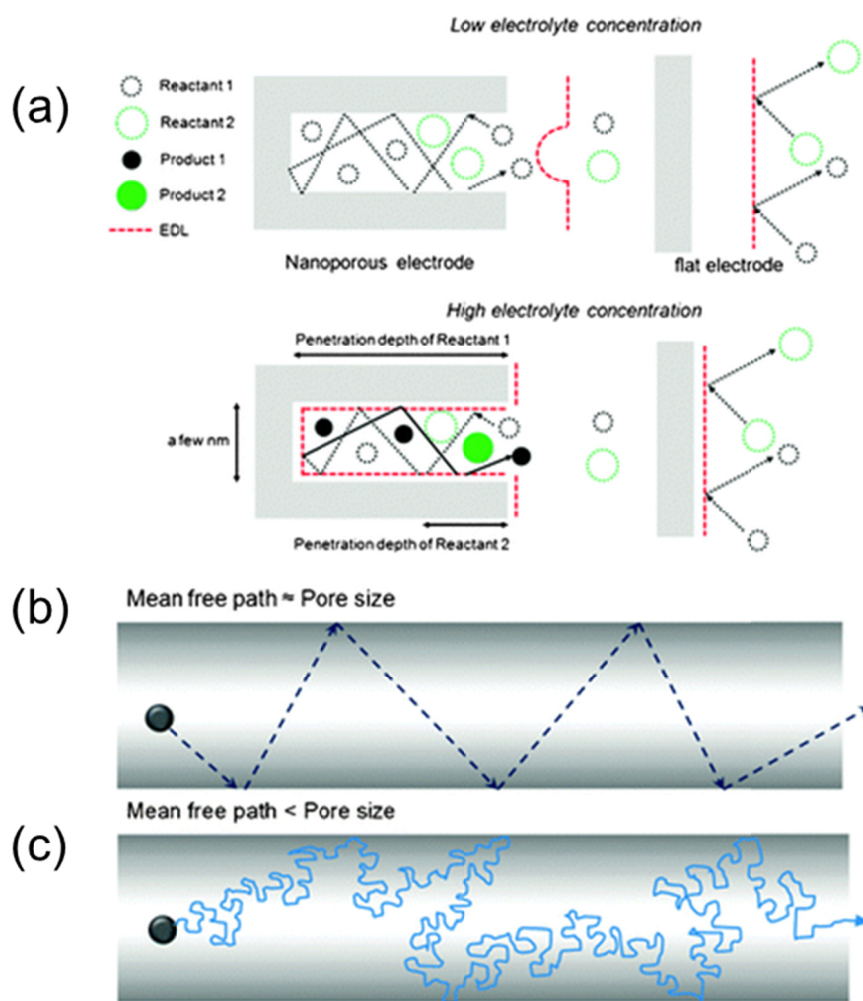
Figure 1.21. (a) Schematic illustration of the movement of molecules inside pores and flat surfaces (b) Schematic illustration of Knudsen diffusion in a nanopore (c) Schematic illustration of the nano-confined molecular dynamics of Brownian motion (from Ref. [98] Bae, J. H.; Han, J.-H.; Chung, T. D. *Phys. Chem, Chem. Phys.* **2012,** *14*, 448–463.)

1.5 Dissertation Overview

Various strategies for the synthesis of mesoporous nanomaterials have been investigated for their applications to LIBs and fuel cells. The synthetic routes for mesoporous nanomaterials can be categorized by three different methods: hard-template, soft-template, and colloidal superstructure methods. Precisely synthesized mesoporous nanomaterials for electrochemical electrodes have the advantages of large ECSA and short diffusion pathway, leading enhanced electrochemical performance. However, the large geometrical surface area and high ratio of edge-to-basal plane is vulnerable to side reactions during electrochemical reaction, such as excessive SEI formation in LIBs. The quantitative determination of the characteristics of mass transfer in porous structures has remained elusive because it is hard to discriminate thermodynamic reactions at the active sites and transport phenomena around the active sites. Although extensive and rigorous studies investigating the exact mechanism and features of the mass transport have been carried out, further development of the mesoporous nanomaterials as active materials is required to enable future application of these materials in

energy devices.

In chapter 2, mesoporous iron oxide superstructure by using bottom-up self-assembly strategy are synthesized for resolving excessive SEI formation in LIBs. The secondary superstructure of exhibits the characteristics of individual constituting iron NPs, as well as new collective properties derived from interactions between neighboring NPs.

In chapter 3, I develop three types of model catalysts, which have different porous structures with same surface area. The formation and utilization of three-phase boundary are investigated on the basis of electric double layer capacitance in quantitative manner. With the help of transmission line model and complex capacitance analysis, I can conclude that the mesoporous structure is essential to enlarge interphase density, whereas macroporous structure derived from the gaps between NPs needed to exhibit superior rate capability.

1.6 References

[1]   Baxter, J.; Bian, Z.; Chen, G.; Danielson, D.; Dresselhaus, M. S.; Fedorov, A. G.; Fisher, T. S.; Jones, C. W.; Maginn, E.; Kortshagen, U.et al. *Energy Environ. Sci.* **2009,** *2*, 559-588.

[2]   Hoffert, M. I.; Caldeira, K.; Jain, A. K.; Haites, E. F.; Harvey, L. D. D.; Potter, S. D.; Schlesinger, M. E.; Schneider, S. H.; Watts, R. G.; Wigley, T. M. L.et al. *Nature* **1998,** *395*, 881-884.

[3]   Steele, B. C. H.; Heinzel, A. *Nature* **2001,** *414*, 345-352.

[4]   Owens, B. B.; Osaka, T. *J. Power Sources* **1997,** *68*, 173-186.

[5]   Rolison, D. R.; Long, J. W.; Lytle, J. C.; Fischer, A. E.; Rhodes, C. P.; McEvoy, T. M.; Bourg, M. E.; Lubers, A. M. *Chem. Soc. Rev.* **2009,** *38*, 226-252.

[6]   Jeong, B.; Ocon, J. D.; Lee, J. *Angew. Chem. Int. Ed.* **2016,** *55*, 4870-4880.

[7]   Cheng, X.; Yi, B.; Han, M.; Zhang, J.; Qiao, Y.; Yu, J. *J. Power Sources* **1999,** *79*, 75-81.

[8]   Walcarius, A. *Chem. Soc. Rev.* **2013,** *42*, 4098-4140.

[9]   Evans, S. A. G.; Elliott, J. M.; Andrews, L. M.; Bartlett, P. N.; Doyle, P. J.; Denuault, G. *Anal. Chem.* **2002,** *74*, 1322-1326.

[10]   Ghanem, M. A.; Marken, F. *Electrochem. Commun.* **2005,** *7*, 1333-1339.

[11]   Szamocki, R.; Reculusa, S.; Ravaine, S.; Bartlett, P. N.; Kuhn, A.; Hempelmann, R. *Angew. Chem. Int. Ed.* **2006,** *45*, 1317-1321.

[12]   Walcarius, A.; Etienne, M.; Bessière, J. *Chem. Mater.* **2002,** *14*, 2757-2766.

[13]   Dutta, S.; Bhaumik, A.; Wu, K. C. W. *Energy Environ. Sci.* **2014,** *7*, 3574-3592.

[14]   Largeot, C.; Portet, C.; Chmiola, J.; Taberna, P.-L.; Gogotsi, Y.; Simon, P. *J. Am. Chem. Soc.* **2008,** *130*, 2730-2731.

[15]   Liu, N.; Lu, Z.; Zhao, J.; McDowell, M. T.; Lee, H.-W.; Zhao, W.; Cui, Y. *Nat. Nanotechnol.* **2014,** *9*, 187-192.

[16]   Rolison, D. R. *Science* **2003,** *299*, 1698-1701.

[17]   Merlet, C.; Rotenberg, B.; Madden, P. A.; Taberna, P.-L.; Simon, P.; Gogotsi, Y.; Salanne, M. *Nat. Mater.* **2012,** *11*, 306-310.

[18]   Kondrat, S.; Wu, P.; Qiao, R.; Kornyshev, A. A. *Nat. Mater.* **2014,** *13*, 387-393.

[19]   Chmiola, J.; Yushin, G.; Gogotsi, Y.; Portet, C.; Simon, P.;

Taberna, P. L. *Science* **2006,** *313*, 1760-1763.

[20]   Raymundo-Piñero, E.; Kierzek, K.; Machnikowski, J.; Béguin, F. *Carbon* **2006,** *44*, 2498-2507.

[21]   Griffin, J. M.; Forse, A. C.; Tsai, W.-Y.; Taberna, P.-L.; Simon, P.; Grey, C. P. *Nat. Mater.* **2015,** *14*, 812-819.

[22]   Forse, A. C.; Griffin, J. M.; Merlet, C.; Bayley, P. M.; Wang, H.; Simon, P.; Grey, C. P. *J. Am. Chem. Soc.* **2015,** *137*, 7231-7242.

[23]   Levi, M. D.; Salitra, G.; Levy, N.; Aurbach, D.; Maier, J. *Nat. Mater.* **2009,** *8*, 872-875.

[24]   Costentin, C.; Di Giovanni, C.; Giraud, M.; Saveant, J.-M.; Tard, C. *Nat. Mater.* **2017,** *16*, 1016-1021.

[25]   Roberts, A. D.; Li, X.; Zhang, H. *Chem. Soc. Rev.* **2014,** *43*, 4341-4356.

[26]   Gu, D.; Schuth, F. *Chem. Soc. Rev.* **2014,** *43*, 313-344.

[27]   Soler-Illia, G. J. A. A.; Azzaroni, O. *Chem. Soc. Rev.* **2011,** *40*, 1107-1150.

[28]   Soler-Illia, G. J. d. A. A.; Sanchez, C.; Lebeau, B.; Patarin, J. *Chem. Rev.* **2002,** *102*, 4093-4138.

[29]   Schrettl, S.; Schulte, B.; Frauenrath, H. *Nanoscale* **2016,** *8*,

18828-18848.

[30]   Yang, X.-Y.; Chen, L.-H.; Li, Y.; Rooke, J. C.; Sanchez, C.; Su,
         B.-L. *Chem. Soc. Rev.* **2017,** *46*, 481-558.

[31]   Petkovich, N. D.; Stein, A. *Chem. Soc. Rev.* **2013,** *42*, 3721-
         3739.

[32]   Falcaro, P.; Malfatti, L.; Kidchob, T.; Giannini, G.; Falqui, A.;
         Casula, M. F.; Amenitsch, H.; Marmiroli, B.; Grenci, G.;
         Innocenzi, P. *Chem. Mater.* **2009,** *21*, 2055-2061.

[33]   Zhang, X.; Lu, W.; Dai, J.; Bourgeois, L.; Hao, N.; Wang, H.;
         Zhao, D.; Webley, P. A. *Angew. Chem. Int. Ed.* **2010,** *49*,
         10101-10105.

[34]   Zhang, Y.; Hu, L.; Han, J.; Jiang, Z.; Zhou, Y. *Micropor.*
         Mesopor. Mater. **2010,** *130*, 327-332.

[35]   Sun, Z.; Deng, Y.; Wei, J.; Gu, D.; Tu, B.; Zhao, D. *Chem.*
         Mater. **2011,** *23*, 2176-2184.

[36]   Kresge, C. T.; Leonowicz, M. E.; Roth, W. J.; Vartuli, J. C.;
         Beck, J. S. *Nature* **1992,** *359*, 710-712.

[37]   Chen, Y.; Chen, H.; Zeng, D.; Tian, Y.; Chen, F.; Feng, J.; Shi,
         J. *ACS Nano* **2010,** *4*, 6001-6013.

[38]   Drisko, G. L.; Zelcer, A.; Luca, V.; Caruso, R. A.; Soler-Illia,

G. J. d. A. A. *Chem. Mater.* **2010,** *22*, 4379-4385.

[39] Gao, H.-L.; Xu, L.; Long, F.; Pan, Z.; Du, Y.-X.; Lu, Y.; Ge, J.; Yu, S.-H. *Angew. Chem. Int. Ed.* **2014,** *53*, 4561-4566.

[40] Simon, P. F. W.; Ulrich, R.; Spiess, H. W.; Wiesner, U. *Chem. Mater.* **2001,** *13*, 3464-3486.

[41] Zhao, D.; Feng, J.; Huo, Q.; Melosh, N.; Fredrickson, G. H.; Chmelka, B. F.; Stucky, G. D. *Science* **1998,** *279*, 548-552.

[42] Che, S.; Garcia-Bennett, A. E.; Yokoi, T.; Sakamoto, K.; Kunieda, H.; Terasaki, O.; Tatsumi, T. *Nat. Mater.* **2003,** *2*, 801-805.

[43] Wan, Y.; Zhao. *Chem. Rev.* **2007,** *107*, 2821-2860.

[44] Huo, Q.; Margolese, D. I.; Ciesla, U.; Demuth, D. G.; Feng, P.; Gier, T. E.; Sieger, P.; Firouzi, A.; Chmelka, B. F. *Chem. Mater.* **1994,** *6*, 1176-1191.

[45] Templin, M.; Franck, A.; Du Chesne, A.; Leist, H.; Zhang, Y.; Ulrich, R.; Schädler, V.; Wiesner, U. *Science* **1997,** *278*, 1795-1798.

[46] Orilall, M. C.; Wiesner, U. *Chem. Soc. Rev.* **2011,** *40*, 520-535.

[47] Fan, J.; Boettcher, S. W.; Tsung, C.-K.; Shi, Q.; Schierhorn, M.; Stucky, G. D. *Chem. Mater.* **2008,** *20*, 909-921.

[48]   Attard, G. S.; Glyde, J. C.; Goltner, C. G. *Nature* **1995,** *378,* 366-368.

[49]   Meng, Y.; Gu, D.; Zhang, F.; Shi, Y.; Cheng, L.; Feng, D.; Wu, Z.; Chen, Z.; Wan, Y.; Stein, A.et al. *Chem. Mater.* **2006,** *18,* 4447-4464.

[50]   Monnier, A.; Schüth, F.; Huo, Q.; Kumar, D.; Margolese, D.; Maxwell, R. S.; Stucky, G. D.; Krishnamurty, M.; Petroff, P.; Firouzi, A.et al. *Science* **1993,** *261,* 1299-1303.

[51]   Attard, G. S.; Bartlett, P. N.; Coleman, N. R. B.; Elliott, J. M.; Owen, J. R.; Wang, J. H. *Science* **1997,** *278,* 838-840.

[52]   Cagnol, F.; Grosso, D.; Soler-Illia, G. J. d. A. A.; Crepaldi, E. L.; Babonneau, F.; Amenitsch, H.; Sanchez, C. *J. Mater. Chem.* **2003,** *13,* 61-66.

[53]   Lu, Z.; Yin, Y. *Chem. Soc. Rev.* **2012,** *41,* 6874-6887.

[54]   Nie, S.; Emory, S. R. *Science* **1997,** *275,* 1102-1106.

[55]   Penn, R. L.; Banfield, J. F. *Science* **1998,** *281,* 969-971.

[56]   Narayanaswamy, A.; Xu, H.; Pradhan, N.; Kim, M.; Peng, X. *J. Am. Chem. Soc.* **2006,** *128,* 10310-10319.

[57]   Narayanaswamy, A.; Xu, H.; Pradhan, N.; Peng, X. *Angew. Chem. Int. Ed.* **2006,** *45,* 5361-5364.

[58]   Corma, A.; Atienzar, P.; Garcia, H.; Chane-Ching, J.-Y. *Nat. Mater.* **2004,** *3*, 394-397.

[59]   Zhuang, J.; Wu, H.; Yang, Y.; Cao, Y. C. *Angew. Chem. Int. Ed.* **2008,** *47*, 2208-2212.

[60]   Bai, F.; Wang, D.; Huo, Z.; Chen, W.; Liu, L.; Liang, X.; Chen, C.; Wang, X.; Peng, Q.; Li, Y. *Angew. Chem. Int. Ed.* **2007,** *46*, 6650-6653.

[61]   Chen, C.; Nan, C.; Wang, D.; Su, Q.; Duan, H.; Liu, X.; Zhang, L.; Chu, D.; Song, W.; Peng, Q.et al. *Angew. Chem. Int. Ed.* **2011,** *50*, 3725-3729.

[62]   WHITTINGHAM, M. S. *Science* **1976,** *192*, 1126-1127.

[63]   Tarascon, J. M.; Armand, M. *Nature* **2001,** *414*, 359-367.

[64]   Thackeray, M. M.; Wolverton, C.; Isaacs, E. D. *Energy Environ. Sci.* **2012,** *5*, 7854-7863.

[65]   Goodenough, J. B.; Park, K.-S. *J. Am. Chem. Soc.* **2013,** *135*, 1167-1176.

[66]   Poizot, P.; Laruelle, S.; Grugeon, S.; Dupont, L.; Tarascon, J. M. *Nature* **2000,** *407*, 496-499.

[67]   Yu, S.-H.; Lee, S. H.; Lee, D. J.; Sung, Y.-E.; Hyeon, T. *Small* **2016,** *12*, 2146-2172.

[68]   Eftekhari, A. *Micropor. Mesopor. Mater.* **2017,** *243*, 355-369.

[69]   Mai, L.; Tian, X.; Xu, X.; Chang, L.; Xu, L. *Chem. Rev.* **2014,** *114*, 11828-11862.

[70]   Ren, Y.; Armstrong, A. R.; Jiao, F.; Bruce, P. G. *J. Am. Chem. Soc.* **2010,** *132*, 996-1004.

[71]   Kim, E.; Son, D.; Kim, T.-G.; Cho, J.; Park, B.; Ryu, K.-S.; Chang, S.-H. *Angew. Chem. Int. Ed.* **2004,** *43*, 5987-5990.

[72]   Park, G. O.; Yoon, J.; Park, E.; Park, S. B.; Kim, H.; Kim, K. H.; Jin, X.; Shin, T. J.; Kim, H.; Yoon, W.-S.et al. *ACS Nano* **2015,** *9*, 5470-5477.

[73]   Goodenough, J. B.; Kim, Y. *Chem. Mater.* **2010,** *22*, 587-603.

[74]   An, S. J.; Li, J.; Daniel, C.; Mohanty, D.; Nagpure, S.; Wood, D. L. *Carbon* **2016,** *105*, 52-76.

[75]   Patil, A.; Patil, V.; Wook Shin, D.; Choi, J.-W.; Paik, D.-S.; Yoon, S.-J. *Mater. Res. Bull.* **2008,** *43*, 1913-1942.

[76]   Li, M.; Wu, Y.; Zhao, F.; Wei, Y.; Wang, J.; Jiang, K.; Fan, S. *Carbon* **2014,** *69*, 444-451.

[77]   Shi, S.; Lu, P.; Liu, Z.; Qi, Y.; Hector, L. G.; Li, H.; Harris, S. J. *J. Am. Chem. Soc.* **2012,** *134*, 15476-15487.

[78]   Zhang, J.; Wang, R.; Yang, X.; Lu, W.; Wu, X.; Wang, X.; Li,

H.; Chen, L. *Nano Lett.* **2012,** *12*, 2153-2157.

[79] Wu, H.; Chan, G.; Choi, J. W.; Ryu, I.; Yao, Y.; McDowell, M. T.; Lee, S. W.; Jackson, A.; Yang, Y.; Hu, L.et al. *Nat. Nanotechnol.* **2012,** *7*, 310-315.

[80] Gasteiger, H. A.; Marković, N. M. *Science* **2009,** *324*, 48-49.

[81] Cheng, F.; Chen, J. *Chem. Soc. Rev.* **2012,** *41*, 2172-2192.

[82] Ge, X.; Sumboja, A.; Wuu, D.; An, T.; Li, B.; Goh, F. W. T.; Hor, T. S. A.; Zong, Y.; Liu, Z. *ACS Catal.* **2015,** *5*, 4643-4667.

[83] Geniès, L.; Faure, R.; Durand, R. *Electrochim. Acta* **1998,** *44*, 1317-1327.

[84] Hu, P.; Song, Y.; Chen, L.; Chen, S. *Nanoscale* **2015,** *7*, 9627-9636.

[85] GreeleyJ; Stephens, I. E. L.; Bondarenko, A. S.; Johansson, T. P.; Hansen, H. A.; Jaramillo, T. F.; RossmeislJ; ChorkendorffI; Nørskov, J. K. *Nat. Chem.* **2009,** *1*, 552-556.

[86] Jasinski, R. *Nature* **1964,** *201*, 1212-1213.

[87] Zhu, C.; Li, H.; Fu, S.; Du, D.; Lin, Y. *Chem. Soc. Rev.* **2016,** *45*, 517-531.

[88] Koslowski, U. I.; Abs-Wurmbach, I.; Fiechter, S.; Bogdanoff, P. *J. Phys. Chem. C* **2008,** *112*, 15356-15366.

[89] Zitolo, A.; Goellner, V.; Armel, V.; Sougrati, M.-T.; Mineva, T.; Stievano, L.; Fonda, E.; Jaouen, F. *Nat. Mater.* **2015,** *14*, 937-942.

[90] Kramm, U. I.; Herranz, J.; Larouche, N.; Arruda, T. M.; Lefevre, M.; Jaouen, F.; Bogdanoff, P.; Fiechter, S.; Abs-Wurmbach, I.; Mukerjee, S.; Dodelet J.-P. *Phys. Chem. Chem. Phys.,* **2012,** *14*, 11673-11688.

[91] Carver, C. T.; Matson, B. D.; Mayer, J. M. *J. Am. Chem. Soc.* **2012,** *134*, 5444-5447.

[92] Kattel, S.; Wang, G. *J. Mater. Chem. A* **2013,** *1*, 10790-10797.

[93] Ramaswamy, N.; Tylus, U.; Jia, Q.; Mukerjee, S. *J. Am. Chem. Soc.* **2013,** *135*, 15443-15449.

[94] Liu, J.; Li, E.; Ruan, M.; Song, P.; Xu, W. *Catalysts* **2015,** *5*, 1167.

[95] Costentin, C.; Savéant, J.-M. *Proc. Natl. Acad. Sci.* **2016,** *113*, 11756-11758.

[96] Joo, S. H.; Choi, S. J.; Oh, I.; Kwak, J.; Liu, Z.; Terasaki, O.; Ryoo, R. *Nature* **2001,** *412*, 169-172.

[97] Wang, G.; Sun, Y.; Li, D.; Liang, H.-W.; Dong, R.; Feng, X.; Müllen, K. *Angew. Chem.* **2015,** *127*, 15406-15411.

[98] Bae, J. H.; Han, J.-H.; Chung, T. D. *Phys. Chem, Chem. Phys.* **2012,** *14*, 448-463.

[99] Levitz, P. *J. Phys. Chem.* **1993,** *97*, 3813-3818.

[100] White, R. J.; White, H. S. *Anal. Chem.* **2005,** *77*, 214 A-220 A.

[101] Tang, J.; Liu, J.; Li, C.; Li, Y.; Tade, M. O.; Dai, S.; Yamauchi, Y. *Angew. Chem. Int. Ed.* **2015,** *54*, 588-593.

[102] Bonakdarpour, A.; Lefevre, M.; Yang, R.; Jaouen, F.; Dahn, T.; Dodelet, J.-P.; Dahn, J. R. *Electrochem. Solid-State Lett.* **2008,** *11*, B105-B108.

[103] Amatore, C.; Savéant, J. M.; Tessier, D. *J. Electroanal. Chem.* **1983,** *147*, 39-51.

[104] Bertoncello, P.; Edgeworth, J. P.; Macpherson, J. V.; Unwin, P. R. *J. Am. Chem. Soc.* **2007,** *129*, 10982-10983.

[105] Dumitrescu, I.; Dudin, P. V.; Edgeworth, J. P.; Macpherson, J. V.; Unwin, P. R. *J. Phys. Chem. C* **2010,** *114*, 2633-2639.

Chapter 2. Magnetite Nanoparticle Clusters as Highly Stable Anodes for Lithium-Ion Batteries via Controlled SEI formation

2.1 Introduction

In the last two decades, many transition-metal oxide nanostructures based on conversion reactions have been extensively supposed as potential LIB anodes because they have higher theoretical specific capacities (~1000 mAh g^{-1}) than the currently commercially used graphite (372 mAh g^{-1}) and they show significantly improved reversibility.[1-3] Furthermore, nano-sized materials are known to provide short diffusion pathways for lithium ions, resulting in high rate capabilities.[4] Despite these advantages, these nano-sized materials face two critical challenges for practical commercial LIBs applications. Firstly, they generally exhibit poor capacity retention, which is attributed to their huge volume expansion during lithiation/delithiation processes. Although the mechanical stress originated from volume expansion and contraction during cycling can be reduced with small-

sized nanoparticles,[5] such particles are likely to be pulverized after long cycles, ultimately leading to rapid capacity fading. Secondly, the solid-electrolyte-interphase (SEI) layer formed by electrolyte decomposition on the surface of anode materials can deteriorate battery performance tremendously. Repeated expansion and contraction upon cycling can cause fracture on the surfaces, which can provide new active surfaces for SEI growth. The continuous SEI formation associated with additional exposure of the active material upon each cycle bring about consistent consumption of electrolytes and lithium ions, and the resulting SEI layer retards the diffusion of lithium ions. As a result, the design of a stable SEI at the interface between the electrolyte and active material is critically important to achieve a more stable and enhanced battery performance.[6] The stable SEI involves elasticity, flexibility and uniform morphology to relax non-uniform electrochemical reactions, which can supply good passivation to the anode materials.[7] However, nanoparticles (NPs) have a huge surface area over which electrolytes can decompose, and a thick SEI layer can be generated easily and continuously with each charge/discharge cycle. In order to overcome these limitations, a wide variety of nanostructures such as metal oxide/carbon composites,[8-10]

mesoporous structures,[11-15] hollow structures,[16-20] and inactive/active composites[21,22] have been investigated. Recently, various coating methods such as conformal carbon coating,[23] tubular carbon coating,[24,25] and silica shell coating[6] have been developed in nanostructured silicon-based anode materials, resulting in the improved mechanical strength, higher conductivity, and most importantly stable SEI formation. Herein, we report the successful synthesis of mesoporous iron oxide nanoparticle clusters (MIONCs) with carbon coatings through bottom-up self-assembly approach. Owing to the 3D-ordered and mesoporous structures, the MIONCs showed higher cyclic stability than random aggregates of iron oxide nanoparticles (RAIONs), and commercialized bare iron oxides (CBIOs) by confining stable SEI layer on the outer surface. Iron oxide NPs were selected as the representative component NPs because of their well-characterized properties and facile production.[26] Among various synthetic strategies for the preparation of 3D mesoporous metal oxides,[27-29] I used bottom-up self-assembly strategy because the secondary structure exhibits not only the characteristics of individual constituting NPs, but also new collective properties derived from interactions between neighboring NPs.

2.2 Experimental Section

2.2.1. Synthesis of Fe₃O₄ nanoparticles

36 g of iron-oleate complex (40 mmol), 10.4 g of oleic acid (40 mmol, 90%, Aldrich), and 200 g of dioctyl ether (95%, Aldrich) were added in 1 L reactor and mixed at room temperature. The reaction mixture was degassed at 90 °C under vacuum for 2 h. The mixture was heated to 287 °C with a constant heating rate of 3.3 °C/min, and then held at that temperature for 30 min under Ar atmosphere. The resulting solution was then slowly cooled to approximately 150 °C, and the solution was exposure to air to increase the crystallinity of the nanoparticles for 2 hr. Subsequently, 700 ml of acetone was added to the solution to precipitate the nanoparticles and the nanoparticles were separated by discarding supernatant. In this procedure, most of dioctyl ether was separated but not oleic acid (Non-washed state). To wash free oleic acid, the nanoparticles were dispersed in hydrophobic solvent (such as hexane or chloroform) and acetone with the ratio of 1:3 (washing process). Finally the iron oxide nanoparticles are redispersed in chloroform with concentration of 75 mg/mL.

2.2.2. Synthesis of Random Aggregates of Iron Oxide Nanoparticles (RAIONs)

The typical synthetic procedure used to generate RAIONs is as follows: The non-washed iron oxide nanoparticles were dried in vacuum at 70 °C for 3 h. The resulting powders were then calcinated under Ar from room temperature to 500 °C at a heating rate of 1.66 °C min^{-1} and held at this temperature for 5 hr to synthesize the RAIONs.

2.2.3. Synthesis of Colloidal Nanoparticle Clusters (CNCs)

In typical synthetic procedure, Dodecyltrimethylammonium bromide (DTAB, 0.1 g) was dissolved in 5ml of pure water. A 0.5 mL chloroform solution consisted of nanoparticles (75 mg/mL) was added to the solution with stirring vigorously. After 30 min, the chloroform was removed by Ar flow for 2 hr.

This nanoparticle-micelle solution was injected to flask composed of Polyvinylpyrrolidone solution (MW 55000, 2.75 g) which was dissolved in 25 ml of ethylene glycol with stirring. The mixture heated up 80 °C with Ar flow at a heating rate of 10 °C min^{-1} and held up 6 hr. The solution was separated by centrifuge (8000 rpm, 20 min). The supernatant part of solution was discarded and rest of solution was

redispersed in ethanol. We repeated this washing process 3 times.

2.2.4. Synthesis of Mesoporous Iron Oxide Nanoparticle Clusters (MIONCs)

To prepare MIONCs, the CNCs in ethanol was dried in vacuum oven at 70 °C for 3 h to remove ethanol solvent. The resulting nanoparticles were then calcined under Ar from room temperature to 500 °C at a heating rate of 1.66 °C min^{-1} and held at this temperature for 5 hr.

2.2.5. Selective Chemical Etching of Solid-Electrolyte-Interphase (SEI) layer

For selective removal of SEI, we used chemical etching process which had been previous reported.[3] The RAIONs and MIONCs electrodes after cycling were carefully taken out of argon-filled glove box and were soaked immediately in acetonitrile 24 hr for washing the residue of electrolytes. Moreover, the two samples were dipped in water for 48 hr to remove residual Li_2O. For characterizing TEM and SEM, etched samples were detached using sonicator. ED patterns (Insets of Figures 7d and 7h) confirms that Li_2O is absent after the selective etching.

2.2.6. Electrochemical Test

Working electrodes were fabricated by mixing the samples, Super P (as a conductive agent) and PVDF (as a binder) in N-methyl-2-pyrrolidone solvent at a weight ratio of 70:15:15. The diameter of Cu foil was 11 mm and loading level was 2.1 mg cm^{-2}. The prepared mixture was pressed into a film, followed by drying under vacuum at 120 °C overnight. A two-electrode 2016 type coin cell was used to assess the electrochemical performance of the samples. Lithium metal electrode was used as a counter and reference electrode, the organic electrolyte was 1.0 M LiPF$_6$ dissolved in a mixture of ethylene carbonate and diethyl carbonate with a volume ratio of 1:1. Electrochemical test cells galvanostatically charged and discharged in the voltage range of 3.0 to 0.01 V (vs. Li/Li$^+$). The cyclic voltammetry experiment was conducted at a scan rate of 0.1 mV s^{-1}. Electrochemical measurements were performed using a WBCS3000 cycler (WonA tech, Korea) at room temperature. In the cycle performance test, the current density was fixed at 100 mA g^{-1}. In the rate performance test, the current density was changed according to this sequence of values: 0.1, 0.2, 0.4, 0.8 and 1.6 A g^{-1} for every 10 cycles.

2.2.7. Characterization

All TEM images were obtained using a JEOL EM-2010 microscope at an acceleration voltage of 200 kV. The samples for TEM studies were prepared by drying a drop of the suspension of the nanoparticles on a piece of carbon-coated copper grid under ambient conditions. All SEM images were obtained using a Carl Zeiss SUPRA 55VP Field-Emission Scanning Electron Microscope at voltage of 15 kV. The samples for SEM images were prepared by using carbon-type. The X-ray diffraction pattern was taken by a Rigaku Dmax 2500 diffractometer system. The small angle X-ray scattering was measured by a D8 DISCOVER with GADDS (Brucker). The surface area and pore size was measured using micromeritics surface area measurement analyzer (ASAP 2000). Before actual measurements, the samples were degassed at 120 °C for 5 hr under high vacuum. Elemental analysis was performed by Elemental Analyser using CHNS-932 (LECO Corp). The hydrodynamic diameters of nanoparticles were measured with a particle size analyzer (ELS-Z2, Otsuka). The microtoming of nanoparticles was taken by MTX Ultramictome (RMC, USA). The Raman spectra were recorded on Jobin Yvon In-situ Raman spectroscopy (LabRam HR).

2.3 Result and Discussion

2.3.1. Synthesis of MIONCs and RAIONs

The overall synthetic procedure of the MIONCs and RAIONs is shown in Figure 1a. Fe_3O_4 NPs (11–12 nm) were prepared by thermal decomposition of iron–oleate complex using the previously reported method.[26] For the synthesis of MIONCs, the Fe_3O_4 NPs were self-assembled into colloidal nanoparticle clusters (CNCs) based on the previously reported method.[31] Fe_3O_4 NPs in chloroform were emulsified into an aqueous solution containing DTAB as surfactants for use in an oil-in-water emulsion system. Subsequently, the solution was heated to evaporate the oil phase in the emulsion droplet, leading to the synthesis of densely packed CNCs. At least two times of washing process were required because free oleic acid in Fe_3O_4 NPs solution can act as a co-surfactant in oil-in-water emulsion system.[44]

Further coating of polyvinylpyrrolidone (PVP) polymers stabilized the CNCs through repulsive steric interactions, and directed the CNCs into a more ordered structure.
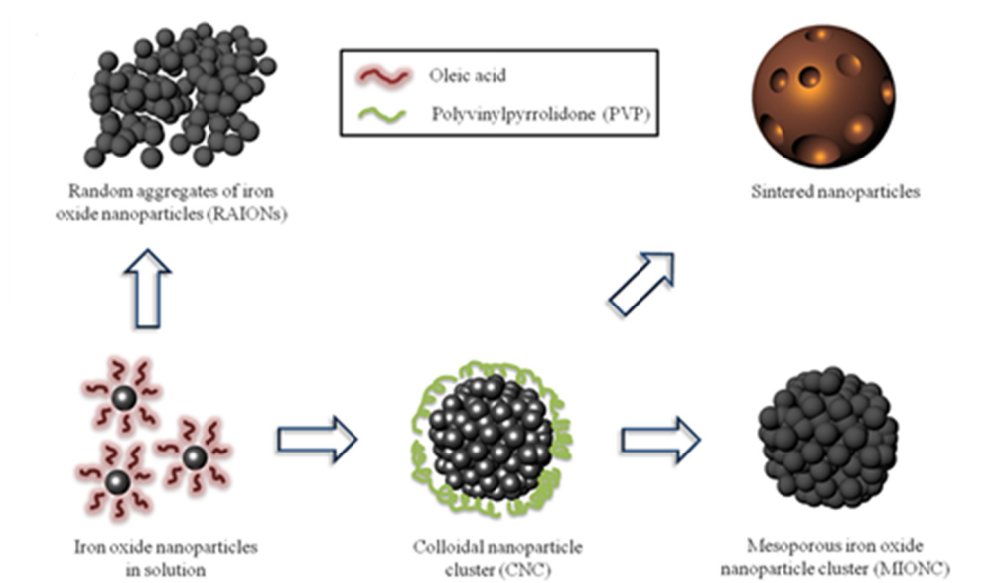
Figure 2.1. Schematic illustration of the preparation of MIONCs and RAIONs. (b) TEM image of MIONCs

2.3.2. Characterization of MIONCs and RAIONs

TEM image (Figure 2.2.b) and dynamic light scattering (DLS) data (Figure 2.2.c) exhibited that the average size of the CNCs was 174 nm with a relative standard deviation of 26%. The CNCs were then dried in vacuum and calcined in Ar at 500 °C for 5 h to yield mesoporous iron oxide nanoparticle clusters (MIONCs) with carbon coating. Figure 2.3.a clearly exhibits that the morphology of the MIONCs maintained intact even after the heat treatment at 500 °C. High-resolution TEM (HRTEM) image was obtained after a microtoming process to verify the internal structure of the MIONCs. Figure 2.3.b exhibits uniform pores between neighboring Fe_3O_4 NPs, and such ordered assembly structure were observed throughout the MIONCs.

To synthesize comparison group, Fe_3O_4 NPs in chloroform were dried in a vacuum oven and then heated directly in Ar without any modification, leading to the formation of random aggregates of iron oxide nanoparticles (RAIONs). To make sufficient carbon coatings in the RAIONs, the Fe_3O_4 NPs were prepared without washing process. A TEM image of the RAIONs (Figure 2.3.c) showed that no sintering appeared between the constituting Fe_3O_4 NPs. HRTEM image of these RAIONs (Figure 2.3.d) exhibited that the individual Fe_3O_4 NPs were

distinctly observable in a carbon matrix with high crystallinity. Figure 2.4.a shows a low-magnification TEM image of microtomed sections of the MIONCs. Interestingly, black sintered parts were sometimes observed, as shown by the red circle in Figure 2a. For the analysis of the structure and composition of the sintered particles, HRTEM images and selected-area electron diffraction (SAED) patterns were obtained. The HRTEM image exhibited that the black sintered particles had a different phase, which was different from the neighboring Fe_3O_4 NPs (see the regions in the red and blue squares in Figure 2.4.b). From the SAED patterns, it was confirmed that the phase in the red square corresponds to metallic Fe (Figure 2.4.d), and that in the blue square to Fe_3O_4 (Figure 2.4.c). In synthesis procedure, PVP polymers were gradually degraded with concomitant evolution of H_2 gas to bring about a reductive environment. Because the degradation temperature of PVP starts at 380 °C and peaks at 435 °C,[32] metallic Fe NPs might be expected to transform more easily from Fe_3O_4 NPs in such an reductive environment. Advantageous roles of these metallic iron species in LIBs are discussed below.

Figure 2.5a shows the X-ray diffraction (XRD) pattern of the MIONCs, and shows Fe and Fe_3O_4 phases. The most intense diffraction

peaks at 44.9° and 65.2° demonstrate the formation of metallic Fe. The major diffraction peaks except these two peaks can be matched to the inverse spinel phase of Fe_3O_4. The crystal size of metallic Fe, calculated using the Scherrer equation, was evaluated to be ~ 80 nm, which is roughly eight times larger than that of the component Fe_3O_4 nanoparticles. The ratio of Fe_3O_4 to Fe was determined by Rietveld refinement to be 94:6 wt% (Figure 2.5.c). In comparison, the XRD pattern of the RAIONs revealed the presence of highly crystalline Fe_3O_4. Small-angle X-ray scattering (SAXS) measurements on the MIONCs and RAIONs were conducted to verify the long-range ordering (Figure 2.5.b). The main peak was exhibited at 1.7° for the MIONCs, which corresponds to a d-spacing of approximately 5.2 nm (from $\lambda = 2d \sin \theta$), demonstrating a well-ordered assembled structure after the calcination. However, in the case of the RAIONs, no clearly distinguishable peak was obtained, indicating random assembly of nanoparticles within the aggregates.

For further confirmation of the surface area and porous structure, nitrogen adsorption–desorption isotherms were obtained. The MIONCs exhibited a type-IV isotherm (Figure 2.6.a), which was ascribed to a mesoporous structure with uniform pores.[33] The Brunauer–Emmett–

9 8

Teller (BET) surface area of the MIONCs was calculated to be 55.4 m^2 g^{-1}. A uniform pore distribution with an average size of 3.5 nm was determined from analysis of the desorption curve (Figure 2.6.c). Furthermore, a broad peak at around 40 nm was observed for the MIONCs, corresponding to the mesopores among the clusters. In comparison, we obtained a type-IV isotherm for the RAIONs with an H3-type hysteresis loop attributed to an interconnected mesoporous system (Figure 2.6.b).[34] The BET surface area was measured to be 144.6 m^2 g^{-1}. The pore-size distribution for the RAIONs is shown in the inset of Figure 2.6.b, and indicates the formation of randomly distributed pores. There were no additional pores with diameters of more than 25 nm (Figure 2.6.d). Elemental analysis showed that the MIONC and RAION samples contained 7.7 and 24.0 wt% carbon, respectively. In order to examine the characteristics of the carbon layer within the samples, we performed Raman spectroscopy on the two samples (Figure 2.5.d). In the case of the MIONCs, the signal peaks exhibited a D band at 1315 cm^{-1} and a weaker G band at 1580 cm^{-1}, with an I_D/I_G ratio of 1.15. On the contrary, the RAIONs had a D band at 1322 cm^{-1} and G band at 1578 cm^{-1} with similar intensities (I_D/I_G ratio of 0.99). As reported previously,[35] the D band is ascribed to sp^3

9 9

carbon and defects such as topological defects, dangling bonds, and vacancies, whereas the G band is attributed to ordered sp^2 carbon. Therefore, the I_D/I_G ratio represents the degree of disorder in the carbon materials on the surfaces of the MIONCs and RAIONs, which can be regarded as disordered nanocrystalline graphite.[36]
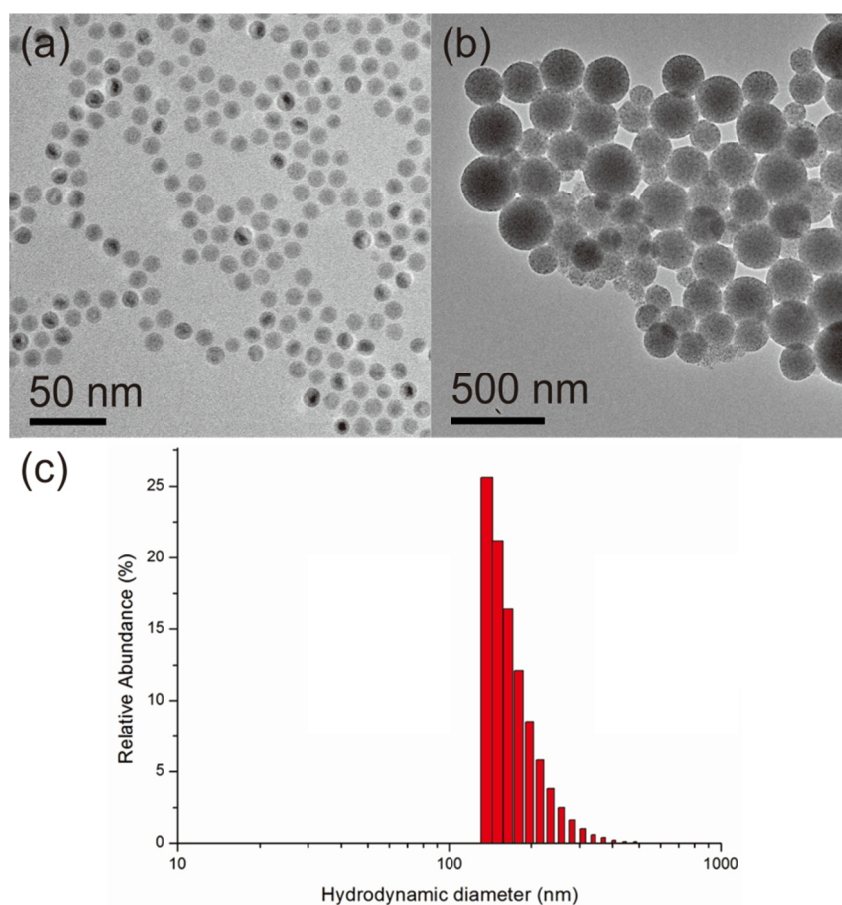
Figure 2.2. TEM images of (a) Fe_3O_4 NPs prepared via thermal decomposition of Fe-oleate complexes and (b) synthesized CNCs composed of Fe_3O_4 NPs dispersed in water. (c) Dynamic light scattering data for as-synthesized CNCs dispersed in water. Hydrodynamic diameter was measured as 174 ± 44.8 nm.

1 0 1
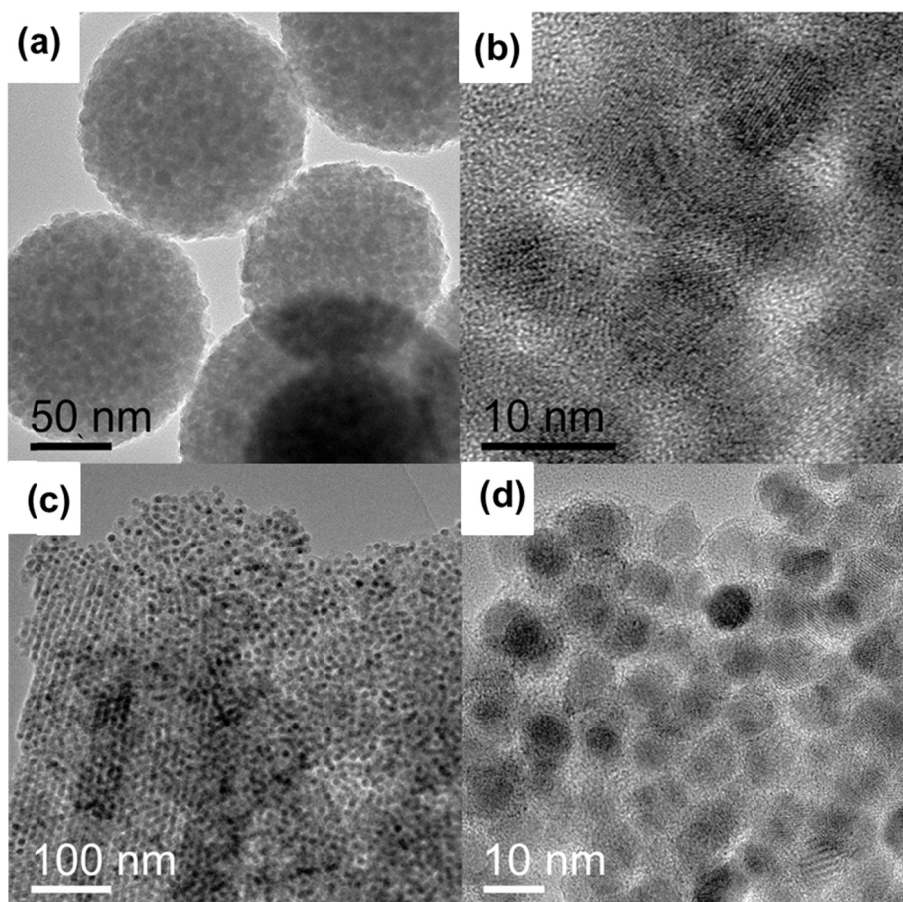
Figure 2.3. (a) TEM image of MIONCs. (b) HRTEM image obtained from cross-sectioned MIONCs by microtoming. (c) TEM image of RAIONs. No sintering was occurred between each component Fe_3O_4 NPs. (d) In high resolution TEM (HR-TEM) image of RAIONs.
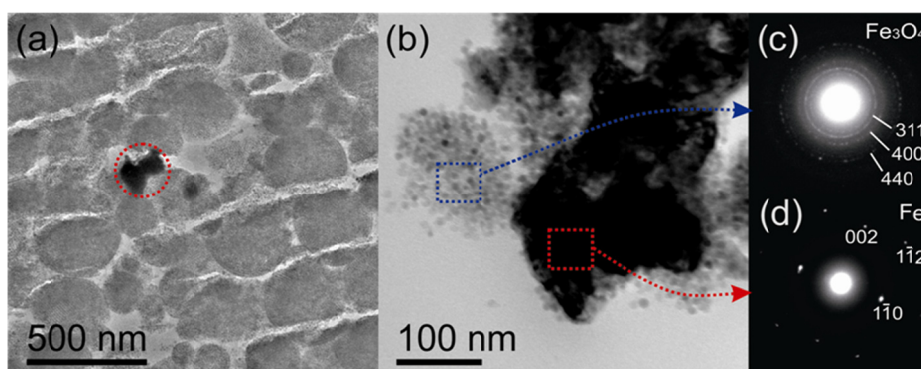
Figure 2.4. (a) Low-magnification TEM image and (b) HRTEM image of MIONCs obtained by ultra-thin microtoming method (sectioned at 100 nm thickness); (c,d) SAED patterns corresponding to the regions of the red and blue squares indicated in the TEM image of (b), respectively.
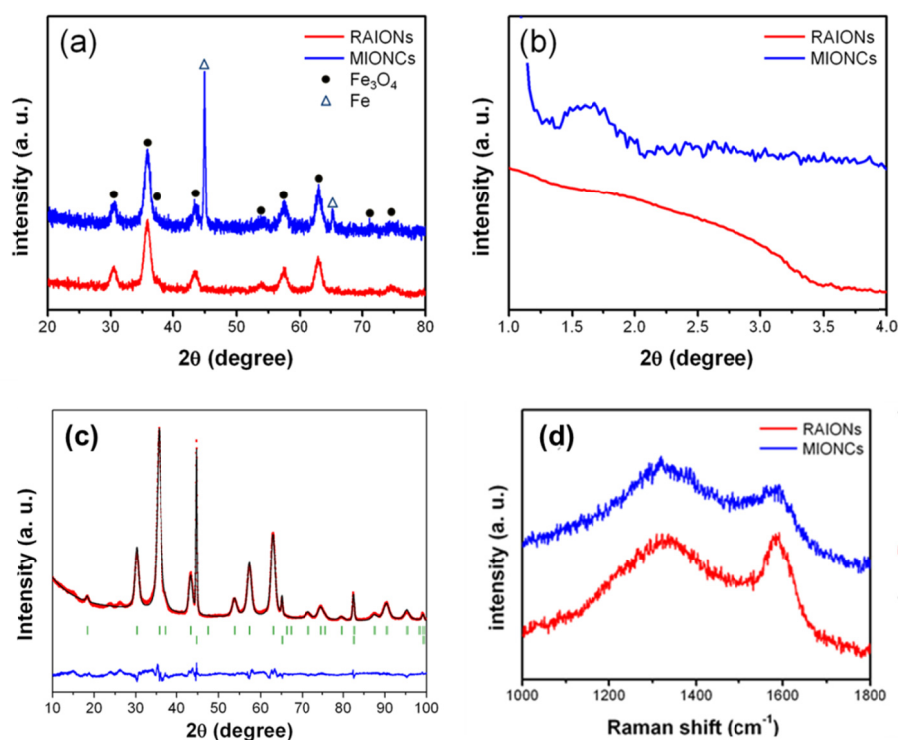
Figure 2.5. (a) XRD patterns of MIONCs and RAIONs. (b) SAXS patterns of MIONCs and RAIONs. (c) Rietveld refinement of the MIONCs sample. Bragg positions (green) for Fe_3O_4 (above) and Fe (below) are indicated. Observed data (red squares) at room temperature, fitting curve (black line) and difference curve (blue line) are also reported. A ratio of Fe_3O_4 to Fe was determined to be 94:6 wt%. (d) (c) Raman spectra of MIONCs and RAIONs.

1 0 4
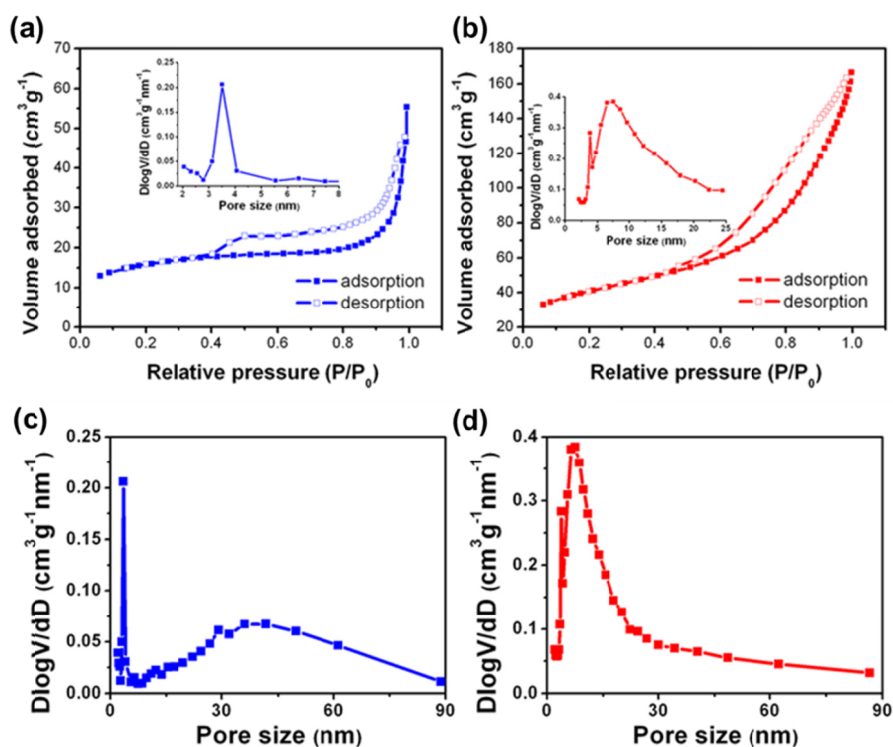
Figure 2.6. N_2 adsorption–desorption isotherms of MIONCs (a) and RAIONs (b). (c) Interstitial pore size distribution of MIONCs. Most uniform pores inside the clusters are positioned at 3.5 nm, but broad pores were also detected in the regions of 20~60nm, peaked at 40 nm. (d) Pore size distribution of RAIONs exhibited that there is no pore distribution more than 25 nm and randomly positioned in the regions of 5~15 nm.

2.3.3. Electrochemical Test via Coin-type Cells

The application of MIONCs and RAIONs as LIB anode materials was characterized by an electrochemical test using coin-type cells. Figures 2.7.a and 2.7.b show the cyclic voltammograms of the MIONCs and RAIONs, respectively. In the cathodic process, both samples showed large peaks at 0.58 and 0.64 V, respectively, in the first cycle; this represented the conversion reaction $Fe_3O_4 + 8Li^+ + 8e^- \rightarrow 3Fe^0 + 4Li_2O$ with the formation of the SEI layer. The two samples commonly exhibited a peak below 0.5 V, which was mainly owing to the reaction of lithium with carbon. In the first anodic cycle, two peaks were visible at approximately 1.66 and 1.87 V in both samples, attributed to the oxidation of Fe^0 to Fe^{2+} and Fe^{3+}, respectively. These results are in accordance with the previous studies, especially those involving $Fe/Fe_3O_4/C$[22] and Fe_3O_4/C[37] composite anode materials. The difference between the peaks in the first cycle and in subsequent cycles can be attributed to activation processes, involving the conversion to nanosized metal particles dispersed in the Li_2O matrix or the formation of the SEI. These similar phenomena were also observed in the galvanostatic charge–discharge voltage profiles measured at a current density of 100 mA g^{-1} (Figure 2.7.c,d).

In order to test the durability of the electrodes, the MIONCs, RAIONs and CBIOs were charged and discharged galvanostatically in the range of 0.01–3.00 V (*vs*. Li$^+$/Li) at a current density of 100 mA g^{-1} (Figure 2.8.a). The reversible capacity of the MIONCs was around 867 mAh g^{-1} in the first cycle. Interestingly, the specific capacity initially decreases until ten cycles and then began to increase after ten cycles and continued until 80 cycles; this increase was ascribed to the existence of some activation process, such as electrolyte penetration to active materials.[38,39] More importantly, the MIONCs exhibited high cyclic stability during 100 cycles even though small amounts of capacity decrease at first. On the contrary, the RAIONs exhibited a high specific capacity of 970 mAh g^{-1} initially and retained about 76.6% of the initial capacity after 80 cycles. The first charge capacity of the RAIONs was higher than the theoretical specific capacities of Fe$_3$O$_4$ (926 mAh g^{-1}) and graphite (372 mAh g^{-1}). This excess specific capacity can be ascribed to the defeat-rich carbonaceous materials that showed higher specific capacities than graphite, as reported earlier.[35] The augmentation might also be owing to other reactions such as the reversible growth of a polymer/gel-like film caused by decomposition of the electrolyte on the transition-metal oxide during the conversion

reaction.[40] CBIOs exhibited a capacity of 800 mAh g^{-1} initially, but degraded very rapidly until 50 cycles. At 50 cycles, they showed only 19.6% of capacity retention, and the measurement was stopped. Clear capacity fading was observed in the RAIONs and CBIOs, in comparison to the MIONCs. The initial coulombic efficiencies (CEs) of the MIONCs and RAIONs were 73.4% and 69.0%, respectively. The CEs of the MIONCs increased steadily after several cycles and rapidly approached up to 99.7%. In contrast, the RAIONs showed an oscillating CE of 95–97% after two cycles, indicating their lower reversibility than that of the MIONCs. Because the loss of just 1% CE in each cycle can give rise to nearly complete degradation of the balanced full cell after 100 cycles,[25] this difference in CE indicates the superior reversibility of the MIONCs.

This stable reversibility was also manifested in the rate performance at various current densities (Figure 2.8.b). At low current densities (less than 400 mA g^{-1}), the specific capacities of the MIONCs were lower than those of the RAIONs. However, at high current densities (higher than 800 mA g^{-1}), the MIONCs showed higher reversible capacities than the RAIONs. Even at 1600 mA g^{-1}, the reversible capacity delivered by the MIONCs (473 mAh g^{-1}) was 61% of the value at 100

mA g^{-1}; this is even higher than the theoretical capacity of commercially available graphite (372 mAh g^{-1}). On the other hand, only 27% of the capacity at 100 mA g^{-1} was recorded at 1600 mA g^{-1} in the RAIONs. Clearly, the modification in the geometric configurations allows lithium ions to approach the active materials of the MIONCs rapidly, in despite of their larger overall size.
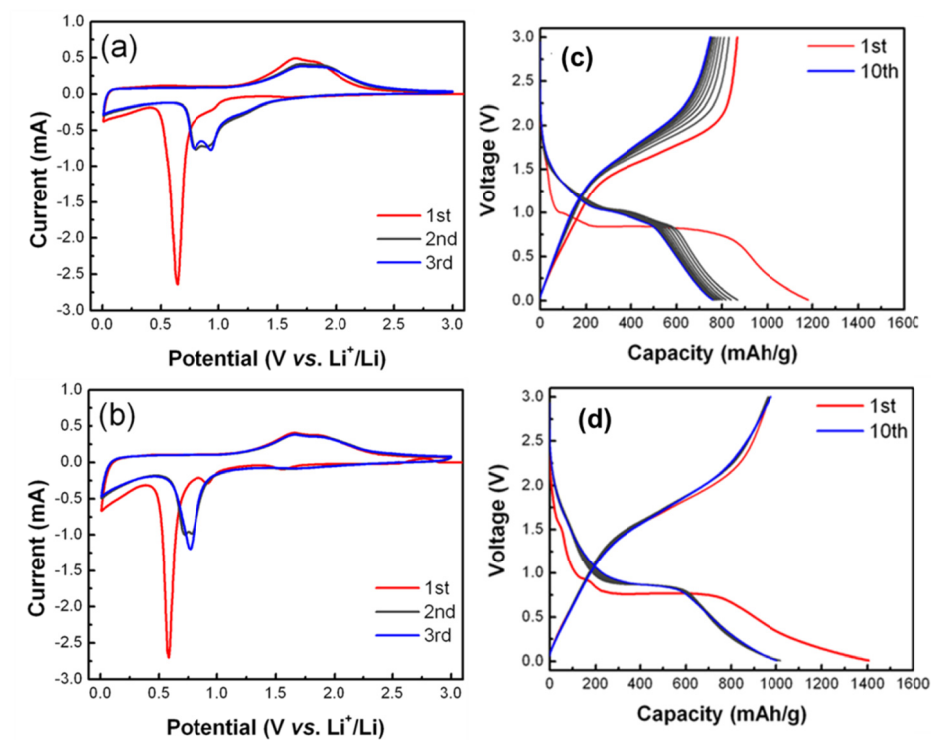
Figure 2.7. Cyclic voltammograms of (a) MIONCs and (b) RAIONs at a scan rate of 0.1 mV s^{-1}. Galvanostatic charge and discharge voltage profiles of (c) MIONCs and (d) RAIONs at a current density of 100 mA g^{-1} for 10 cycles.
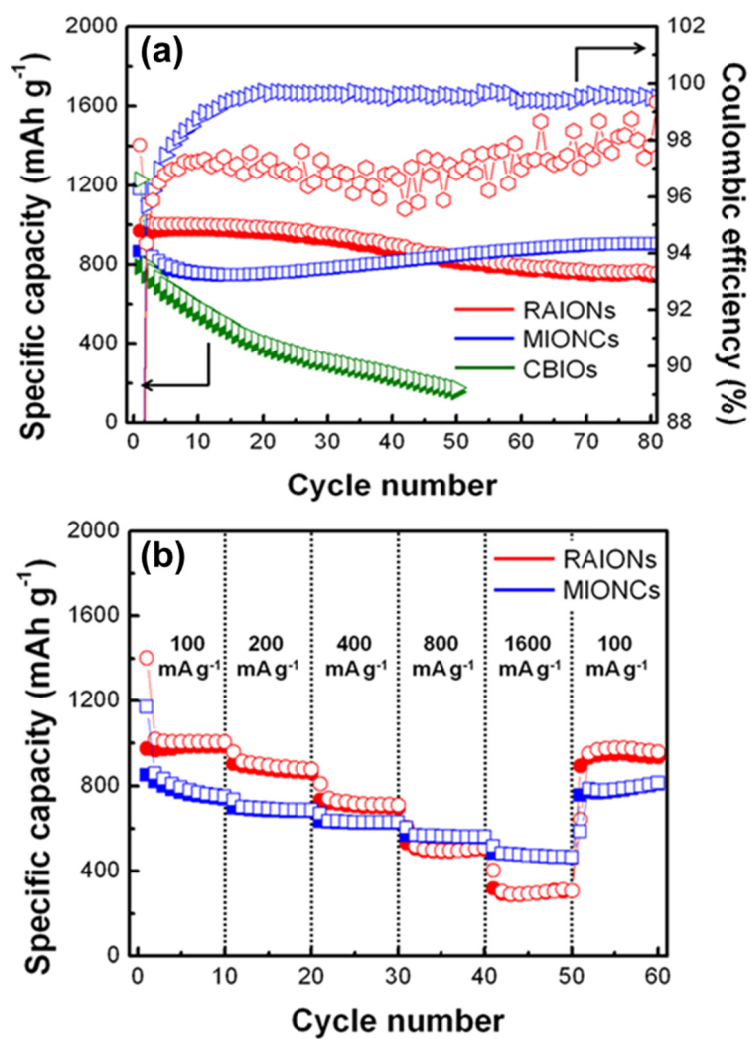
Figure 2.8. (a) Cycle performances of MIONCs, RAIONs and CBIOs at a current density of 0.1 A g^{-1}. (b) Rate properties of MIONCs and RAIONs.

2.3.4. SEI Formation Analysis

By comparing the electrochemical performances of the MIONCs and RAIONs, we can estimate on the attractive characteristics of the MIONCs, which showed more stable and higher rate performances. First, metallic iron particles, which are inactive toward lithium ions in the voltage range 0.01–3V, can play role as a buffer to reduce electrode swelling when intimate contact is made between inactive and active components, as reported in the previous study.[22] To prove this fact, we compared XRD patterns of the CBIOs and MIONCs before and after cycling (Figure 2.9.a,b). Although CBIOs were transformed into amorphous state during the first cycle, MIONCs maintained metallic iron after first cycle. Thus, metallic iron particles in MIONCs sample are inactive toward lithium ions. In addition, metallic iron has much greater electrical conductivity (two orders of magnitude higher) than Fe_3O_4; this utilizes an electrical conductive network by reducing the internal resistance.[41] However, these advantages are only restricted locally because metallic iron particles are much bigger than the constituting Fe_3O_4 NPs, and relative fraction of metallic iron is much smaller (~6 wt.%) than that of Fe_3O_4 phase. Second, the uniform void spaces originated from the gaps between neighboring NPs of the self-

assembled mesoporous structure can provide a "buffer space" to relieve the volume expansion during lithiation and delithiation. Therefore, the overall morphology can be maintained without any aggregation of primary nanoparticles after long cycles. In addition, the mesoporous structure provides short diffusion paths for lithium ions, resulting in a high rate capability. The RAIONs also have randomly distributed pores that can alleviate volume expansion. Furthermore, carbon coating, which can endow some mechanical strength against deformation, seemed to supply electron-transfer channels.[36] To test the effects of carbon coatings, we compared two RAIONs samples with different carbon contents (Figure 2.9.c). As a result, RAIONs sample with low carbon contents (17 wt%) exhibited rapid capacity degradation until 20 cycles. Therefore, carbon coatings are crucial to the battery performance. However, the random distribution of the pores and carbon coatings deriving from the ligands of the Fe_3O_4 NPs is not sufficient to prevent the aggregation of particles. Finally, the MIONC structure can retain its morphology with a stable SEI layer during cycling (Figure 2.10). On the other hand, the RAIONs show a high surface area exposed to electrolytes and additional surface exposure upon cycling, leading to excessive and repeated SEI formation. Randomly distributed

1 1 3

pores can give rise to a concentration gradient of lithium ions, consequently stress relaxation[42] and SEI formation cannot be controlled efficiently. As verification of this assumption, the MIONCs and RAIONs (Figure 2.11.a,b) were subjected to different cycling processes and the resulting structures were characterized by SEM and TEM. The MIONCs showed a stable and thin SEI layer on their individual surfaces exclusively (Figure 2.11.c). However, a thick and excessive SEI layer was formed on the RAIONs after only one lithiation/delithiation cycle in the whole region (Figure 2.11.d). This difference was visible more obviously on the electrode surfaces after 20 cycles. The intact morphology of the MIONCs can be observed clearly with a limited SEI layer on their surfaces (Figure 2.11.e), but the RAIONs are buried under thick SEI layers (Figure 2.11.f). TEM images after 20 cycles showed a thin SEI layer on the surface of each cluster with pores inside the MIONCs (inset of Figure 2.11.e), whereas an excessive SEI layer was formed on the RAIONs (inset of Figure 2.11.f). Because excessive SEI formation is associated to rapid capacity fading and low rate capabilities and CEs, the MIONC structure permits an outstandingly stable battery performance and high-power rate capabilities. To confirm the material stability, which is directly

1 1 4

associated to battery cyclic stability, we performed selective etching of the SEI, as reported previously.[43] After selective etching of the SEI, the MIONCs showed a morphology similar to that before cycling (Figure 2.12.a). However, after SEI removal from the RAIONs, the SEM images exhibited more aggregated morphology than in the initial state (Figure 2.12.b). The TEM image after SEI removal from the MIONCs also exhibited that their morphology was intact in comparison to before cycling, demonstrating high mechanical stability (Figure 2.12.c). However, the resulting morphology for the RAIONs after etching of the SEI layer showed that some Fe_3O_4 NPs were aggregated (Figure 2.12.d) and exhibited a different morphology from the initial state. Both the MIONC and RAION materials revealed an amorphous nature after battery cycling, as seen by their ED patterns (insets of Figures 2.12.c,d). This robustness of the MIONC structure suggests that we can limit SEI formation to the outer surface of the MIONCs simply by modifying their geometric configuration. Thus, the application of a bottom-up self-assembly method endows new collective properties such as a stable SEI formation and resistance to mechanical degradation, which was not observed in the case of primary nanoparticles.

1 1 5
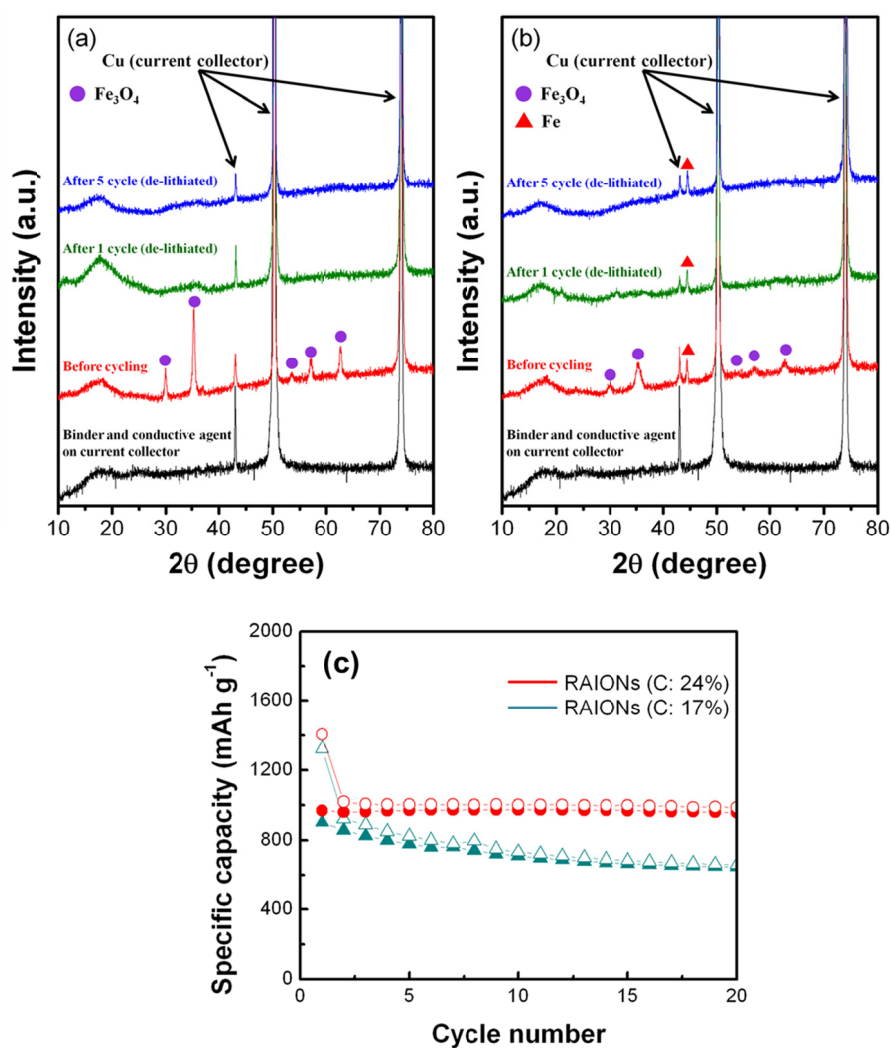
Figure 2.9. XRD patterns of (a) CBIOs and (b) MIONCs before and after cycling. (c) Cycle performances of RAIONs with different carbon contents. Two kinds of RAIONs were prepared by applying different washing steps
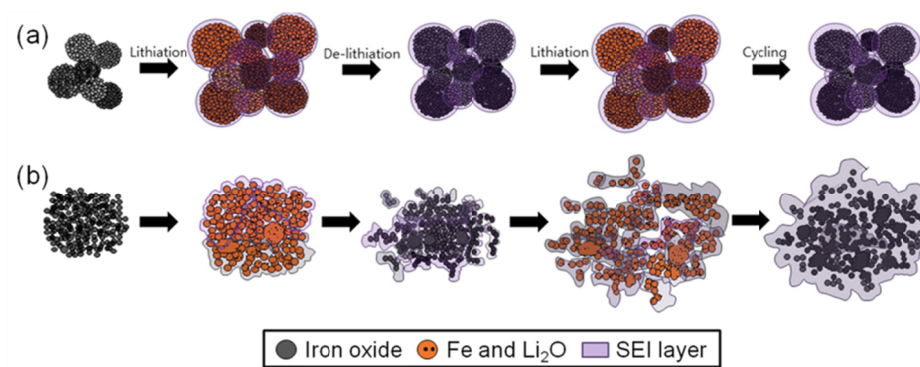
Figure 2.10. Schematic illustration of SEI formation on MIONCs and RAIONs. (a) In the case of MIONCs, the outer surface of the MIONCs can form a stable SEI because each composite NP is tightly confined by neighboring NPs. Also, the original morphology can be retained after several cycles. (b) The RAIONs have a higher surface area exposed to electrolytes and there is no confinement of nanoparticles against SEI formation. During lithiation and delithiation, the SEI can shrink and break down freely and continuously, resulting in excessive SEI formation.

1 1 7
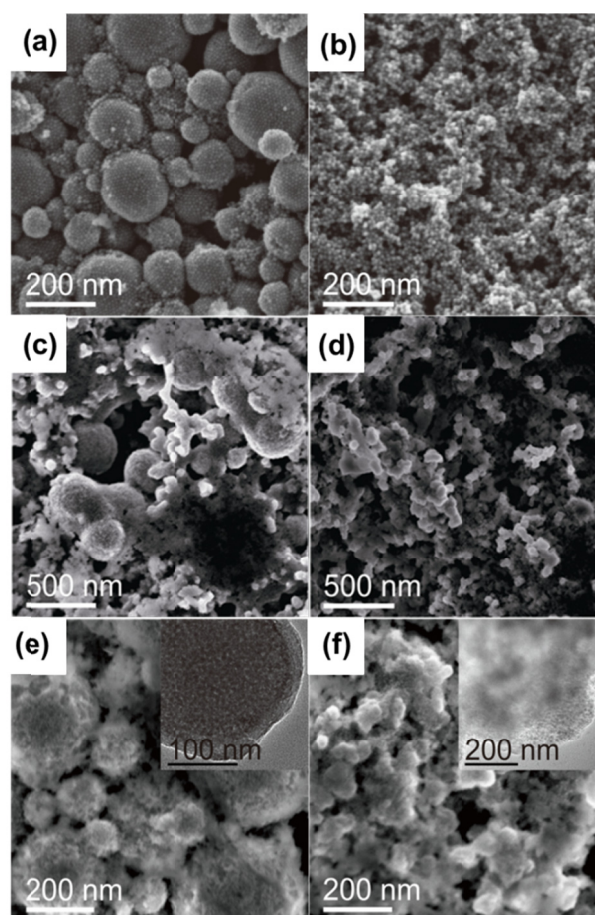
Figure 2.11. Comparison of MIONC and RAION electrodes before and after cycling. SEM images of initial (a) MIONCs and (b) RAIONs before cycling. SEM images of (c,e) MIONCs and (d,f) RAIONs after 1 cycles and 20 cycles respectively. Insets of (e) and (f) show high-magnification TEM images.
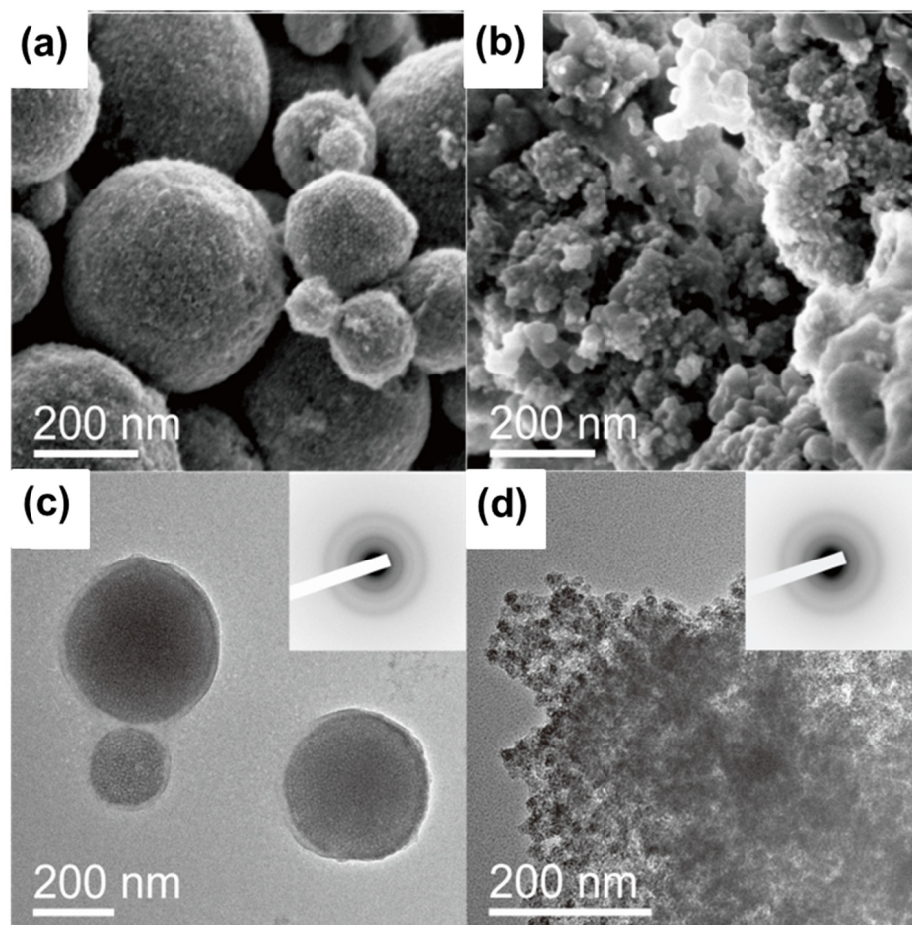
Figure 2.12. SEM and TEM images of MIONCs (a, c) and RAIONs (b, d) are shown respectively after 20 cycles in which the SEI was removed selectively by chemical etching. Insets of TEM images (c, d) show ED patterns of corresponding samples.

2.4 Conclusions

In summary, mesoporous iron oxide nanoparticle clusters with carbon coating were prepared successfully and applied as anode materials for LIBs. The unique structure imparted the MIONCs with enhanced capacity retention, rate capability, and coulombic efficiency. More importantly, the results proved that modifying the geometric configuration can result in the confinement of SEI layer formation, leading to stable battery performance. This synthetic strategy can be considered a model framework and applied to other metal oxide NPs such as Co_3O_4 and NiO with high specific capacities. These findings further confirm that bottom-up self-assembly of active materials can improve battery performance.

Many parts of this chapter have been published in Soo Hong Lee, Seung-Ho Yu, Ji Eun Lee, Aihua Jin, Dong Jun Lee, Nohyun Lee, Hyungyung Jo, Kwangsoo Shin, Tae-Young Ahn, Young-Woon Kim, Heeman Choe, Yung-Eun Sung, and Taeghwan Hyeon,
"Self-Assembled Fe_3O_4 Nanoparticle Clusters as High Performance Anodes for Lithium-Ion Batteries via Geometric Confinement,"
Nano Letters, **2013**, *13*, 4249-4256.

2.5 References

[1] Poizot, P.; Laruelle, S.; Grugeion, S.; Dupont, L.; Tarascon, J.-M. *Nature*, **2000**, *407*, 496-499.

[2] Bruce, P. G.; Scrosati, B.; Tarascon, J.-M. *Angew. Chem. Int. Ed.* **2008**, *47*, 2930-2946.

3] Aricò, A. S.; Bruce, P.; Scrosati, B.; Tarascon, J.-M.; van Schalkwijk, W. *Nat. Mater.* **2005**, *4*, 366-377.

[4] Choi, N.-S.; Chen, Z.; Freunberger, S. A.; Ji, X.; Sun, Y.-K.; Amine, K.; Yushin, G.; Nazar, L. F.; Cho, J.; Bruce, P. G. *Angew. Chem. Int. Ed.* **2012**, *51*, 9994-10024.

[5] Cheng, Y.-T.; Verbrugge, M. W. *J. Appl. Phys*. **2008**, *104*, 083521.

[6] Wu, H.; Chan, G.; Choi, J. W.; Ryu, I.; Yao, Y.; Mcdowell, M. T.; Lee, S. W.; Jackson, A.; Yang, Y.; Hu, L.; Cui, Y. *Nat. Nanotechnol*. **2012**, *7*, 310-315.

[7] Aurbach, D. *J. Power Sources* **2000**, *89*, 206-218.

[8] Zhang, W.-M.; Wu, X.-L.; Hu, J.-S.; Guo, Y.-G.; Wan, L.-J. *Adv. Funct. Mater*, **2008**, *18*, 3941-3946.

[9] Kang, E.; Jung, Y. S.; Cavanagh, A. S.; Kim, G.-H.; George, S. M.; Dillon, A. C.; Kim, J. K.; Lee, J. *Adv. Funct. Mater.* **2011**, *21*, 2430-2438.

[10] Piao, Y.; Kim, H. S.; Sung, Y.-E.; Hyeon, T. *Chem. Commun.* **2010**, *46*, 118-120.

[11] Demir-Cakan, R.; Hu, Y.-S.; Antonietti, M.; Maier, J.; Titirici, M.-M. *Chem. Mater.* **2008**, *20*, 1227-1229.

[12] Jiao, F.; Bao, J.; Bruce, P. G. *Electrochem. Solid-state Lett.* **2007**, *10*, A264-A266.

[13] Ren, Y.; Armstrong, R.; Jiao, F.; Bruce, P. G. *J. Am. Chem. Soc.* **2010**, *132*, 996-1004.

[14] Kim, H.; Han, B.; Choo, J.; Cho, J. *Angew. Chem. Int. Ed.* **2008**, *47*, 10151-10154.

[15] Ren, Y.; Hardwick, L. J.; Bruce. P. G. *Angew. Chem. Int. Ed.* **2010**, *122*, 2624-2628.

[16] Yu, Y.; Gu, L.; Wang, C.; Dhanabalan, A.; van Aken, P. A.; Maier, J. *Angew. Chem. Int. Ed.* **2009**, *48*, 6485-6489.

[17] Lou, X. L.; Li, C. M.; Archer, L. A. *Adv. Mater.* **2009**, *21*, 2536-2539.

[18] Ding, S.; Chen, J. S.; Qi, G.; Duan, X.; Wang, Z.; Giannelis, E. P.; Archer, L. A.; Lou, X. W. *J. Am. Chem. Soc.* **2011**, *133*, 21-23.

[19] Koo, B.; Xiong, H.; Slater, M. D.; Prakapenka, V. B.; Balasubramanian, M.; Podsiadlo, P.; Johnson, C. S.; Rajh, T.;

Shevchenko, E. V. *Nano Lett.* **2012**, *12*, 2429-2435.

[20] Chan, C. K.; Peng, H.; Liu, G.; Mcilwrath, K.; Zhang, X. F.; Huggins, R. A.; Cui, Y. *Nat. Nanotechnol.* **2008**, *3*, 31-35.

[21] Kim, J.; Chung, M. K.; Ka, B. H.; Ku, J. H.; Park, S.; Ryu, J.; Oh, S. M. J. *Electrochem. Soc.* **2010**, *157*, A412-A147.

[22] Liu, N.; Wu, H.; McDowell, M. T.; Yao, Y.; Wang, C.; Cui, Y. *Nano Lett.* **2012**, *12*, 3315-3321.

[23] Wu, H.; Zheng, G.; Liu, N.; Carney, T. J.; Yang, Y.; Cui, Y. *Nano Lett*. **2012**, *12*, 904-909.

[24 Herzberg, B.; Alexeev, A.; Yushin, G. *J. Am. Chem. Soc.* **2010**, *132*, 8548-8549.

[25] Park, J.; An, K.; Hwang, Y.; Park, J.-G.; Noh, H.-J.; Kim, J.-Y.; Park, J.-H.; Hwang, N.-M.; Hyeon, T. *Nat. Mater.* **2004**, *3*, 891-895.

[26] Cao, A.; Veser, G. *Nat. Mater*. **2010**, *9*, 75-81.

[27] Magasinski, A.; Dixon, P.; Hertzberg, B.; Kvit, A.; Ayala, J.; Yushin, G. *Nat. Mater.* **2010**, *9*, 353-358.

[28] Chen, C.; Nan, C.; Wang, D.; Su, Q.; Duan, H.; Liu, X.; Zhang, L.; Chu, D.; Song, W.; Peng, Q.; Li, Y. *Angew. Chem. Int. Ed.* **2011**, *50*, 3725-3729.

[29] Lu, Z.; Yin, Y. *Chem. Soc. Rev.* **2012**, *41*, 6874-6887.

[30] Zhuang, J.; Wu, H.; Yang, Y.; Cao, Y. C. *Angew. Chem. Int. Ed.* **2008**, *47*, 2208-2212.

[31] Azhari, S. J.; Diab, M. A. *Polym. Degrad. Stab.* **1998**, *60*, 253-256.

[32] Jiao, F.; Jumas, J.-C.; Womes, M.; Chadwick, A. V.; Harrison, A.; Bruce, P. G. *J. Am. Chem. Soc.* **2006**, *128*, 12905-12909.

[33] Mohanan, J. L.; Arachchige, I. U.; Brock, S. L. *Science*, **2005**, *307*, 397-400.

[34] Pan, D.; Wang, S.; Zhao, B.; Wu, M.; Zhang, H.; Wang, Y.; Jiao, Z. *Chem. Mater.* **2009**, *21*, 3136-3142.

[35] Jang, B.; Park, M.; Chae, O. B.; Park, S.; Kim, Y.; Oh, S. M.; Piao, Y.; Hyeon, T. *J. Am. Chem. Soc.* **2012**, *134*, 15010-15015.

[36] Ban, C.; Wu, Z.; Gillaspie, D. T.; Chen, L.; Yan, Y.; Blackburn, J. L.; Dillon, A. C. *Adv. Mater.* **2010**, *22*, E145-E149.

[37] Zhou, L.; Wu, H. B.; Zhu, T.; Lou, X. W. *J. Mater. Chem.* **2012**, *22*, 827-829.

[38] Lee, J. E.; Yu, S.-H.; Lee, D. J.; Lee, D. C.; Han, S. I.; Sung, Y.-E.; Hyeon, T. *Energy Environ. Sci.* **2012**, *5*, 9528-9533.

[39] Laruelle, S.; Grugeon, S.; Poizot, P.; Dollé, M.; Dupont, L.;

Tarascon, J.-M. *J. Electrochem. Soc.* **2002**, *149*, A627-A634.

[40] Taberna, P. L.; Mitra, S.; Poizot, P.; Simon, P.; Tarascon, J.-M.

Nat. Mater. **2006**, *5*, 567-573.

[41] Ge, M.; Rong, J.; Fang, X.; Zhou, C. *Nano Lett.* **2012**, *12*, 2318-

2323.

[42] Choi, J. W.; McDonough, J.; Jeong, S.; Yoo, J. S.; Chan, C. K.;

Cui, Y. *Nano Lett.* **2010**, *10*, 1409-1413.

Chapter 3. Optimization of Hierarchical Porous Fe-N-C Electrocatalysts for Oxygen Reduction Reaction

3.1 Introduction

Non-precious metal catalysts have been extensively developed to replace expensive Pt/C electrodes, which facilitate the oxygen reduction reaction (ORR) at the cathode.[1] Among them, Fe-N-C catalysts bind H_2O_2 and OH more strongly than other catalysts, leading to high selectivity for the four-electron process.[2,3] The atomic configuration of the active sites in the Fe-N-C catalysts, such as Fe-N$_x$ in the micropores or Fe/Fe$_3$C in N-doped carbons, has been firmly established.[4-10] However, the actual fuel cell performance not only depends on the atomic configuration of the active sites but also heavily depends on the structural factors, such as the active site utilization and mass transfer properties.[11,12] To improve the structural factors, various kinds of Fe-N-C catalysts with hierarchical macro/mesoporous structures have been proposed.[13-18] However, the

majority of relationships published to date relating the porosity to the ORR activity are based on empirical measurements without detailed electrochemical analysis, leading to inconsistent optimum values or morphologies. A complex capacitance analysis of porous carbon electrodes, which are employed as electric double-layer capacitor electrodes, could be a solution to optimize the size and morphology of the catalysts to maximize the active site utilization and mass transfer properties.

Herein, we conducted a systemic optimization of Fe-N-C catalysts to maximize the ORR activity in alkaline media. To prepare the model carbon-based support system, we developed a synthetic method for a hierarchically macro/mesoporous N-doped carbon nanoparticle (HMNC) system based on commercial precursors and using a facile hydrothermal reaction. This method allows the simultaneous size-control and modulation of the porous structure. Through comparisons with control groups using complex capacitance analysis, we can conclude that a mesoporous structure is essential to increase the utilization of the active sites, whereas a nano-sized particulate morphology is needed to obtain a superior rate capability. By combining spectroscopic and electrochemical analyses, we are able to

show that the ORR activities before NH$_3$ activation of the catalyst mainly stem from N-doped carbon and the subsurface Fe/Fe$_3$C, regardless of the structural factors. In contrast, preventing the formation of Fe/Fe$_3$C is vital to achieving a high ORR activity after NH$_3$ activation. This systematic optimization results in a highly reactive Fe-N-C catalyst, which exhibited one of the best ORR performances in alkaline medium. During accelerated durability tests, our optimized catalysts show negligible activity loss over 10,000 potential cycles, demonstrating excellent long-term stability.

3.2 Experimental Section

3.2.1. Synthesis of Hierarchically Micro/Mesoporous N-doped Carbon Nanoparticles (HMNCs)

In a typical synthesis, 0.6 g of phenol, 2.4 g of melamine, and 15 mL of 0.1 M NaOH aqueous solution were mixed and stirred at 430 rpm. After the solution had been heated to 50 °C, 4.2 mL of formaldehyde solution (37 wt%) was added and stirred at 70 °C for 30 min. Then, 0.96 g of Pluronic F127 dissolved in 15 mL of distilled water was added and stirred at 66 °C at a stirring rate of 340 rpm for 2 h. Then, 50 mL of distilled water was added to dilute the solution. The reaction was stopped after 17 h. After cooling to room temperature, 15 mL of the resulting solution was diluted with 56 mL of distilled water and transferred to a Teflon lined autoclave and heated at 120 °C for 24 h. The resultant spherical nanoparticles can be obtained with various diameters by changing the amount of solution (9 mL for 67 nm; 12 mL for 118 nm; 15 mL for 182 nm; 18 mL for 242 nm; and 21 mL for 290 nm) diluted with 56 mL of distilled water. For micrometer-sized HMNCs (Micro_HMNC), 56 mL of resulting solution directly underwent hydrothermal reaction without dilution. The resulting

nanoparticles were washed with distilled water three times through vacuum filtration and dried under vacuum. Finally, carbonization was carried out under vacuum condition (<0.1 Torr). For sufficient soft-template removal, a stepwise carbonization process (1 °C min^{-1} up to 350 °C, 2 h aging, 1 °C min^{-1} up to 600 °C, and 5 °C min^{-1} up to 700 °C, 2 h aging) was applied. For non-porous N-doped carbon nanoparticles (HMNC_Ar), carbonization under Ar gas flow of 100 standard cubic centimeters per minute (sccm) was carried out with the same carbonization process.

3.2.2 Synthesis of Fe-loaded HMNC (Fe$_x$-HMNC, x=1.9, 10, and 100)

For Fe$_x$_HMNC, 380 mg of the resulting nanoparticles were re-dispersed in 40 mL EtOH (99.9%, anhydrous). Then, three different amounts of iron(III) chloride hexahydrate (1.9, 10, and 100 mg for Fe$_{1.9}$_HMNC, Fe$_{10}$_HMNC, and Fe$_{100}$_HMNC, respectively) were added and stirred at room temperature for 20 h. Then, the product was washed with EtOH four times and centrifuged at 10,000 rpm and dried under vacuum for more than 12 h. The same stepwise carbonization process was finally carried out under vacuum conditions (<0.1 Torr) at

700 °C.

3.2.3. Ammonia Activation for HMNC(A) and Fe$_x$_HMNC(A)

A second heat treatment under ammonia gas was carried out to synthesize Fe$_x$(A)_HMNC. As-prepared HMNC and Fe$_x$_HMNC were placed into a tube furnace and heated to 900 °C (ramping rate = 5 °C min^{-1}) under Ar gas (100 sccm). Once the temperature had reached 900 °C, the Ar gas was switched to NH$_3$ gas with a flow rate of 60 sccm. After 15 min of heat treatment under NH$_3$ gas, the resulting samples were cooled to room temperature under Ar gas flow (100 sccm).

3.2.4. Characterizations

Transmission electron microscopy (TEM) was performed by using a JEOL JEM-2100F (JEOL) microscope at an acceleration voltage of 200 kV. High angle annular dark field-scanning TEM (HAADF-STEM) and energy dispersive spectroscopy (EDS) analysis were obtained with a JEOL JEM-2100F (JEOL) microscope. The X-ray diffraction patterns (XRD) were obtained using a Rigaku D/Max 2500 diffractometer system. Small angle X-ray scattering (SAXS)

measurements were carried out using a SmartLab (Rigaku, Japan) using an X-ray source with a Cu target (wavelength: 1.5412 Å). Nitrogen sorption isotherms were measured at 77 K using a 3-FLEX surface characterization analyzer (Micromeritics, USA). Before measurement, the samples were degassed under vacuum at 200 °C for 12 h. The Brunauer–Emmett–Teller (BET) method was used to calculate the specific surface area, and the pore volume was deduced from the adsorbed quantity of nitrogen at $P/P_o = 0.99$. The pore size distribution was obtained using the Barrett–Joyner–Halenda (BJH) desorption isotherm, and the microporosity data was calculated by t-plot analysis. Elemental analysis was conducted using a Flash 2000 elemental analyzer (Thermo Scientific). Fourier-transform infrared (FT-IR) analysis was conducted using a VERTEX80v FT-IR spectrophotometer (Bruker, Germany). X-ray photoelectron spectroscopy (XPS) data was measured by SIGMA PROBE (SelectScience, UK). The microtoming of nanoparticles was carried out using an MTX Ultramicrotome (RMC, USA). Thermogravimetric analysis (TGA) was carried out using an SDT Q600 apparatus (TA Instruments, USA) under Ar gas from room temperature to 900 °C at 5 °C min^{-1}. Raman spectroscopy was carried out using a LabRAM HV

Evolution (HORIBA, Japan) with an excitation laser of 532 nm. X-ray absorption near-edge spectroscopy (XANES) and extended X-ray absorption fine structure (EXAFS) measurements were performed at the Pohang Accelerator Laboratory (PAL, beamline 8C).

3.2.5. Electrochemical Measurement

All electrochemical measurements were carried out using PGSTAT 302 (Metrohm Autolab) potentiostat in a three-electrode system. The counter and reference electrodes were a glassy carbon rod and Ag/AgCl electrode, respectively. The rotating ring-disk electrode (RRDE, Pine instrument) was used as the working electrode, and its area was 0.2475 cm^2. All potentials are reported with respect to the reversible hydrogen electrode (RHE) by measuring the equilibrium potential of hydrogen oxidation/evolution in an H$_2$-saturated electrolyte using a Pt electrode. The catalyst ink was prepared by mixing a catalyst, Nafion ionomer (15 wt%, Sigma Aldrich), and 2-isopropanol (Sigma Aldrich). The catalyst loading of carbon-based materials except Pt was fixed at 0.274 mg cm^{-2}. To compare the activity, 20 wt% commercial Pt electrocatalyst (Johnson Matthey) was used. The Pt loading was 16 μg$_{Pt}$ cm^{-2}. Before the ORR measurements,

we conducted potential cycles from 0.05 to 1.0 V to obtain reproducible data. The ORR activity was measured by potential cycling method with rotation speed 1600 rpm and a scan rate of 20 mVs^{-1}. The non-faradaic capacitive effect was compensated for by measurement under Ar saturated conditions, and an iR correction was made. To quantify the electron transfer number during the ORR measurements, the ring disk (Pt) potential was held at 1.4 V vs. RHE, and the electron transfer number was calculated. The long-term durability tests were conducted by the potential sweep method between 0.6 to 1.0 V with a scan rate of 50 mVs^{-1} in an O_2-saturated electrolyte.

3.2.6. Electrochemical Impedance Spectroscopy (EIS) and Capacitance Analysis

Electrochemical impedance spectroscopy (EIS) analysis was carried out in the three-electrode configuration, as for the ORR measurements, using an EIS instrument (Zennium, Zahner). Before the EIS measurements, the electrode was equilibrated for around 10 min at the open circuit potential (OCP). The measurements were conducted at the OCP in the frequency range from 50 mHz to 100 kHz with an AC

amplitude of 10 mV. The complex capacitance ($C(\omega)$) is defined as follows:

$$Z(w) = \frac{1}{jwC(w)'}$$

$$C(w) = C'(w) - jc''(w)$$

$$C' = \frac{-Z''(w)}{w|Z(w)|^2} , C'' = \frac{Z'(w)}{w|Z(w)|^2}$$

where $Z(\omega)$ is the impedance and ω is the penetration depth. The real part of the complex capacitance ($C'(\omega)$) indicates the capacitance as a function of frequency. The imaginary part ($C''(\omega)$) is related to the energy dissipation of the capacitor by an irreversible process, such as *iR* drop and irreversible faradaic charge transfer. In general, the total static capacitance (C_0) is extracted from the flat value in the plot of $C'(\omega)$ as a function of frequency in the low frequency region. However, flat features were not clearly observed in our samples. Therefore, we estimated the static capacitance from the $C''(\omega)$ plot based on the complex capacitance analysis model. The integrated area under the C'' (ω) curve is proportional to the capacitance of the active carbons based on the Kramers–Kronig relationship.

$$A = -\int_{-\infty}^{\infty} C''(w)\,d\log f = 0.682 C_0$$

Here, A is the peak area, and C_0 is the total static capacitance. Because of the technical difficulty in measuring at very low frequencies, we calculated C_0 using the following equation.

$$C_0 = -\frac{2}{0.682} A_{half}, \qquad A_{half} = \int_{f_0}^{10^5} C''(w)\,d\log f$$

The A_{half} is the area under $C''(\omega)$ from the peak frequency to the maximum frequency, 100 kHz in our experimental condition, and f_0 is the peak potential.

To compare the capacitance from the EIS and cyclic voltammetry (CV), the static capacitance (C_0) derived from EIS is denoted C_{dl_EIS}, and the capacitance derived from CV is denoted C_{dl_CV}. The CV measurements were carried out at 20 mV s^{-1}, which is same scan rate as the ORR measurements. The specific capacitance determined by CV (C_{dl_CV}, F g^{-1}) was estimated using the following equation.

$$C_{dl\_CV} = \frac{1}{2vm\Delta V}\int I\,dV$$

Here, v is the scan rate (ms^{-1}), m is the mass of active materials (g), ΔV

is the potential window, and $\int I \, dV$ indicates the area under the CV curve.

We now define two parameters to express how porous electrode materials can be effectively utilized in a quantitative manner. The first term is the ideal efficiency of the electrode (η_{ideal}). The η_{ideal} is defined by the ratio between the surface area derived by BET and the capacitance derived by EIS, as follows.

$$\eta_{ideal} = \frac{C_{dl\_}EIS}{BET \; Surface \; Area}$$

Considering that $C_{dl\_}EIS$ indicates the static specific capacitance, which is related to the ideal electrochemical surface area of systems under very static conditions and the BET surface area is the physical surface of a given structure, η_{ideal} indicates the how liquid/solid interface is effectively established in a given electrode pore structure, excluding kinetic effects, which are related to the wetting properties.

To consider kinetic issues, we can also define real efficiency of the electrode (η_{real}) as follows.

$$\eta_{real} = \frac{C_{dl\_}CV}{C_{dl\_}EIS}$$

η_{real} is related to how the electrochemical surface area can be utilized in the real systems. Because the C_{dl}_EIS is the static potential electrochemical surface area regardless of the kinetic issues, the ratio between C_{dl}_CV, which is affected by the kinetic values, and C_{dl}_EIS indicates the real utilization of the electrode material at a given timescale.

3.2.7. Transmission Line Model Analysis.

EIS is the most commonly used technique to investigate electrochemical systems, allowing the investigation of reaction mechanisms in a non-destructive manner and on different timescales. The transmission line model (TLM) describes not only the capacitive behavior of a porous electrode but also the time-dependent penetration depth analysis for the overall electrode structure, which are important criteria for the utilization of porous electrodes in various electrochemical systems.

3.3 Result and Discussion

3.3.1. Synthesis of Hierarchical N-doped Mesoporous Carbon

To obtain a model system for optimizing the Fe-N-C catalysts, we developed a synthetic method for preparing N-doped mesoporous carbon materials with controllable size and porous structure. For facile and economical synthesis, this material was synthesized by using phenol resin (PR) as the carbon precursor, melamine resin (MR) as the nitrogen source, and the block copolymer Pluronic F127 as soft-template for the mesoporous structure.[19] The resulting phenol-melamine resin (PMR) can form hydrogen bonds with the F127. Upon the subsequent hydrothermal treatment, the self-assembled structures were further solidified into the PMR composite polymer with an ordered mesoporous structure (Figure 3.1). The morphology of the resulting PMR nanoparticles was confirmed by TEM (Figure 3.2.a). The successful co-condensation between the PR and MR was confirmed by FT-IR (Figure 3.2.b). If only MR was used in the synthesis, the resulting particles were irregular microspheres with no mesoporous structure (Figure 3.2.c,d). The size control of the composite polymer was achieved by simply varying the concentration

1 3 9

of the PMR during the hydrothermal reaction. The particle size can be tuned from 67 nm to micrometer-sized while maintaining the ordered mesoporous structure (Figure 3.3). The N contents of the HMNCs were controlled by the temperature of the subsequent carbonization (Figure 3.4.a). The carbonization temperature was optimized at 700 °C in a vacuum (<0.1 Torr) by measuring various physicochemical properties and the ORR performance (Figure 3.3.b).
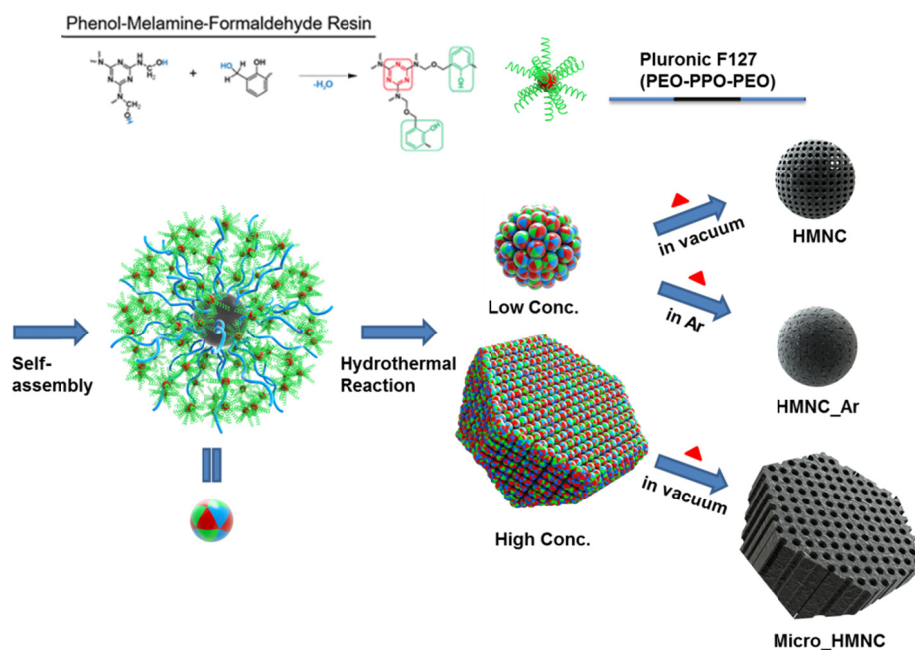
Figure 3.1. Schematic illustration of hierarchical N-doped carbon nanoparticles (HMNC), microporous N-doped carbon nanoparticles (HMNC_Ar), and micro-sized N-doped carbon nanoparticles (Micro_HMNC).
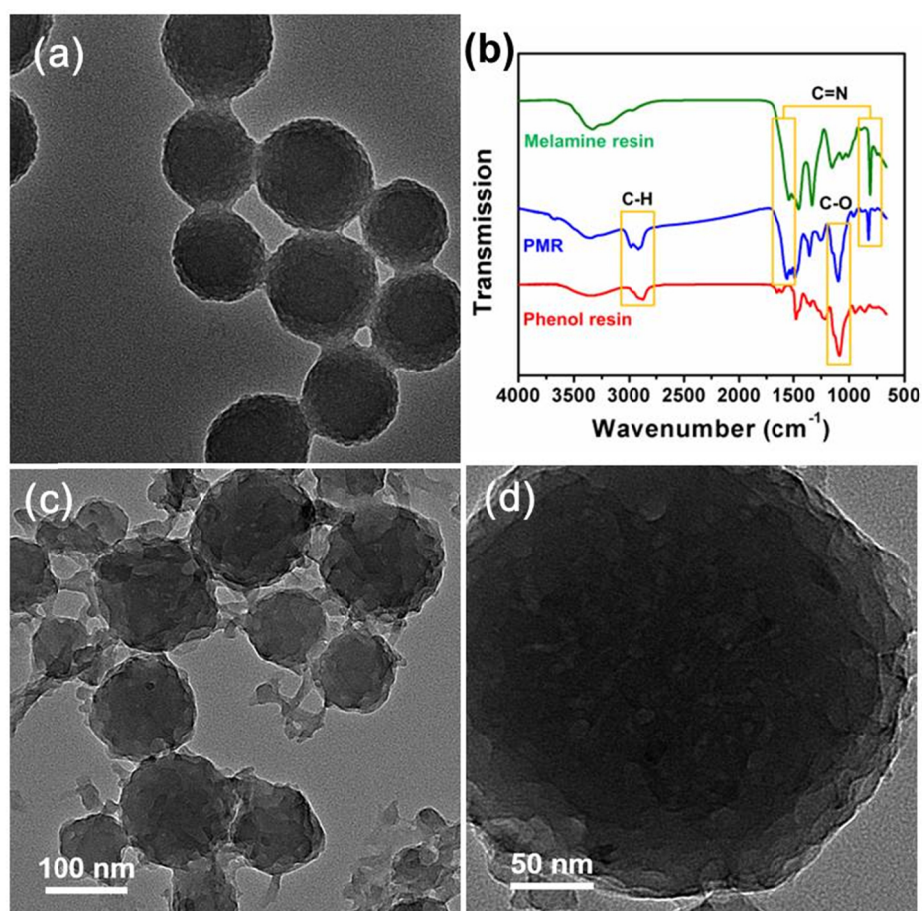
Figure 3.2. (a) TEM image of phenol-melamine resin (PMR) nanoparticles. (b) FT-IR spectra of PMR, phenol resin, and melamine resin. (c, d) TEM images of a melamine resin nanoparticle.
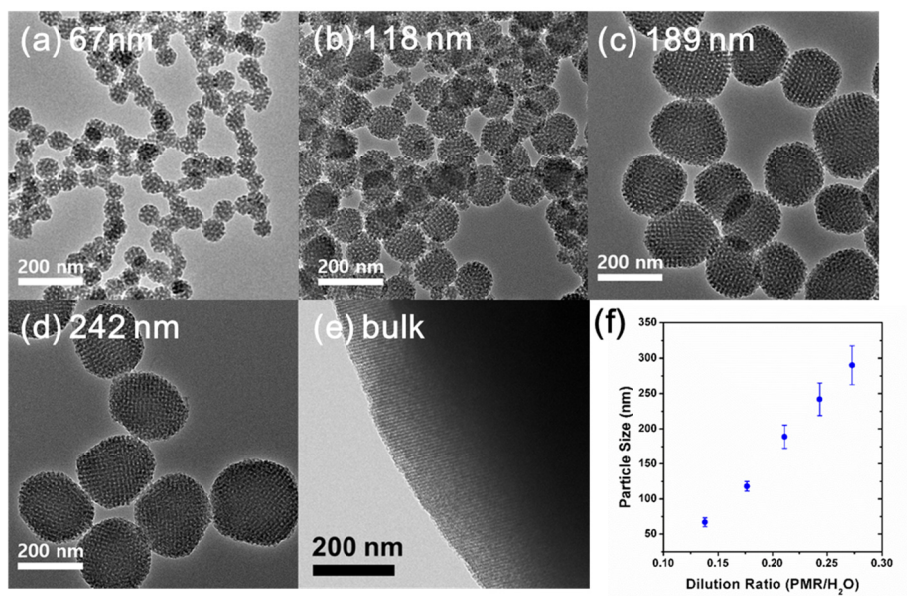
Figure 3.3. (a–e) TEM images of size-controlled PMR nanoparticles. Each average diameter is indicated in the image. (f) Plot of the size of the PMR nanoparticles vs. dilution ratio.
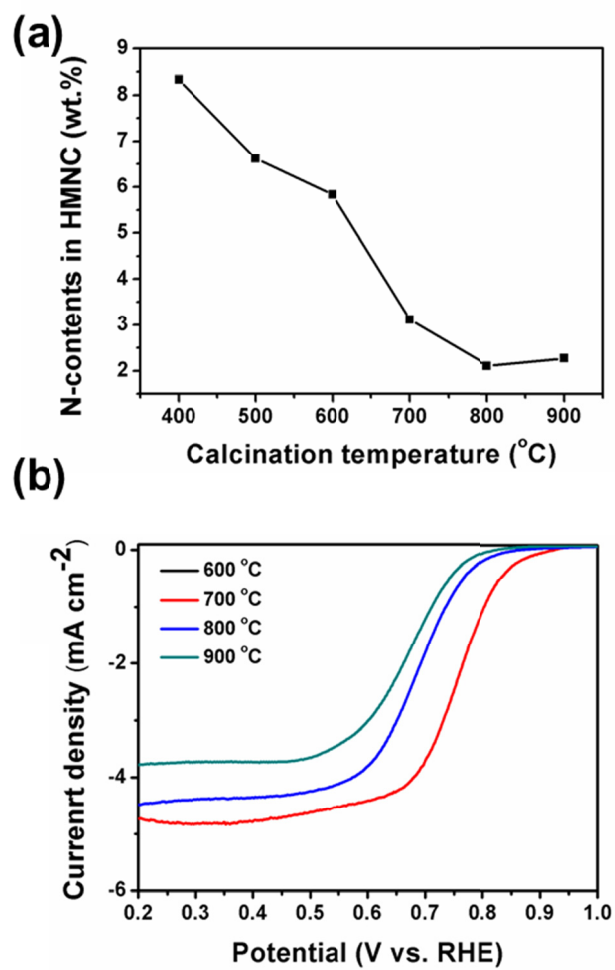
Figure 3.4. (a) Plot of calcination temperature vs. N-contents in HMNC nanoparticles. (b) Oxygen reduction reaction activity of HMNC depending on the carbonization temperature.

3.3.2. Characterizations of Hierarchical N-doped Mesoporous Carbon (HMNC)

To investigate the morphology and size of the particles, SEM and TEM observations of the HMNC particles were conducted (Figure 3.5.a,b). The representative HMNCs show uniform spherical morphology with a size of approximately 167 nm. In the high-resolution SEM images, an ordered hexagonal array of mesopores can be seen on their surfaces, demonstrating an open pore structure (inset of Figure 3.5.a). The highly ordered mesostructure of the HMNC samples was characterized by SAXS analysis. The SAXS pattern exhibited two well-resolved diffraction peaks (Figure 3.5.c), which can be indexed as the 110 and 211 reflections of a body-centered cubic *Im3m* space group. To evaluate the nitrogen doping and bond configurations after carbonization at 700 °C, the XPS spectrum in the N 1s region was obtained for the HMNC sample (Figure 3.5.d). The result shows main peaks at 398.3 and 400.7 eV, corresponding to pyridinic-N (N-6) and graphitic-N (N-Q) respectively. Furthermore, there are minor peaks ascribed to pyrrolic-N (N-5) at 399.7 eV and a pyridinic-N-oxide peak at 402.3 eV. The calculated percentages of each bond configurations are listed in Table 1. N_2 adsorption–

desorption isotherms of HMNC show pseudo-type-I curves with H1 hysteresis loops at high relative pressures (Figure 3.5.e).[20] The pore-size distribution, calculated by the BJH method from the desorption branch, is centered at 3.0 nm (Figure 3.5.f). Moreover, broad macropores derived from the interparticle gaps between the HMNCs were observed. This series of results implies that HMNCs have a highly ordered and hierarchical macro/mesoporous structure with N-6 and N-Q configurations. Meanwhile, the carbonization under vacuum conditions plays a critical role in maintaining the original mesoporous structure of the HMNCs. The carbonization of the PMR polymer in an Ar environment (denoted as HMNC_Ar) led to a collapse or blockage of the mesopores, confirmed by N_2 adsorption–desorption isotherms (Figure 3.5.e). In an inert environment, the volatile products from the melamine resin cannot be removed efficiently because the melamine resin is extensively degraded at temperatures greater than 375 °C.[21] The pore size distribution confirmed that the hierarchical macro/mesoporous structure was deteriorated in the HMNC_Ar sample (Figure 3.5.f). Therefore, the existence of hierarchical porous structure can be controlled by changing the carbonization conditions.
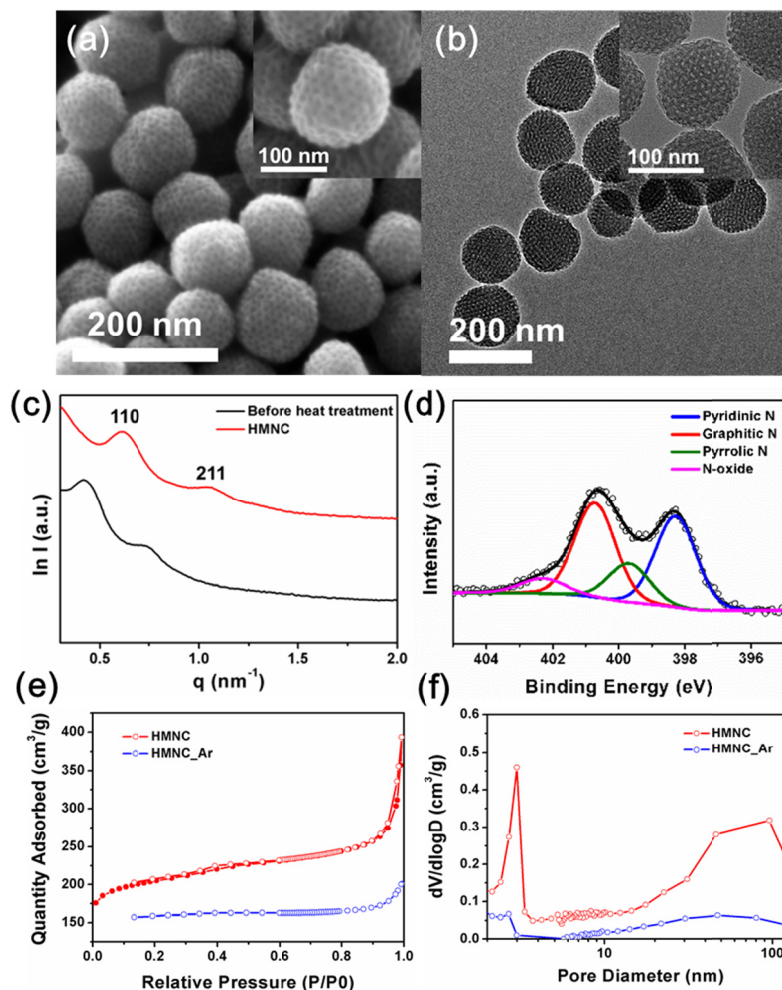
Figure 3.5. (a) SEM and (b) TEM images of HMNC nanoparticles with a diameter of 167 nm. (c) SAXS patterns of HMNC before and after carbonization. (d) N 1s branch of the HMNC XPS spectrum. (e) N_2 adsorption–desorption isotherms of HMNC and HMNC_Ar. (f) Pore size distribution curve from the desorption branch using the BJH model.

Table 1. Summary of XPS fitting results of the HMNC.

Carbonization	Pyridinic N (%)	Pyrrolic N (%)	Graphitic N (%)	N-O (%)
600 °C	45.119	17.545	34.467	2.869
700 °C	37.548	15.910	39.050	7.492
800 °C	29.772	11.476	46.730	12.023
900 °C	26.728	14.852	44.908	13.511

3.3.3 Optimization of the N-doped Carbon Support for the Oxygen Reduction Reaction

The optimization of the Fe-N-C catalyst was first conducted on the N-doped carbon support because the physicochemical properties of the support determine the active site utilization and mass transport properties. The HMNCs with a diameter of about 167 nm were selected to represent a nano-sized mesoporous carbon support. As a control group, the HMNC_Ar represents a nano-sized microporous carbon support, while micro-sized HMNCs (denoted Micro_HMNCs) represent a bulky mesoporous carbon support. The size and porosity of the Micro_HMNCs were characterized by TEM, SAXS, and N_2 adsorption–desorption measurements (Figure 3.6.b–e). After the carbonization process, a second heat treatment in NH_3 at 900 °C was applied to improve the ORR activity (NH_3 activation). Reactive NH_3 gas can lead to the facile gasification of the disordered carbon phase, yielding large numbers of micropores on the surfaces. After NH_3 activation, the morphology and mesoporous structure of all the samples (denoted as sample name(A)) were found to be preserved compared to the samples before NH_3 activation. Notably, the BET surface areas of all samples were similar, around 850 $m^2\,g^{-1}$, which is

extremely suitable for comparison to demonstrate the effects of other factors than the microporous area (Figure 3.6.f). The prepared carbon materials including HMNCs, Micro_HMNCs, and HMNCs_Ar after NH_3 activation were studied as electrocatalysts for the ORR in alkaline media (0.1 M KOH). ORR polarization curves (Figure 3.7.a) and electron transfer numbers (Figure 3.7.b) during ORR were recorded. Considering that nitrogen functional groups are considered as active sites for the ORR, nitrogen XPS analysis was conducted to discuss the activity trend.[21] After NH_3 treatment, HMNC(A) showed a remarkably high activity compared to Micro_HMNC(A) and HMNC_Ar(A), albeit all samples have similar BET surface areas (around 850 m^2g^{-1}) and similar nitrogen functional groups, indicating that not only nitrogen functional groups but other factors affect the ORR activity significantly. We conjecture that the activity difference could originate from the carbon structure because other factors were controlled to be similar. To reveal the structural effects on the ORR activity of the porous carbon, we conducted electric double layer capacitance (EDLC) analysis through CV and EIS measurements. The EDLC_CV of HMNC(A) shows higher values (96.7 F g^{-1}) compared to that of HMNC_Ar(A) (62.0 Fg^{-1}) and Micro_HMNC(A) (64.8 Fg^{-1}),

indicating that both HMNC_Ar(A) and Micro_HMNC(A) cannot effectively utilize their pore structure for electrochemical reaction (Figure 3.8.a,b). We also conducted static EDLC (EDLC_EIS) analysis to determine the utilization of the porous carbon structure through EIS measurements under non-faradaic conditions using the transmission line model, which is often used to understand the behavior of porous materials in EDLCs.[22,23] The EIS results were interpreted based on the complex capacitance analysis for extracting frequency-related information (Table 2).[24-26] The calculated C_0 values of HMNC(A) and Micro_HMNC(A) are similar (102.7 and 108.0 F g^{-1}, respectively). However, that of HMNC_Ar(A) is low (72.6 F g^{-1}), indicating that the microstructure alone cannot utilize the surface area because of the limited electrolyte wetting. By comparing η_{ideal} of each sample (Figure 3.8.c), we found that the mesopores are important for utilizing the micropore surface area effectively. The main origin of the low utilization of HMNC_Ar is the low electrolyte wetting. Because C_0 does not include kinetic factors, the low η_{ideal} value is attributed to the smaller interphase between the carbon and the electrolyte. The much lower η_{ideal} value of HMNC_Ar(A) compared to other NH$_3$ activated samples further corroborates our interpretation

1 5 1

that the micropore structure alone limits the formation of a solid/liquid interphase.

To understand the low utilization of the Micro_HMNC sample, we considered the real efficiency of the electrode (η_{real}) of each sample (Figure 3.8.d). In the case of HMNC, the η_{real} is almost unchanged after NH_3 activation, implying the full utilization of the active sites in the micropores. However, Micro_HMNC showed a significant decrease in activity after the NH_3 activation, which indicates limited utilization of the active sites. We also conducted kinetic analysis by calculating the relaxation time constant (Figure 3.9.a). From the peak frequency (f_0) of $C''(\omega)$, the relaxation time constant ($\tau_0 = (2\pi f_0)^{-1}$) can be calculated, which reflects the kinetic performance of the supercapacitor. When comparing HMNC and HMNCs_Ar, the time constant of HMNC_Ar is slightly faster than that of HMNC, which is related to the fact that only micropores close to particle surface can participate in the electrochemical reaction in the case of HMNC_Ar. The Micro_HMNC sample has a large time constant compared to those of the nano-sized samples, indicating that the long diffusion path inside the particles results in a high resistance to facile mass transport (Figure 3.9.b). After NH_3 treatment, the time constant of HMNC(A) is

faster than that of HMNC_Ar(A) (Figure 3.9.c). The reverse trend before and after NH$_3$ treatment originates from the large time constant increase of HMNC_Ar after NH$_3$ treatment, indicating that the mesopores not only increase the interphase formation between the electrode and electrolyte but also increase the mass transport issues. From the CV coupled with EIS analysis, we conclude that the hierarchical porous structure is ideal for maximizing the electrocatalytic surface with fast kinetics. Furthermore, the nano-sized structure can diminish the transport length, resulting in low mass transport resistance in electrochemical systems (Figure 3.9.d). To the best of our knowledge, this is the first demonstration of the utilization of a hierarchical porous structure and systematic investigation of the advantages of nano-sized carbon in terms of kinetics and electrolyte wetting using a well-defined model system.

The enhancement of the electron transfer number to 4e$^-$ in all samples after NH$_3$ treatment is also explained by the increase in the active surface area and the porous structure (Figure 3.7.b). When increasing the active surface area, the collision frequency of reactants, including oxygen and reaction intermediates, increases.[27] The enhancement in the collision frequency of the reaction intermediates

results in further reaction pathways to H_2O formation via the $4e^-$ pathway. The reaction selectivity increase associated with a high collision frequency on increasing the active surface area is further supported by the results of samples without NH_3 treatment. HMNC only shows a $4e^-$ dominant pathway ($n = 3.3$); however, HMNC_Ar and Micro_HMNC show a dominant two-electron pathway, indicating a high reaction probability because the high active surface area affects the reaction pathway. Furthermore, the ORR selectivity increases with increasing catalyst loading.[28,29] The ORR selectivity increases by simply increasing the catalyst loading excludes any catalytic active site effects and can only be explained by the increase of reactant collision probability by the increased catalyst layer thickness. We hypothesize that increasing the reactant collision probability by pore structure engineering is helpful not only increasing the activity but enhancing the reaction selectivity. Consequently, the utilization of the active sites in the micropores depends on the existence of ordered mesoporous channels in the catalysts, which allow facile access of the reactants and electrolytes to the active sites. The macropores derived from the interparticle gaps can act as electrolyte reservoirs, leading to an enhancement in mass transport.
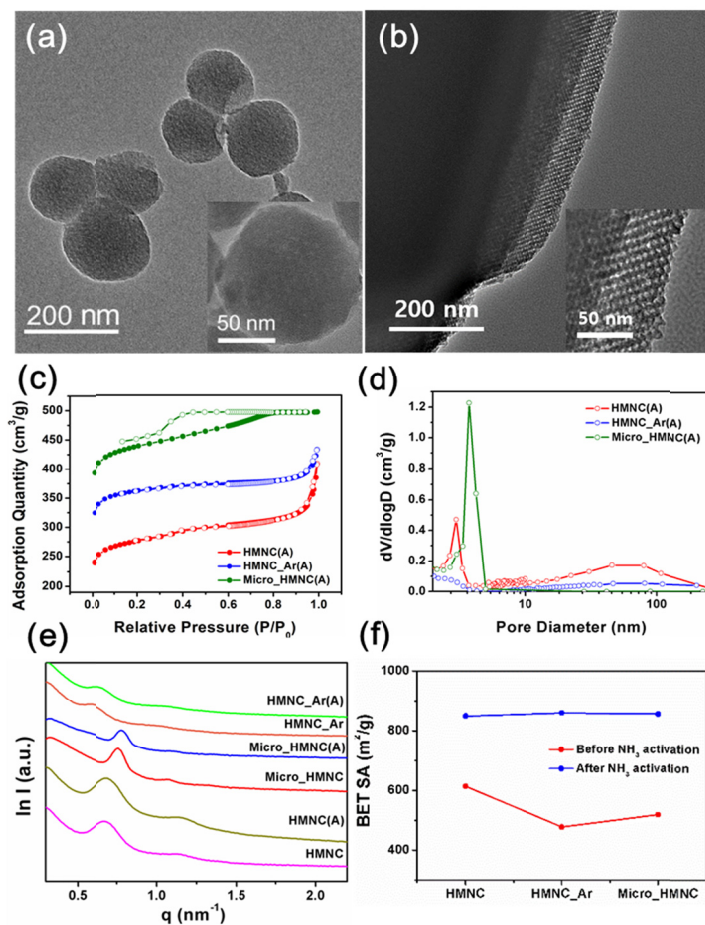
Figure 3.6. TEM images of (a) HMNC_Ar(A) and (b) Micro_HMNC(A). (c) N$_2$ adsorption–desorption isotherms of HMNC(A), HMNC_Ar(A), and Micro_HMNC. (f) Pore size distribution curve from the desorption branch of (c) using the BJH model. (e) SAXS patterns for HMNC(A) and control groups. (f) Surface area calculated by BET model before and after NH$_3$ activation..
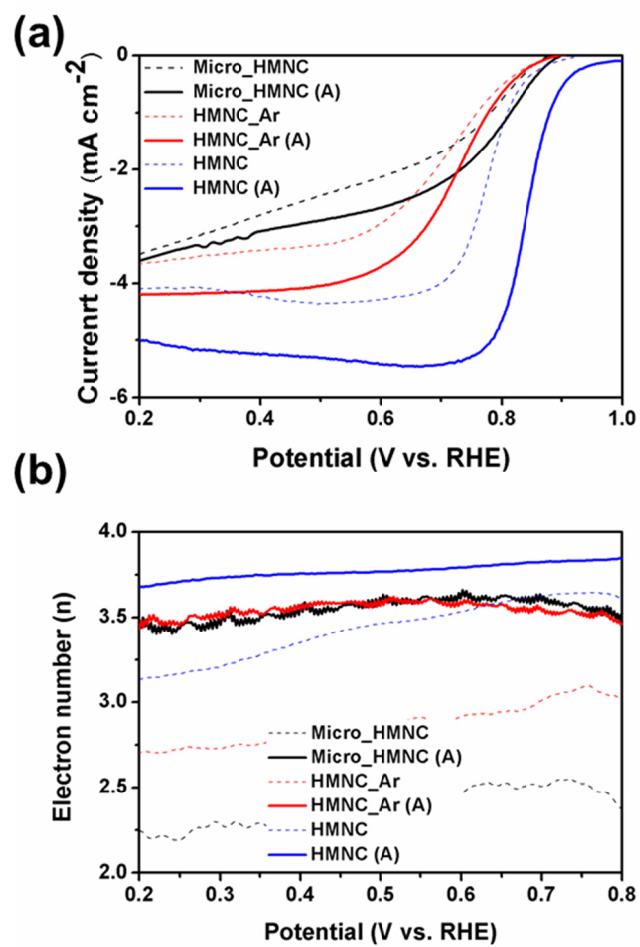
Figure 3.7. (a) ORR polarization curves and (b) number of electrons transferred of HMNC(A) and control groups measured in 0.1 M KOH.
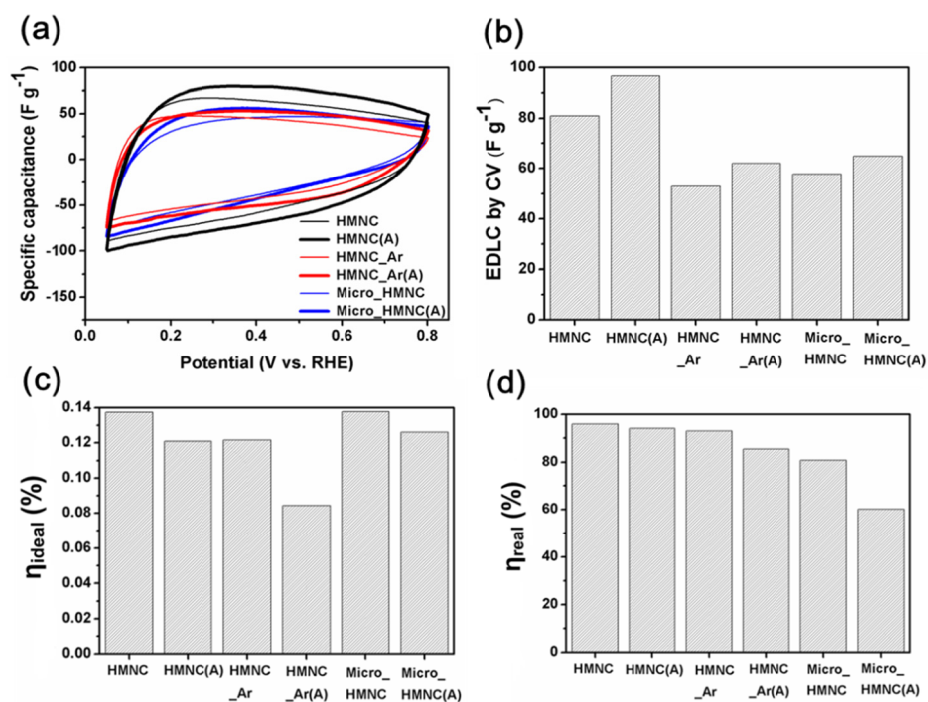
Figure 3.8. (a,b) EDLC analysis using CV measurements of the HMNC and control groups. Comparison of (a) η_{ideal} and (b) η_{real} of the HMNC and control groups, which are defined in the Section 3.2.6.

Table 2. Summary of complex capacitance analysis

	BET SA $[m^2 g^{-1}]$	EDLC by CV $[Fg^{-1}]$	Static EDLC by EIS $[Fg^{-1}]$	η_{ideal} [%]	η_{real} [%]
HMNC	613.8	80.9	84.4	0.138	95.9
HMNC(A)	849.7	96.7	102.7	0.121	94.2
HMNC_Ar	477.1	52.9	56.9	0.120	93.0
HMNC_Ar(A)	859.8	62.0	72.6	0.084	85.4
Micro_HMNC	518.7	57.7	71.4	0.138	80.8
Micro_HMNC(A)	856.4	64.8	108.0	0.126	60.0
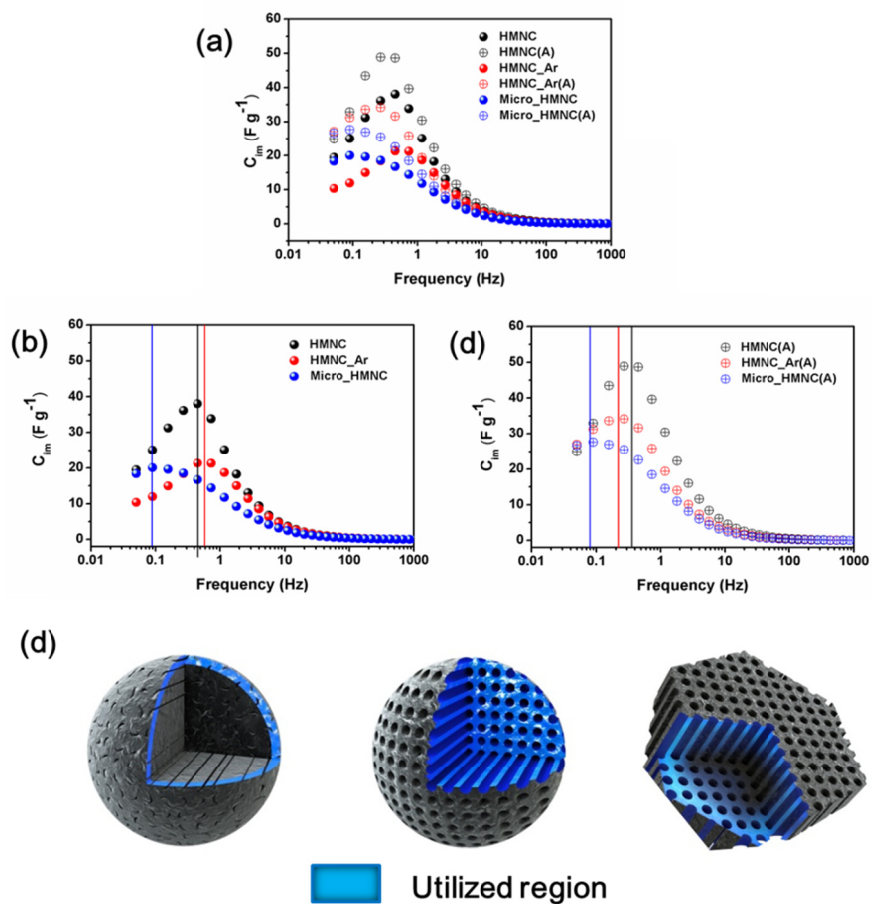
Figure 3.9. (a) Relaxation time constants calculated from EIS measurements of HMNC and the control group (b) before NH_3 activation and (c) after NH_3 activation. (d) Schematic illustration of regions used in HMNC and control groups during the ORR process.

3.3.3. Optimization of the Fe-N-C catalysts before NH$_3$ activation

Based on the results from the optimization of the carbon support, we extended the optimization process to the Fe-N-C catalysts by adding Fe^{3+} ions to the catalysts. To determine the effects of iron ions on the adjacent N-doped carbon support, different amounts of Fe^{3+} ions were adsorbed before carbonization. After heat treatment, morphological changes were observed depending on the amount of Fe^{3+} ions added (the samples are denoted Fe$_x$_HMNC, and the subscript corresponds to the weight of FeCl$_3$ added to the catalysts). In the case of Fe$_{1.9}$_HMNC, the morphology and mesoporous structure were the same as that of HMNC (Figure 3.10.a). On the other hand, in the case of Fe$_{10}$_ and Fe$_{100}$_HMNC, spherical nanoparticles were generated in the carbon structure (Figure 3.10.b,c). The deformation of the well-ordered mesoporous structure was also detected in the SAXS measurements (Figure 3.10.d). The peaks in the XRD patterns of Fe$_{1.9}$_HMNC are assigned to amorphous carbon alone, implying that the iron existed in a disordered state. However, intense peaks related to metallic Fe$_3$C or Fe were detected as the amount of added Fe^{3+} ions increased (Figure 3.10.e). EXAFS analysis was utilized to probe the local coordination of iron in the Fe$_x$_HMNC samples (Figure 3.11.a).

1 6 0

In the case of $Fe_{1.9}$_HMNC, the Fourier transform (FT) of the Fe K-edge of the EXAFS spectrum contains a characteristic Fe-N/O peak at 1.6 Å, which is indicative of a Fe-N interaction. In contrast, the spectra of the Fe_{10}_HMNC and Fe_{100}_HMNC samples show broad peaks corresponding to a Fe-N/O peak at 1.6 Å and a peak at 2.2 Å, which can be fitted to Fe-Fe scattering. This result suggests that the pyrolysis step created not only Fe-Nx configurations but also resulted in the formation of metallic iron with a carbide phase.[30]

Interestingly, the BET specific surface area, especially the microporous surface area, decreased depending on the amount of Fe^{3+} ions added to the samples (Figure 3.11.b). It can be considered that most of the Fe^{3+} ions are deposited in the micropores on the catalyst surfaces. In Raman spectroscopy, the D band (centered at 1350 cm^{-1}) is known to be characteristic of disordered graphite. In particular, the D band must be deconvoluted into D1, D3, and D4 peaks in highly disordered carbon samples (Figure 3.11.c).[31] For these peaks, the increased full width at half-maximum (FWHM) of the D1 peak is related to the increase in the disordered carbon phase.[32] In our results, a constant decrease in the FWHM of the D1 peak was observed with increasing Fe^{3+} ion addition (Figure 3.11.d). Considering these results,

1 6 1

we conclude that Fe/Fe_3C NPs acted as graphitization catalysts bringing about a decrease in surface area, mesoporosity, and the amount of disordered carbon phase.

To evaluate the catalytic activity for ORR, the prepared catalysts were tested using an RRDE in 0.1 M KOH solution saturated with O_2. Compared to catalysts prepared with little additional Fe^{3+}, Fe_{100}_HMNC exhibit a much more positive half-wave potential (Figure 3.12). Moreover, the catalyst performance improved with increasing added Fe^{3+}, and this trend is inversely proportional to the structural factors, such as surface area and mesoporosity. Combining the physicochemical and electrochemical analyses of Fe_x_HMNC, we can conclude that the ORR activity is predominantly located on the N-doped carbon with subsurface Fe/Fe_3C.[9] A more facile ORR process was possible because the reactants can reach the active sites readily as a result of most of the N-doped carbon with Fe_3C/Fe NPs being located on the NP surfaces. Therefore, before the NH_3 activation process, the large amounts of Fe ions and resulting Fe_3C/Fe NPs facilitate active site formation and enhance the ORR performance, regardless of the disadvantages with respect to macroscopic factors.
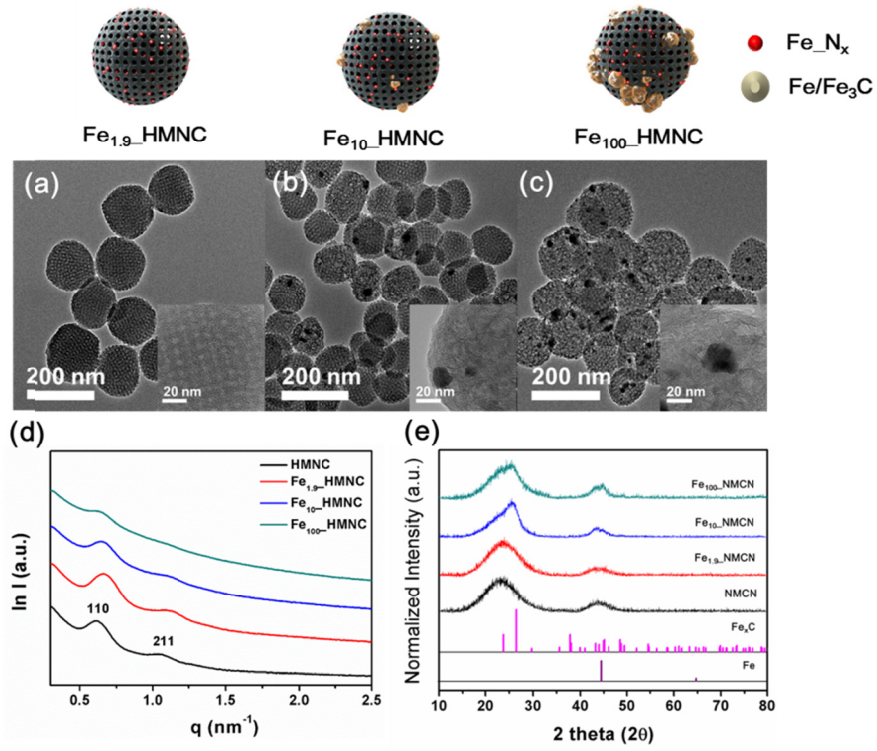
Figure 3.10. TEM images of the Fe$_x$_HMNC samples (a) x = 1.9, (b) x = 10, and (c) x = 100. (d) SAXS and (e) XRD patterns and of the Fe$_x$_HMNC samples (x = 1.9, 10, and 100).
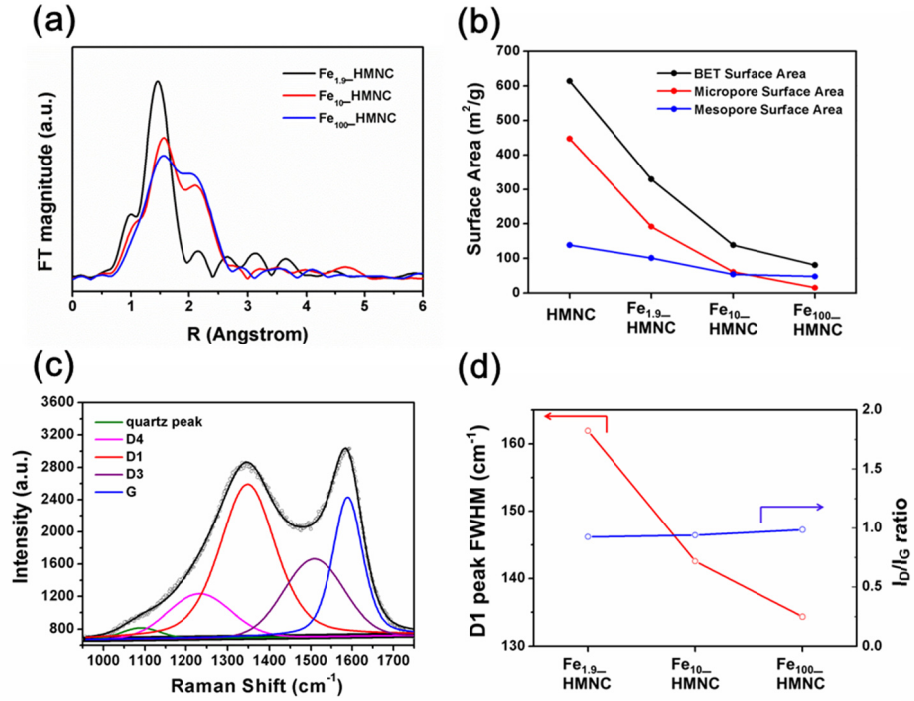
Figure 3.11. (a) Fourier transform EXAFS of the Fe_x_HMNC samples (x = 1.9, 10, and 100). (b) Comparison of the BET surface area, microporous surface area, and mesoporous surface area of HMNC and Fe_x_HMNCs (x = 1.9, 10, and 100). (c) The representative Raman spectra of $Fe_{1.9}\_HMNC$. (d) Plots of the D1 peak FWHM (I_D/I_G ratio) vs. Fe_x_HMNCs (x = 1.9, 10, and 100).
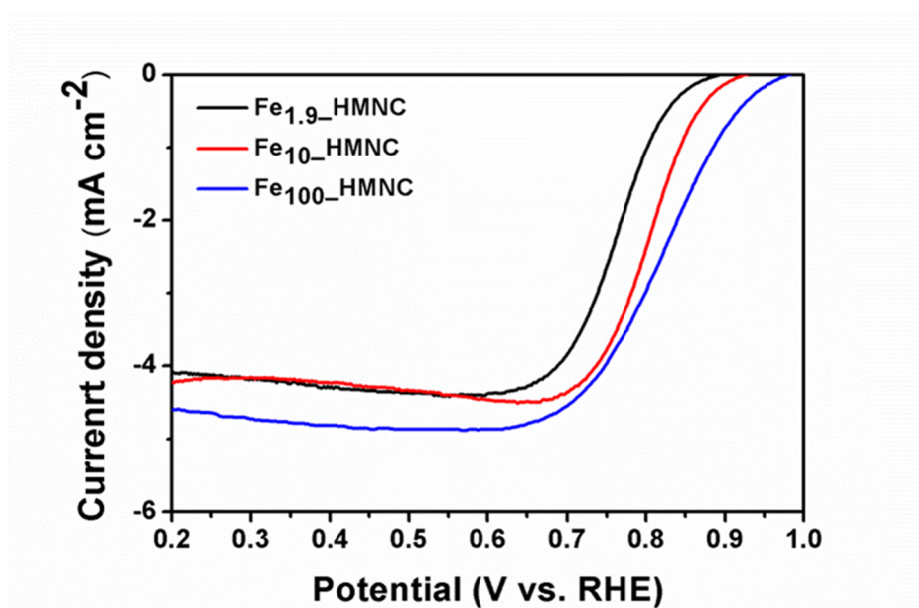
Figure 3.12. ORR polarization plots of the Fe$_x$_HMNC samples (x = 1.9, 10, and 100).

3.3.4. Optimization of Fe-N-C catalysts after NH$_3$ activation

After NH$_3$ activation, the catalysts did not show morphological changes compared to that of Fe$_x$_HMNC, which was confirmed by the TEM and SAXS analysis (Figure 3.13.a–d). Moreover, the XRD patterns after NH$_3$ activation are similar to that of Fe$_x$_HMNC, except the formation of new diffraction lines in the case of Fe$_{100}$_HMNC(A) (Figure 3.13.e). These new lines are characterized as an iron-rich iron nitride phase (FeN$_{0.03}$), indicating the incorporation of nitrogen into the vicinity of the Fe$_3$C/Fe NPs. The local coordination of the iron confirmed by EXAFS also shows no significant changes, except a reduction in the signal intensity of the characteristic Fe-N/O peak at 1.6 Å (Figure 3.13.f). Comparing these results with those obtained from the catalysts before NH$_3$ activation, we can conclude that NH$_3$ gas treatment affects the Fe local structure and electronic states little, which is in line with previous reports.[8,33] On the other hand, based on the BET measurements, the NH$_3$ activation caused considerable changes in the surface area and porous structure. The N$_2$ adsorption–desorption isotherms of the samples exhibited pseudo-type-I curves with H1 hysteresis loops at high relative pressures, which is similar to the case of HMNC(A) (Figure 3.14.a). These changes in the surface

1 6 6

area can be related to the FWHM of the D1 peaks of these catalysts before NH_3 activation. For the catalysts containing large amounts of iron, the amount of the disordered carbon phase was reduced by the effect of graphitization (Fe/Fe_3C NPs), which resulted in insufficient micropore formation (Figure 3.14.b). This change in the microporous surface area can be directly correlated to the ORR activity. We conducted ORR performance measurements of the Fe_x_HMNC(A) catalyst. The activities of Fe_{10}_HMNC(A) and $Fe_{1.9}$_HMNC(A) samples surpass that of the standard Pt/C catalyst, indicating superior ORR activity (Figure 3.15.a). All samples show nearly $4e^-$ pathways in all potential regions, which is close to the theoretical value of Pt/C (Figure 3.15.b). The high ORR activity of $Fe_{1.9}$_HMNC(A) is attributed to the lower degree of graphitization, the formation of an efficient Fe-N-C structure as revealed by EXAFS, and the ideal pore structure for facile mass transport supported by the model system. We also verified the feasibility of this system for real applications in fuel cells by testing the chemical selectivity and long-term durability. The long-term durability tests were conducted using 10,000 potential cycles in an accelerated durability test (ADT). After 10,000 potential cycles, there was no apparent activity loss, verifying the superior long-

term durability (Figure 3.15.c). Furthermore, no obvious morphological changes were observed by TEM or CV (Figure 3.15.d), indicating that the ordered porous structure is retained after the ADT potential cycles. Based on the above experimental results, we can determine the factors for the optimization of the Fe-N-C catalysts. First, the excess graphitization around Fe/Fe$_3$C NPs can reduce the disordered carbon phase in the catalysts, preventing micropore formation during NH$_3$ activation. Considering the correlation between micropores and Fe-N$_x$ active sites, excess graphitization must be avoided to maximize the active site density, as in the case of Fe$_{1.9}$_HMNC(A). Secondly, a well-ordered mesoporous structure is beneficial to the mass transfer properties compared to a randomly assembled porous structure. After NH$_3$ activation, all the catalysts recovered their hierarchical macro/mesoporous structure and this is a plausible reason for the increased ORR activities. However, the largest increase in ORR activity was observed in the case of Fe$_{1.9}$_HMNC(A), which maintained a well-ordered mesoporous structure even after two successive heat treatments. The deformation of the pore channels by excessive graphitization can disturb the diffusion pathways of the electrolytes and reactants, leading to inferior mass transport properties

and active site utilization.
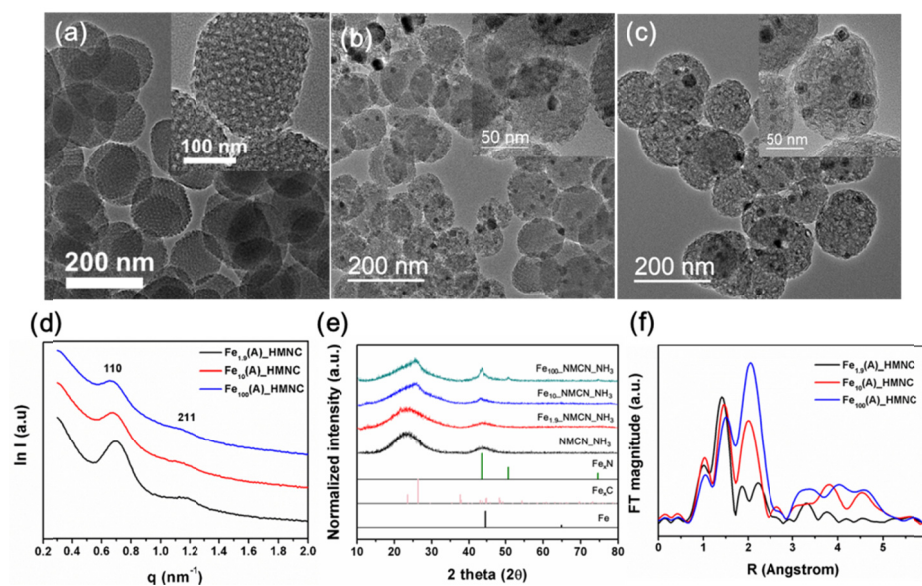
Figure 3.13. . TEM images of Fe$_x$_HMNC(A) (a) x = 1.9, (b) x = 10, and (c) x = 100. (d) SAXS, (e) XRD patterns and of the Fe$_x$_HMNC(A) samples (x = 1.9, 10, and 100). (f) Fourier transform EXAFS of the Fe$_x$_HMNC(A) samples (x = 1.9, 10, and 100).
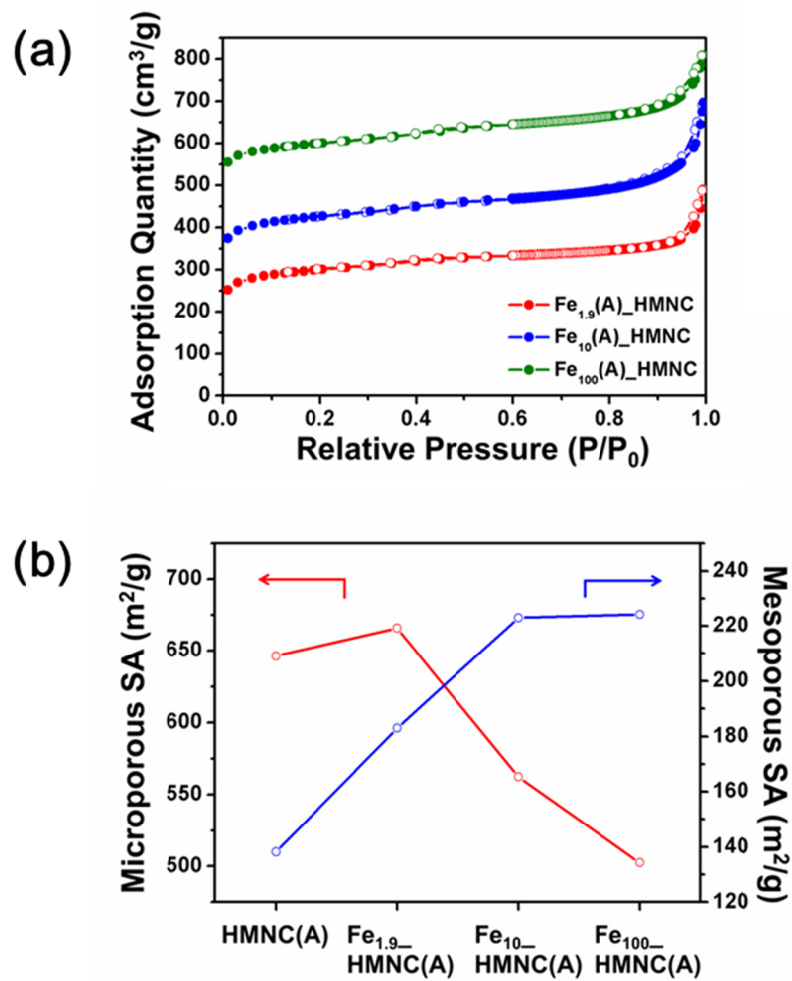
Figure 3.14. (a) N_2 adsorption–desorption isotherms of the Fe$_x$_HMNC(A) samples (x = 1.9, 10, and 100). (b) Comparison of the microporous and mesoporous surface area calculated by the BET method for HMNC(A) and Fe$_x$_HMNC(A)s (x = 1.9, 10, and 100).
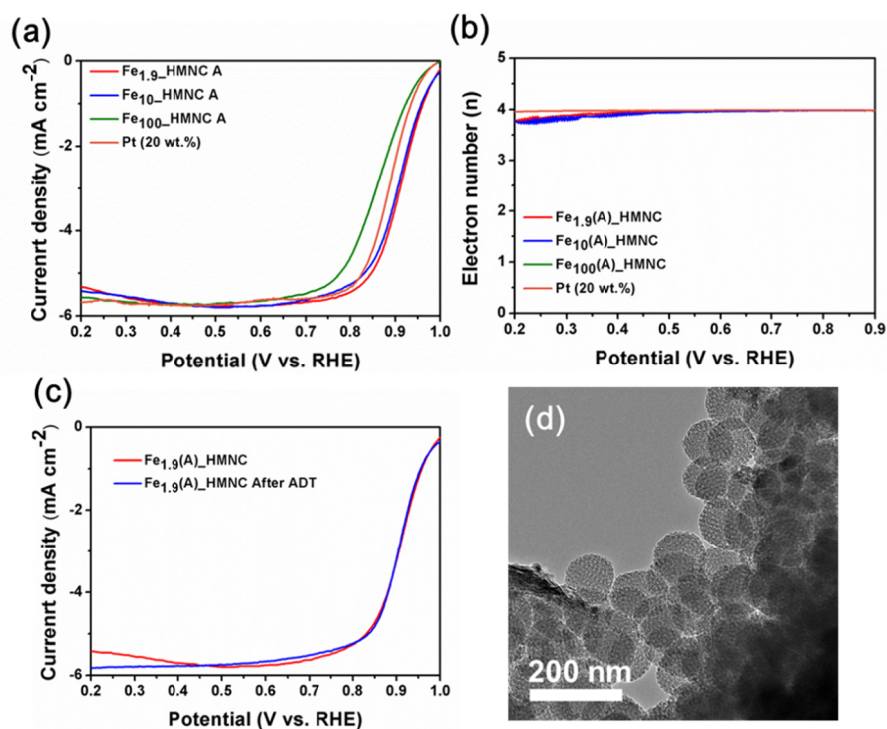
Figure 3.15. (a) ORR polarization curves and (b) number of electrons transferred from the $Fe_x\_HMNC(A)$ samples (x = 1.9, 10, and 100) and Pt/C (20 wt%). RDE and RRDE voltammetry data were recorded in 0.1 M KOH. (c) Changes in half-wave potentials of $Fe_{1.9}\_HMNC(A)$ before and after ADT of 10,000 cycles. (d) TEM image of the $Fe_{1.9}\_HMNC(A)$ sample after ADT of 10,000 cycles.

3.4 Conclusions

In conclusion, we have demonstrated a novel copolymer approach to obtain hierarchical porous N-doped carbon nanoparticles with facile control over the particle size and porous structure. The quantitative analysis of the complex capacitance conducted on various kinds of the N-doped carbon supports with different sizes and porous structures reveals that the ordered mesoporous structure and nano-sized particulate are critical for the excellent ORR performance. We found that, when the Fe^{3+} ions were incorporated in the catalysts, the graphitization of the carbon support affects the microscopic structure and mesoscopic structure simultaneously. After heat treatment in an inert environment, the formation of Fe/Fe_3C NPs derived from the excess Fe^{3+} ions enhanced the ORR performance irrespective of the mesoscopic structure. In contrast, the microporous surface area and well-ordered mesoporous structure in the catalysts determined the ORR activity after the second heat treatment in NH_3 gas. Through this systemic optimization process, our optimized Fe-N-C catalysts outperformed the state-of-the-art Pt/C catalysts with respect to the onset potential, specific activity, and durability. The exceptional ORR activity and durability of our electrocatalyst make it a promising

candidate for high-performance and cost-effective fuel cell catalysts. We believe that this approach for optimizing Fe-N-C catalysts can be further extended to fabricate other related electrocatalysts with enhanced performance and stability.

3.5 References

[1]   Jasinski, R. *Nature* **1964**, *201*, 1212-1213.

[2]   Jahnke, H.; Schönborn, M.; Zimmermann, G. Organic dyestuffs as catalysts for fuel cells. In *Physical and Chemical Applications of Dyestuffs*; Topics in Current Chemistry, Vol. 61; Springer: Berlin, Heidelberg, 1976; pp 133-181.

[3]   Gupta, S.; Tyrk, D.; Bae, I.; Aldred, W.; Yeager, E. *J. Appl. Electrochem*. **1989**, *19*, 19-27.

[4]   Lefèvre, M.; Proietti, E.; Jaouen, F.; Dodelet, J.-P. *Science* **2009**, *324*, 71-74.

[5]   Wu, G.; More, K. L.; Johnston, C. M.; Zelenay, P. *Science* **2011**, *332*, 443-447.

[6]   Jaouen, F.; Lefèvre, M.; Dodelet, J.-P.; Cai, M. *J. Phys. Chem. B* **2006**, *110*, 5553-5558.

[7]   Koslowski, U. I.; Abs-Wurmbach, I.; Fiechter, S.; Bogdanoff, P. *J. Phys. Chem. C* **2008**, *112*, 15356-15366.

[8]   Zitolo, A.; Goellner, V.; Armel, V.; Sougrati, M.-T.; Mineva, T.; Stievano, L.; Fonda, E.; Jaouen, F. *Nat. Mater*. **2015**, *14*, 937-942.

[9]   Strickland, K.; Miner, E.; Jia, Q.; Tylus, U.; Ramaswamy, N.;

Liang, W.; Sougrati, M.-T.; Jaouen, F.; Mukerjee, S. *Nat. Commun.* **2015**, *6*, 7343.

[10] Varnell, J. A.; Tse, E. C. M.; Schulz, C. E.; Fister, T. T.; Haasch, R. T.; Timoshenko, J.; Frenkel, A. I.; Gewirth, A. A. *Nat. Commun.* **2016**, *7*, 12582.

[11] Jaouen, F.; Proietti, E.; Lefèvre, M.; Chenitz, R.; Dodelet, J.-P.; Wu, G.; Chung, H. T.; Johnston, C. M.; Zelenay, P. *Energy Environ. Sci.* **2011**, *4*, 114-130.

[12] Jaouen, F.; Herranz, J.; Lefèvre, M.; Dodelet, J.-P.; Kramm, U. I.; Herrmann, I.; Bogdanoff, P.; Maruyama, J.; Nagoka, T.; Garsuch, A.; Dahn, J. R.; Olson, T.; Pylypenko, S.; Atanassov, P.; Ustinov, E. *ACS Appl. Mater. Interfaces* **2009**, *1*, 1623-1639.

[13] Liang, H.-W.; Zhuang, X.; Brüller, S.; Feng, X.; Müllen, K. *Nat. Commun.* **2014**, *5*, 4973.

[14] Gong, K.; Du, F.; Xia, Z.; Durstock, M.; Dai, L. *Science* **2009**, *323*, 760-764.

[15] Wei, W.; Liang, H.; Parvez, K.; Zhuang, X.; Feng, X.; Müllen, K. *Angew. Chem., Int. Ed.* **2014**, *53*, 1570-1574.

[16] Wang, G.; Sun, Y.; Li, D.; Liang, H.-W.; Dong, R.; Feng, X.; Müllen, K. *Angew. Chem., Int. Ed.* **2015**, *54*, 15191-15196.

[17] Tang, J.; Liu, J.; Li, C.; Li, Y.; Tode, M. O.; Dai, S.; Yamauchi, Y. *Angew. Chem., Int. Ed.* **2015**, *54*, 588-593.

[18] Lin, Y.-S.; Haynes, C. L. *J. Am. Chem. Soc.* **2010**, *132*, 4834-4842.

[19] Lee, J. H.; Lee, H. J.; Lim, S. Y.; Kim, B. G.; Choi, J. W. *J. Am. Chem. Soc.* **2015**, *137*, 7210-7216.

[20] Fang, Y.; Gu, D.; Zou, Y.; Wu, Z.; Li, F.; Che, R.; Deng, Y.; Tu, B.; Zhao, D. *Angew. Chem., Int. Ed.* **2010**, *49*, 7987-7991.

[21] Lv, C.; Su, Y.; Wang, Y.; Ma, X.; Sun, Q.; Jiang, Z. *J. Membr. Sci.* **2007**, *294*, 68-74.

[22] Guo, D.; Shibuya, R.; Akiba, C.; Saji, S.; Kondo, T.; Nakamura, J. *Science* **2016**, *351*, 361-365.

[23] Itagaki, M.; Suzuki, S.; Shitanda, I.; Watanabe, K.; Nakazawa, H. *J. Power Sources* **2007,** *164*, 415-424.

[24] Song, H.-K.; Jung, Y.-H.; Lee, K.-H.; Dao, L. H. *Electrochim. Acta* **1999,** *44*, 3513-3519.

[25] Jang, J. H.; Oh, S. M. *J. Electrochem. Soc.* **2004,** *151*, A571-A577.

[26] Chung, D. Y.; Lee, K. J.; Yu, S.-H.; Kim, M.; Lee, S. Y.; Kim, O.-H.; Park, H.-J.; Sung, Y.-E. *Adv. Energy Mater.* **2015,** *5*, 1401309.

[27] Bae, J. H.; Han, J.-H.; Han, D.; Chung, T. D. *Farad. Discuss.* **2013,** *164*, 361-376.

[28] Bonakdarpour, A.; Lefevre, M.; Yang, R.; Jaouen, F.; Dahn, T.; Dodelet, J.-P.; Dahn, J. R. *Electrochem. Solid State Lett.* **2008,** *11*, B105-B108.

[29] Biddinger, E. J.; Deak, D. v.; Singh, D.; Marsh, H.; Tan, B.; Knapke, D. S.; Ozkan, U. S. *J. Electrochem. Soc.* **2011,** *158*, B402-B409.

[30] Jiang, W.-J.; Gu, L.; Li, L.; Zhang, Y.; Zhang, X.; Zhang, L.-J.; Wang, J.-Q.; Hu, J.-S.; Wei, Z.; Wan, L.-J. *J. Am. Chem. Soc.* **2016**, *138*, 3570-3578.

[31] Ferrari, A. C.; Basko, D. M. *Nat. Nanotechnol.* **2013**, *8*, 235-246.

[32] Sadezky, A.; Muckenhuber, H.; Grothe, H.; Niessner, R.; Pöschl, U. *Carbon* **2005**, *43*, 1731-1742.

[33] Kramm, U. I.; Lefèvre, M.; Larouche, N.; Schmeisser, D.; Dodelet, J.-P. *J. Am. Chem. Soc.* **2014**, *136*, 978-985.

Bibliography

1. Journal Publications

1) **<u>Soo Hong Lee</u>** (*co-first author*), Seung-Ho Yu, Ji Eun Lee, Aihua Jin, Dong Jun Lee, Nohyun Lee, Hyungyung Jo, Kwangsoo Shin, Tae-Young Ahn, Young-Woon Kim, Heeman Choe, Yung-Eun Sung, and Taeghwan Hyeon

"Self-Assembled Fe_3O_4 Nanoparticle Clusters as High Performance Anodes for Lithium-Ion Batteries via Geometric Confinement"

Nano Letters, **2013**, *13*, 4249-4256

2) **<u>Soo Hong Lee</u>**, Byung Hyo Kim, Hyon Bin Na, and Taeghwan Hyeon

"Paramagnetic inorganic nanoparticles as T1 MRI contrast agents"

Wiley Interdisciplinary Reviews: Nanomedicine and Nanobiotechnology, **2013**, *6*, 196-209

3) Seung-Ho Yu, **<u>Soo Hong Lee</u>** (*co-first author*), Dong Jun Lee, Yung-Eun Sung, and Taeghwan Hyeon

"Conversion Reaction-Based Oxide Nanomaterials for Lithium

Ion Battery Anodes"

Small, **2016**, *12*, 2146-2172

4) **Soo Hong Lee** (*co-first author*), Jiheon Kim, Dong Young Chung, Ji Mun Yoo, Hyeon Seok Lee, Soon Gu Kwon, Yung-Eun Sung and Taeghwan Hyeon
"Optimization of Activity and Mass Transfer Properties of Fe-N-C catalysts"
In preparation

5) **Soo Hong Lee** (*co-first author*), Ok Kyu Park, Jonghoon Kim, Kwangsoo Shin, Nohyun Lee, Seung-Hae Kwon, and Taeghwan Hyeon
"Immune cell-mediated anticancer drug delivery using click chemistry for breast cancer treatement"
In preparation

6) Nohyun Lee, Hye Rim Cho, Myoung Hwan Oh, **Soo Hong Lee**, Kangmin Kim, Byung Hyo Kim, Kwangsoo Shin, Tae-Young Ahn, Jin Woo Choi, Young-Woon Kim, Seung Hong Choi, and

Taeghwan Hyeon

"Multifunctional Fe3O4/TaOx Core/Shell Nanoparticles for Simultaneous Magnetic Resonance Imaging and X-ray Computed Tomography"

Journal of the American Chemical Society, **2012**, *134*, 10309-10312

7) Kwangsoo Shin, Jin Woo Choi, Giho Ko, Seungmin Baik, Dokyoon Kim, Ok Kyu Park, Kyoungbun Lee, Hye Rim Cho, Sang Ihn Han, **Soo Hong Lee**, Dong Jun Lee, Nohyun Lee, Hyo-Cheol Kim & Taeghwan Hyeon

"Multifunctional nanoparticles as a tissue adhesive and an injectable marker for image-guided procedures"

Nature Communications, 2017, 8, 15807

8) Hyunbum Kim, Kwangsoo Shin, Ok Kyu Park, Daheui Choi, Hwan D. Kim, Seungmin Baik, Soo Hong Lee, Seung-Hae Kwon, Kevin J. Yarema, Jinkee Hong, Taeghwan Hyeon, and Nathaniel S. Hwang

"General and Facile Coating of Single Cells via Mild Reduction"

Journal of the American Chemical Society, **2017,** *in revision*

2. International Conference Presentations

1) <u>**Soo Hong Lee**</u>, Seung-Ho Yu, Yung-Eun Sung and Taeghwan Hyeon

"Self-Assembled Fe_3O_4 Nanoparticle Clusters as High-Performance Anodes for Lithium Ion Batteries via Geometric Confinement"

Research Society 2014 Spring Meeting, MRS, San Francisco, San Francisco, CA, USA, Apr. 21-24, 2014.

2) <u>**Soo Hong Lee**</u>, Seung-Ho Yu, Yung-Eun Sung and Taeghwan Hyeon

"Self-Assembled Fe_3O_4 Nanoparticle Clusters as Highly Stable Anodes for Lithium Ion Batteries via Geometric Confinement Effects"

The World Conference on Carbon (Carbon 2014), ICC Jeju, Jeju, Koera, June 29- July 4, 2014.

3) **Soo Hong Lee**, Seung-Ho Yu, Yung-Eun Sung and Taeghwan Hyeon

"Self-Assembled Fe_3O_4 Nanoparticle Clusters as Stable SEI Formation via Geometric Confinement for Li-ion Battery Anodes"

45th IUPAC World Chemistry Congress (IUPAC-2015), BEXCO, Busan, Korea, August 9-14, 2015

3. Domestic Conference Presentations

4. Award

초 록

   최근 다양한 메조기공을 가진 나노물질들을 전기화학적 에너지 장비에 응용하는 연구가 많이 진행되고 있다. 메조기공 나노물질들은 활성점이 존재할 수 있는 넓은 표면적뿐만 반응물과 생성물의 물질이동 경로를 짧게 하여 윤활하게 만들어 주는 역할을 할 수 있다. 그러나, 메조 기공 나노 물질 또한 한계점이 존재한다. 보통 넓은 표면적에서 기인하는 부반응이 매우 활발하고, 촉매내 물질이동에 대한 수적 데이터가 부족한 상황이다. 이 학위 논문에서는 정렬된 메조기공을 가진 나노물질을 합성하고 이를 통해 메조기공 나노물질이 갖는 전기화학적 한계를 극복하는 점에 대하여 기술한다.

  먼저, 메조 기공을 가진 마그네타이트 산화철 나노입자 집합체를 자가 배열 합성법을 이용하여 개발하였다. 산화철 나노입자 사이에 존재하는 메조기공으로 인하여 베터리 구동중에 부피팽창을 완화시킬 수 있었고, 메조 기공의 짧은 확산 거리로 인해 높은 방전용량비를 기록하였다. 집합된 구조를 통해 표면적을 감소시켜 안정된 고체 전해질 상호상을

형성하여 높은 안정성을 가진 베터리 음극재료로 활용할 수 있음을 보여주었다.

다음으로, 연료전지의 양극재로써 사용되는 값비싼 백금 촉매을 대체하기 위해 메조 기공을 가진 철-질소-탄소 촉매를 개발하였다. 양극재에서 일어나는 산소 환원 반응은 촉매점의 원자 배열 상태뿐만 아니라, 물질 전달 성질과 촉매점 활용도에 따라 결정된다. 복소수 정전용량 분석 방법을 이용한 대조군과의 비교를 통해, 정렬된 메조 기공은 촉매점의 활성도를 높게하기 위해 필요하다는 것을 증명하였다. 또한 촉매의 크기는 나노 미터 수준에서 가장 높은 물질 전달 성질을 보여주었다. 가속 안정성 실험에서 최적화된 철-질소-탄소 촉매는 10,000번의 촉매 반응 후에도 활성도를 거의 잃지 않았다. 나노 물질의 형태학적 변화를 통해 우리는 최적화된 철-질소-탄소 촉매 구조를 증명할 수 있었고, 알칼리 전해질 연료전지에서 백금촉매보다 높은 활성도를 보였다.

주요어: 메조기공 물질, 리튬-이온 전지, 고체 전해질 상호상, 산소 환원 반응, 복소수 정전용량 분석

학번: 2011-21061